August 2015

Mechanical and Electro-Mechanical Properties of Crystalline Organic Semiconductors

Marcos A. Reyes-Martinez
University of Massachusetts Amherst

MECHANICAL AND ELECTRO-MECHANICAL PROPERTIES OF CRYSTALLINE ORGANIC SEMICONDUCTORS

A Dissertation Presented

by

MARCOS AURELIO REYES-MARTINEZ

Submitted to the Graduate School of the
University of Massachusetts Amherst in partial fulfillment
of the requirements for the degree of

DOCTOR OF PHILOSOPHY

May 2015

Polymer Science and Engineering

MECHANICAL AND ELECTRO-MECHANICAL PROPERTIES OF CRYSTALLINE ORGANIC SEMICONDUCTORS

A Dissertation Presented

by

MARCOS AURELIO REYES-MARTINEZ

Approved as to style and content by:

Alfred J. Crosby, Co-chair

Alejandro L. Briseno, Co-chair

Ashwin Ramasubramaniam, Member

David A. Hoagland, Department Chair
Polymer Science and Engineering

DEDICATION

This work is dedicated to my mother Antonia Martinez. Her love, support, and encouragement are inexhaustible.

ACKNOWLEDGMENTS

Before anything, I would like to thank my thesis advisors Prof. Alfred Crosby and Prof. Alejandro Briseno. I have learned an innumerable amount of valuable lessons from both of them that will always permeate though my personal and scientific life. Together they made a one-of-a-kind team and I feel truly blessed for having them as my advisors and mentors. In my first days as a graduate student I was set on working with electronic devices and joining the Crosby group was not part of my plan. Everything changed when I met with Al for the first time; I immediately understood the importance of having a caring and dedicated advisor. His scientific creativity, patience and work-life balance will always be sources of inspiration and standards to emulate. Working with Alex has been a life-changing experience. When I first met him, his passion for science infected me. I immediately knew I wanted to join his group not only because the work was related to electronics but also because he spoke to me in Spanish, which made me feel closer to home. From him I learned perseverance and the importance of collaboration. I will never forget his visits to the lab, his displays of creativity and our countless conversations regarding what it takes to achieve success in the sciences. I am also deeply grateful to have Prof. Ashwin Ramasubramaniam. Beyond performing all the theoretical calculations shown in this dissertation, he was always willing to talk and to help me think through whatever scientific problem I was having. His questions were insightful and made me dig deeper in my research. I hope that after completing my Ph.D., our relationship continues beyond thesis committee-student and expands to a lifetime of personal and scientific friendship.

I want to thank all the Crosby group members I have coincided with. Especially, the wrinkling subgroup members: Chelsea, Derek, Dinesh, Yuri, Yu-Cheng, Mikey, Han-Yu. Thanks for all the great wrinkling discussions we had and for all the help in the lab. Also, I want to thank Briseno group members I have worked with, in particular, Jung-Ah Lim for teaching me how to grow crystals and how to measure transistors in my first days as a group member. I would also like to acknowledge the very talented undergraduate students I have been fortunate to work with: Niva Ran, for assisting me with initial rubrene wrinkling experiments, Gabriela Rodriguez for her efforts wrinkling single crystals of several materials and Shehzeen Hussain, for her work in the optimization of biaxial wrinkling of rubrene crystals. I will always be grateful for you hard work.

Every journey has a starting point, and I believe my journey towards a scientific career started in high school. I want to acknowledge Rev. Pedro Cartaya, S.J., who was my meteorology, astronomy, and philosophy teacher at Loyola, Santo Domingo. Our long conversations about science, technology, and religion inspired me to become a scientist and a good person. His curiosity and passion for knowledge still resonate inside me. I also want to thank my teacher Ramon Caraballo, who implanted in me the love for astronomy and astrophotography that ultimately got me interested in pursuing physics as a major. I thank my college advisor, Prof. Rodney Yoder, who took the time to teach me fundamental physics and who guided me in the direction of graduate school. I am infinitely grateful to my benefactors Mrs. Nidia Rodriguez, Mrs. Maria Rodriguez and Mr. Gaston Cantens whose financial support allowed to pursue my studies in United States.

I made a lot of great friends during my time at PSE. I especially want to thank Sami Fakhouri who became more than a friend, a brother. Ian Henderson for showing me the best places to eat, drink and hike and Western Massachusetts. Daniel Acevedo

and Luis Cajamarca for always having the time to talk and decompress with me. I know I will always be able to count on all of them.

My parents, Antonia and Aureliano, for believing in me and for supporting me in all my crazy decisions at all times, including my decisions of becoming a scientist and leaving them and my country behind to pursue my studies. I thank my dad for showing me the importance of hard work and also instilling in me the love for books. I thank my sister, Magdeline, for always being there for me and for making sure I never gave up. There are no words to describe how grateful I am to my mother, who still sacrifices so much to see me happy and successful. She reminded me every step of the way that if I did everything with love, everything was going to work out. For this, I have dedicated my Ph.D. work to her. Lastly, I want to acknowledge the Martinez family, my new parents and siblings, who have showed their support constantly through this process and who I know I can count on for whatever comes next.

Finally, I would like to thank my loving wife, Itza. She is my new family, my best friend and the most patient human being I have ever met. Without her infinite love and consideration I would have not been able to complete this dissertation. She has been my anchor from the beginning and I know she will always be.

> *"The worthwhile problems are the ones you can really solve or help solve, the ones you can really contribute something to. No problem is too small or too trivial if we can really do something about it."*
>
> *-Richard Feynman*

ABSTRACT

MECHANICAL AND ELECTRO-MECHANICAL PROPERTIES OF CRYSTALLINE ORGANIC SEMICONDUCTORS

MAY 2015

MARCOS AURELIO REYES-MARTINEZ

B.A., MANHATTANVILLE COLLEGE

M.Sc., UNIVERSITY OF MASSACHUSETTS AMHERST

Ph.D., UNIVERSITY OF MASSACHUSETTS AMHERST

Directed by: Professor Alfred J. Crosby and Professor Alejandro L. Briseno

The study of the physical properties of organic crystalline semiconductors has allowed the advent of a new generation of high-performance organic electronic devices. Exceptional charge-transport properties and recent developments in large-area patterning techniques make organic single crystals (OSCs) excellent candidates for their utilization in the next-generation of electronic technologies, including flexible and conformable organic thin-film devices. In spite of the profound knowledge of the structural and electrical properties of OSCs, knowledge of the mechanical properties and the effects of mechanical strain is almost non-existent. This dissertation aims to bring new understanding of the intrinsic mechanical properties and the effect of mechanical strains in charge transport phenomena in organic semiconductors.

In our studies, the wrinkling instability is chosen as the metrology tool for the effective in-plane elastic constants of OSCs. We demonstrate that the wrinkling instability

can be used to obtain the elastic constants of single crystals of rubrene, tetracene, PDIF-CN_2 (N,N'-1H,1H-perfluorobutyldicyanoperylene-carboxydi-imide) and perylene. We demonstrate that wrinkling is a practical method to map the in-plane mechanical anisotropy in OSCs. In addition, we utilize wrinkling to characterize how the elastic modulus of pBTTT (poly(2,5-bis(3-alkylthiophen- 2-yl)thieno[3,2-b]thiophene)) changes with increasing molecular weight, from the monomer to the pentamer and the high molecular weight polymer.

To elucidate the effects of mechanical strain on charge transport, we first demonstrate and quantify the existence of a piezoresistive effect in rubrene crystals by the application of bending strains along its b [010] axis. A piezoresistive coefficient of approximately 11.26 is determined and confirmed through density functional theory (DFT) calculations. Second, we take advantage of wrinkling as a unique way to strain the conducting channel of field-effect transistors in a non-destructive, reversible, and predictable manner. We observe field-effect mobility modulation upon wrinkling and establish that it is controlled by the strain experienced by the insulator-semiconductor interface upon deformation. Finally, we propose a model based on plate bending to quantify the net strain at the insulator-semiconductor interface and predict the change in mobility. These contributions are the first to quantitatively correlate the crystal structure and the mechanical properties of OSCs, as well as the first to study electro-mechanical behavior in OSCs. They also represent a significant step forward in structure-function relationships in organic semiconductors and lay the groundwork for the effective utilization of organic semiconductors in mechanically demanding applications.

TABLE OF CONTENTS

LIST OF TABLES

Table **Page**

LIST OF FIGURES

Figure **Page**

CHAPTER 1

INTRODUCTION

1.1 Project Overview

To effectively take advantage of the exceptional transport properties of crystalline organic semiconductors it is necessary to understand how they respond to mechanical deformations and how mechanical strains affect their electrical properties. From a fundamental perspective, the knowledge of the mechanical properties of organic semiconductors is indispensable to expand our understanding of structure-property correlations and determining the performance limits of single-crystal-based devices. From an applied perspective, the mechanical limits of a material, such as yield point and failure under mechanical and thermal loadings, dictate limits on processing and manufacturing of devices [1]. In addition, knowledge of the strain effects on electrical properties is imperative as a tool for selection of materials for specific strain intensive applications.

Most of the work presented here focuses in organic single crystals (OSCs) of polycyclic aromatic hydrocarbons. Molecular crystals are ideal platforms for the study of intrinsic physical properties and for elucidating structure-property/structure-function correlations in organic semiconductors. Given their well-ordered structure, their purity, and the absence of grain boundaries, OSCs allow almost complete experimental access to the intrinsic properties of the materials in question. Despite the profound knowledge of the structural and electrical properties of OSCs, there is little research on their mechanical properties and the effects of mechanical strain on their electrical properties. Our goal is to fill this void by establishing a framework for the under-

standing of mechanical phenomena in OSCs that is potentially applicable to a larger set of organic semiconductor materials.

The motivation for this dissertation is that the solid state packing of different molecular structures gives rise to different mechanical and electrical properties. We believe that the physical properties arising from different crystal structures should be taken into account when designing the next generation of flexible and conformable electronic technologies. This will have an impact in electronic device architectures and future molecular design strategies of materials tailored for flexible electronic applications. We strive to answer the following fundamental questions: 1) How does molecular structure affect the mechanical response of organic semiconductors? 2) How do elastic moduli relate to electrical properties such as field-effect mobilities? 3) How do homogenous and inhomogeneous mechanical deformations affect the electrical properties of organic semiconductors? The driving hypothesis for this work is that mechanical strains affect crystal structure and therefore, charge transport phenomena. Moreover, the wrinkling instability is a viable tool to characterize the mechanical properties of organic semiconductor materials including the anisotropic elastic constants in OSCs and different moduli emerging from different molecular weights of the same conjugated polymer.

1.2 Background

There are several concepts that are used repeatedly throughout the following chapters and that make up the backbone of the research presented in the present dissertation. In this section we briefly introduce the basics of organic semiconductors, describe the operation of field effect transistors and finally, explain the mechanics of the wrinkling instability.

1.2.1 Organic Semiconductors

Organic semiconductors are a class of carbon-based materials that due to conjugation, alternating single and double carbon bonds, possess the property of electrical conductivity [2]. Organic semiconductors can be used as active materials in electronic devices such as: light-emitting diodes [3, 4], solar cells [5, 6], and field-effect transistors [7,8]. Most organic electronic devices are based on two types of materials, conjugated polymers and small molecules. The chief attractive feature from these types of materials is their processability. Organic semiconductors can be synthesized to be soluble in common solvents which allow them to be easily applied on a variety of substrates, including large-area and flexible substrates at low temperatures [9]. This ease of processing has the potential of lowering the costs of the manufacturing compared to classical semiconductor devices made of inorganic semiconductors such as silicon and gallium arsenide [2].

There are two main models of carrier transport in organic semiconductors: hopping and band transport [10]. Charge hopping occurs between neighboring molecules with strong $\pi-$orbital overlap. The directionality of the $\pi-$orbital overlaps produces charge-carrier mobility anisotropy, which has been characterized and correlated to the crystal structure of many materials [11, 12]. In the hopping regime, charge-carriers can be considered to be localized as polarons on individual molecules. In contrast, the charge-carriers in the band transport regime are delocalized. Although band transport does occur, hopping dominates the transport in most organic semiconductors. Polaron transport is strongly dependent on phonons in the crystal structure, therefore, mobility has been shown to increase as a function of decreasing temperature [10, 13].

Due to the relative ease of fabrication, polycrystalline thin films, from the vapor phase or solution, are most frequently utilized as active layers in organic electronic devices. However, as a result of the inherent grain boundaries and the dependence of the film morphology on processing, it is difficult to create films with reproducible

high mobilities and impossible to characterize the intrinsic properties of the material under study [14]. Single crystals of organic semiconductors are nearly defect free, and thus provide the opportunity to probe the true transport properties of the material without any reduction in performance due to grain boundaries or impurities.

To grow high-purity crystals of macroscopic dimensions from these materials, the process of physical vapor transport (PVT) is often used [15]. Figure 1.1 shows a schematic of the furnace tube used to grow high-quality organic single crystals. A temperature gradient is induced in the furnace using a heating rope. The source organic material is placed in the area with the highest temperature, where it sublimes. The vapor molecules are carried down the temperature gradient by a steady flow of an inert gas, usually argon or nitrogen. The molecules crystallize once they reach a cooler region corresponding to the crystallization temperature of the material. The growth conditions in the furnaces can be easily adjusted. A comprehensive analysis on crystal growth conditions can be found in literature [15]. The quality of the single crystals obtained by PVT has been confirmed using polarized microscopy and diffraction experiments [16].

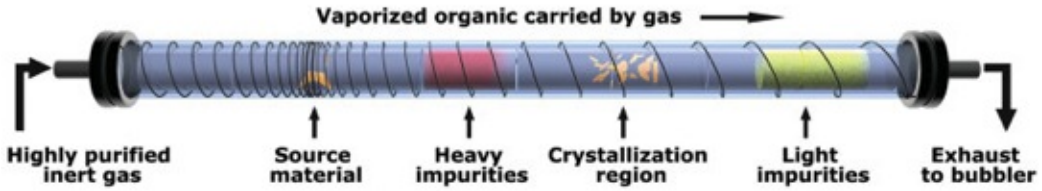

Figure 1.1: Growth of single-crystals from physical vapor transport (PVT). Figure adapted and reprinted from Ref. [17] with permission from Elsevier.

Electronic devices based on OSCs exhibit high-performance and reproducible behavior because of their molecular long-range order. Under the same crystallization conditions, van der Waals forces create the same unit cell in the crystal structure, with few variations due to polymorphs, which are well-documented and easily controlled for

the materials in question [18, 19]. The crystal structure, particularly intermolecular distance, $\pi - \pi$ stacking, and orbital overlap, dictate the electronic coupling throughout the crystal. Orientation of single-crystal semiconductors has a profound impact on their mobilities, as the anisotropy of the crystal structure exhibits varying degrees of orbital overlap and delocalization in different directions [20]. Depending on chemical structure, molecular crystals can have different packing motifs and habits. Molecules that pack face-to-face due to $\pi - \pi$ interactions tend to form one-dimensional nanowire crystals, with their highest mobilities coincident with their longest axes [21]. One notable example of nanowire single crystals is hexathiapentacene (HTP), Figure 1.2a. In hexathiapentacene, the sulfur atoms induce dipoles between each other, creating an intermolecular distance that is smaller than the van der Waals radii of the two atoms [21]. This small intermolecular spacing allows the nanowires to exhibit high mobilities along their long axis [22]. Another typical packing motif is the herringbone exhibited by molecules such as tetracene and pentacene (Figure 1.2b); this crystal structure occurs due to the interaction between the aromatic rings and the edges of the molecules. This herringbone structure creates a less pronounced carrier mobility anisotropy along both in-plane axes of crystallization, and results in two-dimensional crystal platelets [23].

1.2.2 Field-effect Transistors

Field-effect transistors (FETs) are an important component controlling the logic in integrated circuits in virtually all modern electronic devices [24]. FETs are also the main experimental tool to extract the charge-carrier mobilities of semiconducting materials. Charge-carrier mobility is one of the most important figures of merit of organic semiconductors; it determines the performance of organic electronic devices such as field-effect transistors and solar cells [20]. Mobility is defined as the mean velocity of the charge carriers per unit electric field [25]. Figure 1.3 shows the general

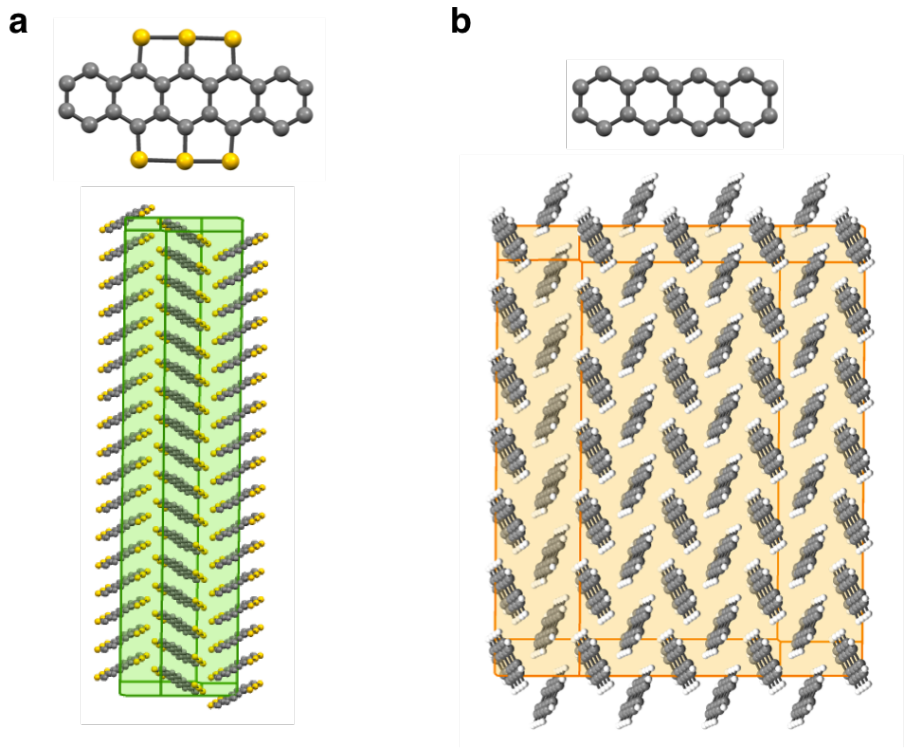

Figure 1.2: Crystal habits. a) π-stacking in hexathiapentacene produces one-dimensional crystals. b) The herringbone structure of tetracene forms a two-dimensional crystal packing.

structure of a transistor. Transistors consist of three electrodes: gate (G), source (S) and drain (D). The active semiconductor material connects the source-drain, and a dielectric layer insulates the gate electrode from the rest of the device. When a voltage is applied to the gate, charge-carriers are induced in the dielectric-semiconductor interface, creating a conducting channel. By applying a bias to the drain electrode a current across the source and drain is generated. The distance between the source and drain is referred to as the channel length (L), while the width is known as the channel width (W). Charge transport in field-effect transistors occurs at the surface of the semiconductor film, as it has been demonstrated that only the first few molecular layers carry the bulk of the current density [26].

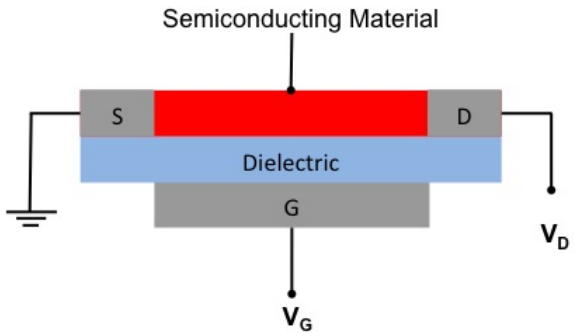

Figure 1.3: General structure of a field-effect transistor (FET).

The field effect mobility of the active layer can be extracted from the drain current at the linear or saturated operation regimes. The difference between these two regimes comes from how homogeneous the effective potential is at the semiconductor-dielectric interface. The voltage at the source will always be equal to V_G. At the drain electrode the voltage is $V_G - V_D$ [8]. In the linear regime (Figure 1.4a) $V_D \ll V_G - V_T$, therefore the electrical potential at the semiconductor-dielectric interface is almost constant and the conducting channel has an uniform carrier concentration from source to drain [24,27]. The current I_D has a linear coupling with V_D in this regime as described in the expression:

$$I_{D,lin} = \frac{W}{L}\mu C_i \left[(V_G - V_T)V_D - \frac{V_D^2}{2}\right] \tag{1.1}$$

where C_i is the capacitance per unit area of the insulating layer, V_G is the gate voltage, V_T is the threshold voltage, and μ is the field-effect mobility.

As V_D is increased, differences in the electrical potentials near the source and drain electrodes become significant and the charge carrier concentration becomes less uniform across the channel. For $V_D \approx V_G$, the voltage at the drain is effectively zero, the channel becomes "pinched" (Figure 1.4b-c) and no further increase in I_D is observed in the output characteristics; this is known as the saturation regime [24]. As V_D is increased above the pinch-off voltage, the pinch-off point slides towards the source electrode. Substituting $V_D = V_G - V_T$ in Equation 1.1 yields the expression

describing the characteristics of a field-effect transistor in the saturation regime:

$$I_{D,sat} = \frac{W}{L}\mu_{sat}C_i(V_G - V_T)^2 \tag{1.2}$$

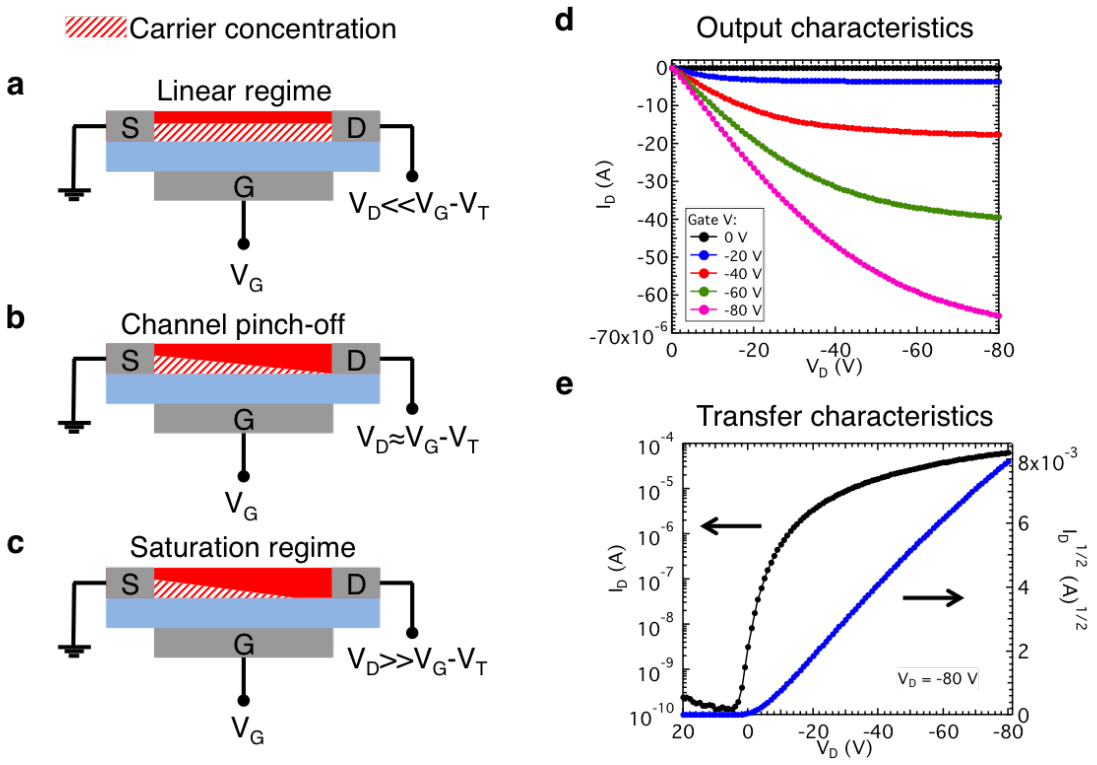

Figure 1.4: Field-effect transistor operation. a-c) Carrier concentration profiles for different operation regimes. d) Output and e) transfer characteristics for representative rubrene single crystal transistor.

Analysis of the electrical characteristics in the saturation regime does not yield an accurate estimation of the field-effect mobility [8]. Trap-dominated transport effects, including gate voltage dependent mobilities will not be captured by Equation 1.2. This is the reason why parameter extraction from the linear regime is preferred and reported at several small V_D values for which little variation of mobility values is expected. It is worth noting that single crystal field-effect transistors rarely show gate voltage dependent mobility [28].

1.2.3 The Wrinkling Instability

To comprehend the formation of wrinkles we must first understand the concept of elastic stability. Consider an ideal beam, made of a linear elastic material and supported at the ends. When a small axial load, F, is applied to one of the ends, the beam is compressed axially and no deflection is observed (Figure 1.5a). In this case, it is said that the beam is in stable equilibrium, as the column returns to its original conformation after the load is removed. When the load is increased such that it equals a critical value, $F = F_{cr}$, the beam may undergo small deflections under small disturbances with no change in the applied force (Figure 1.5b). This is the state of neutral equilibrium. When $F>F_{cr}$, the beam becomes unstable, where it cannot resist the load and fails by buckling [29], as seen in Figure 1.5c.

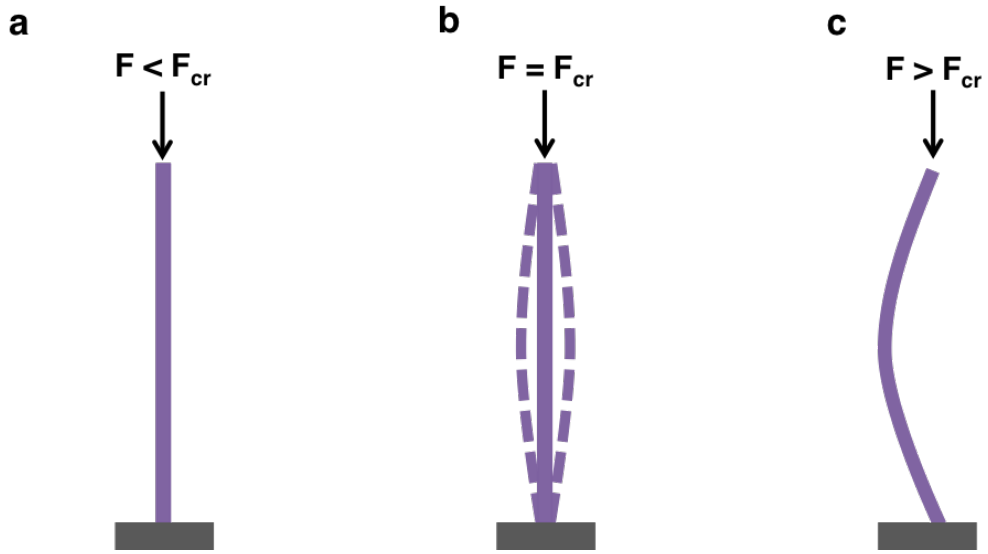

Figure 1.5: Stability of an ideal beam. a) Stable equilibrium. b) Neutral equilibrium. c) Unstable equilibrium.

The analysis of the stability of a buckling beam is analogous to the equilibrium states of a rigid-body system on a smooth surface [29]. As illustrated in Figure 1.6a, a ball on a concave surface is in a state of stable equilibrium, the energy is at a minimum, any application of work will increase the potential energy of the ball. In the case of

stable equilibrium, the ball returns to its original conformation after the disturbance is removed. If the ball is on a flat surface, Figure 1.6b, disturbing it may change its horizontal position but it does not change its potential energy, therefore, it is considered to be in a state of neutral equilibrium. Figure 1.6c represents a state of unstable equilibrium, the energy is at a maximum, thus, any disturbance would reduce the potential energy, making the ball roll down the convex surface.

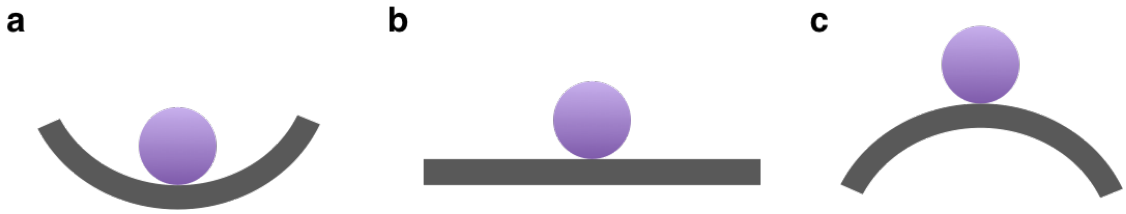

Figure 1.6: Equilibrium of a rigid-body system. a) Stable equilibrium. b) Neutral equilibrium. c) Unstable equilibrium.

Similar a buckling beam, when compressed in-plane above a critical strain value, a thin, stiff film adhered to a thick, soft, elastic substrate may undergo a wrinkling instability. Wrinkling is characterized by the spontaneous formation of periodic patterns that are well defined and predictable. This instability occurs as the balance between the energy required to bend the stiff film and the energy required to deform the soft substrate. The total strain energy of the wrinkling system with an inextensible capping film is given by $U_{total} = U_{film} + U_{substrate}$.

The bending energy of a plate of finite dimensions, U_{film}, is [30]:

$$U_{film} = \frac{E_f h_f^3}{24(1-\nu_f^2)} \int_A d^2\mathbf{y} |\nabla^2 w|^2 \tag{1.3}$$

Where E_f is the Young's modulus of the film, h_f the thickness, ν_f the Poisson's ratio of the film, A is the area and w is the out of plane displacement. For a system undergoing the wrinkling instability under uniaxial stress, we assume a pure sinusoidal

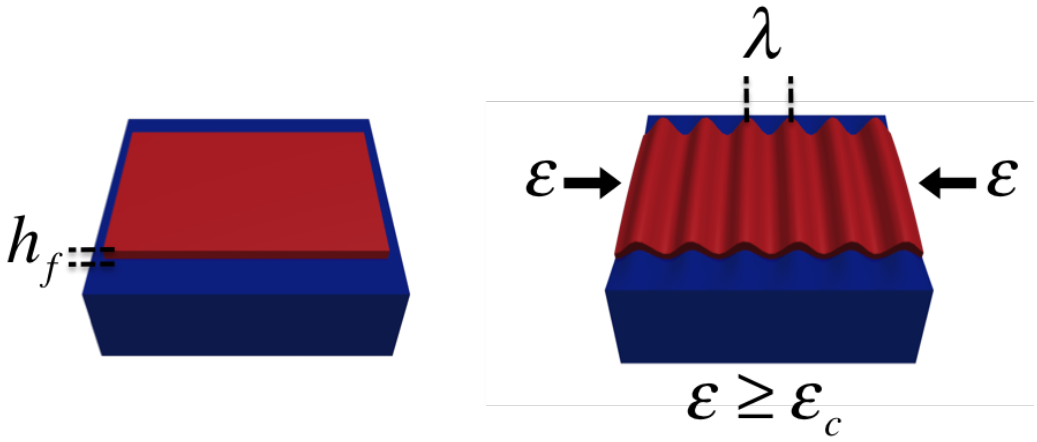

Figure 1.7: A stiff thin film attached to a relatively thick and soft substrate undergoes the wrinkling instability above a critical strain value.

deformation of the surface expressed as: $w(x) = w_0 \cos(kx)$ with wavenumber $k = 2\pi/\lambda$. Equation 1.3 can then be written as Equation 1.4.

$$\frac{U_{film}}{A} = \frac{E_f h_f^3}{48(1-\nu_f^2)} w_0^2 k^4 \tag{1.4}$$

Due to the adhesion of the soft substrate to the buckled film, the soft substrate deforms. Therefore, its deformation energy adds to the total strain energy of the system in the form:

$$\frac{U_{substrate}}{A} = \frac{E_s w_0^2 k}{4(1-\nu_s^2)} \tag{1.5}$$

Where E_s is the Young's modulus of the soft substrate, ν_s the Poisson's ratio and w_0 is the amplitude of the out of plane displacement. The total strain energy of the system can now be written:

$$U_{total} = \frac{w_0^2}{4}\left[\frac{E_f h_f^3 k^4}{12(1-\nu_f^2)} + \frac{E_s k}{(1-\nu_s^2)}\right] \tag{1.6}$$

There exists a characteristic wavelength for which the strain energy of the system is minimized. By minimizing Equation 1.6 with respect to k we obtain the expression

for wrinkling wavelength:

$$\lambda = 2\pi h_f \left[\frac{E_f(1-\nu_s^2)}{3E_s(1-\nu_f^2)} \right]^{1/3} \tag{1.7}$$

The wrinkling wavelength is proportional to the stiff film thickness and the ratio between the mechanical properties of both the stiff film and the soft substrate.

Table 1.1: Elastic moduli of organic electronic materials calculated from wrinkling [31, 32].

Material	**Young's modulus [GPa]**
rr-P3HT	1.33±0.01
pBTTT	1.80±0.345
P3HT/PCBM	6.02±0.03
PEDOT:PSS	2.26±0.05
PANI	0.03
Pentacene	16.09±2.83

Since the wavelength of wrinkles is a function of the mechanical properties of the stiff film and the substrate, it follows that wrinkling can be applied as a tool for mechanical measurements in thin films as long as the modulus of the substrate, the film thickness, and the wrinkle wavelength are known [33, 34]. Recently, the strain-induced buckling instability for mechanical measurements (SIEBIMM) has been used to determine the Young's modulus of polycrystalline thin-films of various organic semiconductors [31, 32]. A summary of their results can be seen in Table 1.1. Moreover, researchers have taken advantage of wrinkled structures as a viable architecture for the fabrication of stretchable devices from ultra-thin buckled ribbons of inorganic materials, where the intrinsic properties of the active materials are not damaged upon stretching [35–37]. The application of wrinkling in semiconductor films is evidence of the critical importance for the field of organic flexible electronics to understand

the effects of wrinkling on the performance of electronic devices. These effects are discussed in Chapter 5.

1.3 Thesis Organization

In Chapter 2, we bring together OSCs and the wrinkling instability. We determine the elastic constants of OSCs of benchmark polycyclic aromatic hydrocarbons (PAHs) using SIEBIMM. We show that molecular packing and characteristic molecular orientations in organic single crystal crystals give rise to anisotropic mechanical properties. Our study centers on benchmark materials in the field of organic electronics: rubrene, PDIF-CN_2 (N,N'-1H,1H-perfluorobutyldicyanoperylene-carboxydi-imide), and their respective molecular cores, tetracene and perylene. Together, they have a wide array of molecular and crystal structures as well as different charge transport properties.

In Chapter 3, we determine the influence of molecular weight on the elastic modulus of oligothiophene films, from the monomer to the pentamer and compare them to the high molecular weight polymer. In addition to the mechanical properties, we investigate the influence of molecular weight in the transport properties of these materials and whether there is any correlation between mechanical and electrical properties as a function of molecular weight.

The effects of homogenous bending deformation on the charge transport properties of rubrene single crystals are discussed in Chapter 4. Due to the weak van der Waals bonds in molecular crystals, we expect global homogeneous deformation to affect crystal structure and therefore, affect molecular orbital overlap between molecules. This is manifested in changes in the resistivity of the crystals.

Finally, after the demonstration that the resistivity of rubrene crystals changes when deformed globally, we focus on studying the effects of local inhomogeneous strains in the overall performance of wrinkled rubrene field-effect transistors in Chapter 5. Changes in field-effect mobility, both increases and decreases, are observed

upon wrinkling. We discovered that this change in performance is dictated by the net strain at the dielectric/semiconductor interface. We propose an analytical model based on plate bending theory to quantify the net strain in wrinkled conducting channels of transistors and predict the change in mobility.

CHAPTER 2

DETERMINING THE ELASTIC CONSTANTS OF ORGANIC SINGLE CRYSTALS

2.1 Introduction

The study of the electrical properties of organic single crystals (OSCs) has provided a better understanding of the charge transport mechanisms in organic semiconductors while opening the doors to a new generation of high-performance electronic devices [10, 11, 38, 39]. Despite the relative high charge carrier mobilities of OSCs, their fragile nature and associated handling difficulty have limited their use to fundamental charge transport studies, where throughput and bendability are not a requirement. Recent advances in the patterning techniques of organic single crystals over large-areas [40, 41], bring new promise for the utilization of these materials beyond charge transport studies, especially in the field of flexible electronics [16, 22]. However, in order to effectively take advantage of the electrical properties of OSCs in flexible devices, their fundamental mechanical properties need to be understood and characterized.

It is well known that physical properties of solids are dictated by the way molecules are arranged and the type of forces that hold them together [42]. The goal of this chapter is to determine the elastic constants that govern the in-plane stress-strain response and correlate measured mechanical properties with crystal structures. We hypothesize that molecular packing and characteristic molecular orientations in organic single crystal crystals gives rise to anisotropic effective in-plane elastic constants that can be measured using the wrinkling surface instability. We investigate the intrinsic

mechanical properties of single crystals from several polycyclic aromatic hydrocarbons (PAHs) (Figure 2.1). Our study focuses on benchmark materials in the field of organic electronics: rubrene, PDIF-CN_2 (N,N'-1H,1H-perfluorobutyldicyanoperylene-carboxydi-imide) and their respective molecular cores, tetracene, and perylene. Together, they have a wide array of molecular and crystal structures as well as different charge transport properties. All these materials can be grown using the physical vapor transport method, producing thin two-dimensional platelets suitable for wrinkling experiments.

Wrinkling was chosen as a suitable metrology tool for mechanical properties due to the dimensions of the as-grown crystals, and due to the technological implications of this surface instability in flexible electronics. Appropriate wrinkling techniques are introduced as part of the experimental approach. For the case of rubrene, the experimental results are complemented with two independent theoretical calculations of the corresponding stiffness matrices. Our results demonstrate a dependence of wrinkling wavelength on crystallographic direction resembling the well-known anisotropic charge-transport properties of rubrene and other molecular crystals. However, the observed elastic anisotropy suggests a there might not be a correlation between mechanical and electrical properties in rubrene crystals. Our findings expand the knowledge of structure-property correlations in organic semiconductors and have the potential to bring insight in the design of organic molecules tailored for strain intensive applications.

2.2 Experimental and Computational Approaches

Crystal growth: Single crystals of all materials shown in Figure 2.1 were grown using the physical vapor transport (PVT) method [15]. All source materials are commercially available and were used as received.

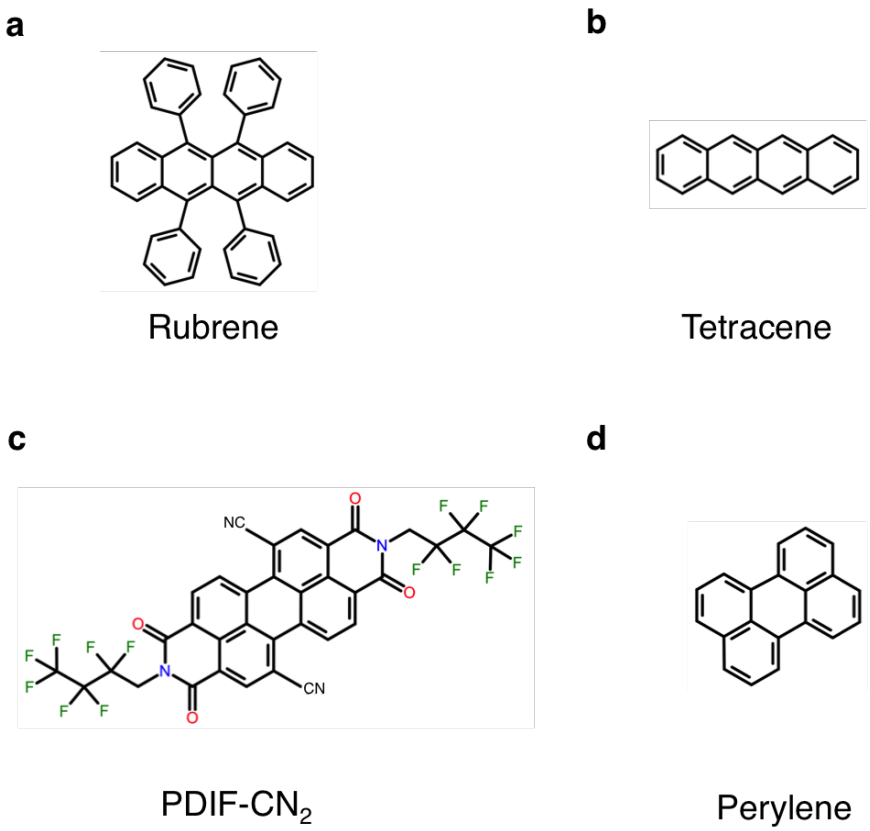

Figure 2.1: Molecular structure of polycyclic aromatic hydrocarbons utilized in this study.

Rubrene (99% Acros Organic™-Thermo Fisher Scientific, Inc) crystals were grown using a fast sublimation rate of the rubrene powder at a source temperature of 330°C under a flow of Argon at a rate of approximately 100 mL min^{-1}. The average time for growth under these conditions was approximately 30 minutes starting from room temperature. Thin (200 nm - 1 μm thick), well-faceted, two-dimensional single crystals, were harvested from these conditions (Figure 2.4b).

Tetracene (98%Sigma-Aldrich ®) and Perylene (99+%Acros Organic™-Thermo Fisher Scientific, Inc) single crystals were grown at a source temperature of 300°C under a flow of Nitrogen at a rate of approximately 100 mL min^{-1}. The average growth time for both materials was approximately 20 minutes starting from room

temperature. These conditions produced two-dimensional tetracene single crystal plates of thicknesses ranging from 300 nm - 1 μm thick. Unlike rubrene, the tetracene crystals obtained were not very faceted, often showing round edges (Figure 2.10b). Well-faceted, two-dimensional Perylene crystals plates of thicknesses ranging from 400 nm - 1 μm thick were harvested from these conditions (Figure 2.16b).

PDIF-CN_2 (N,N'-1H,1H-perfluorobutyldicyanoperylene-carboxydi-imide) (Polyera Activink^{TM}N1100) was obtained from Polyera Corporation. Crystals were grown using a slow sublimation rate at a temperature of approximately 290°C under a flow of Nitrogen of approximately 50 mL min^{-1}. The crystals were grown overnight (approximately 14 hours). These conditions produced well-faceted, two-dimensional single crystal plates with thicknesses ranging from 150 nm - 500 μm thick (Figure 2.13b).

Elastomer substrate preparation: Cross-linked Polydimethylsiloxane (x-PDMS) substrates were prepared by mixing Dow Corning Sylgard 184^{TM}prepolymer and cross-linking agent. Prepolymer/cross-linking agent ratios by mass of 30:1 and 20:1 were used for point contact and mechanical compression experiments, respectively. The mixtures were then degassed in a desiccator under static vacuum for 1 hr. A 30:1 mix was poured into petri dishes to a height of 0.5 cm. The 20:1 mix was poured into cylindrical molds of 1.5 cm of diameter and 2 cm height. Both preparations were cross-linked overnight ($\sim$ 20 hours) at 70°C. The plane-strain modulus, $\overline{E}_s = E_s/(1-\nu^2)$, of the 20:1 substrates ranges from 0.66 to 1 MPa while the 30:1 samples range from 0.38 to 0.45 MPa across the measuring techniques used.

Wrinkling techniques: To induce one-dimensional wrinkling on single crystals, two techniques were developed. In both techniques, crystals are manually harvested from the growth furnace and laminated on x-PDMS substrates. Crystals adhere to the x-PDMS surface by van der Waals forces. In the first wrinkling method (Figure 2.2a), the x-PDMS substrate is deformed by applying a point-like normal load on the elastomer near the edge of the crystal, at approximately 500 μm from the edge

where wrinkles are to be induced. A 200 μm diameter blunt needle was used as a probe to deform x-PDMS substrates. The advancement/regression of the probe was controlled by a piezoelectric nanopositioner operated at speeds of 10 μm/s. The load on the elastomeric substrate generates a radial stress σ_{rr} that deforms the substrate under the crystal; at the same time a compressive stress $\sigma_{\theta\theta}$ develops in the azimuthal direction (Figure 2.2b). Once a critical azimuthal strain is reached, wrinkles develop perpendicular to the desired edge or facet of the crystal. An inverted microscope captures micrographs of the wrinkled films (Figure 2.2c.) Although this technique produces a well-defined and easily controllable radial strain field, it does not provide the freedom to induce wrinkles along any desired direction. Therefore, we complement it with the following technique.

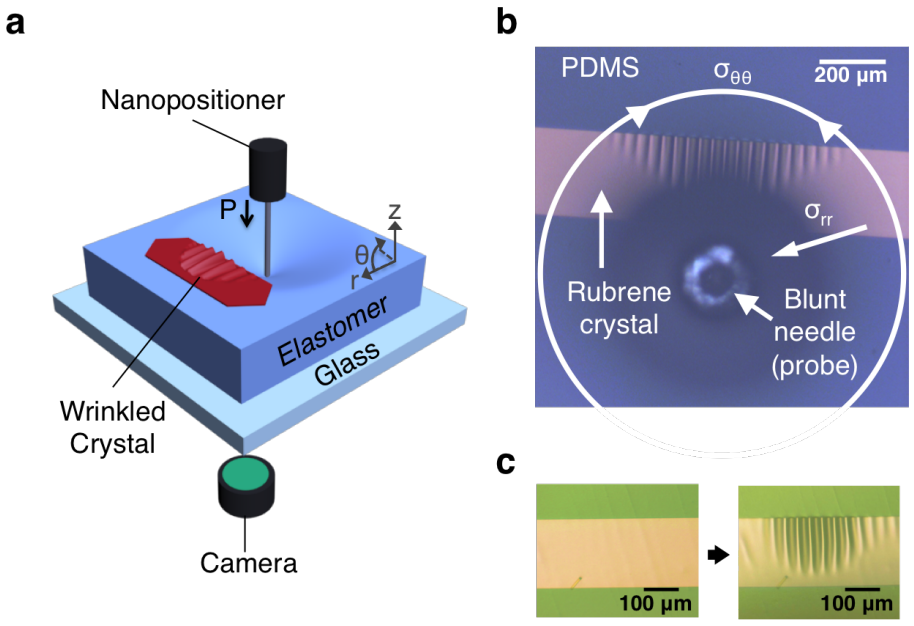

Figure 2.2: Wrinkling technique. a) Schematic of wrinkling by contact point deformation. b) Stresses developed during contact point deformation wrinkling experiments. c) Optical micrographs of a rubrene crystal on x-PDMS before and after wrinkling is induced; the probe is not shown. Figure adapted and reprinted from Ref. [43] with permission from Wiley.

In the second wrinkling technique, the crystal is subjected to in-plane stress by compressing a cylindrical x-PDMS substrate (Figure 2.3a) with a custom-built strain stage composed of two one-dimensional manual translation stages (Figure 2.3b) connected to a manual rotating stage (Newport Corp, Irvine, CA). The x-PDMS cylinder with the crystal laminated to its top surface is placed on a stand between the two translating blocks. As the stand is attached to a rotating stage, the x-PDMS sample is able to be rotated to the precise desired position before compression. At a critical strain, wrinkles develop on the crystal, as shown in Figure 2.3c. Using a cylindrical x-PDMS substrate provides the opportunity to compress the crystal samples along any angle, generating wrinkles along different directions on the crystal.

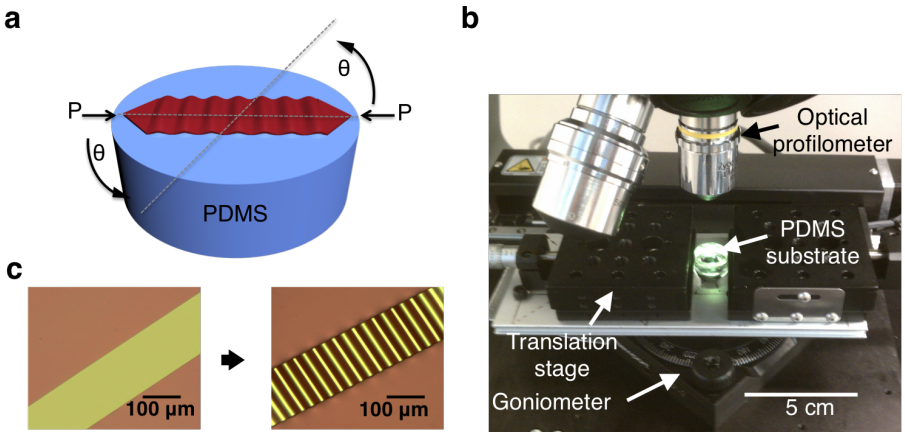

Figure 2.3: Wrinkling technique. a) Schematic of wrinkling by mechanical compression. b) Digital photograph of strain stage. c) Optical micrographs of a rubrene crystal on x-PDMS before and after wrinkling instability is induced respectively. Figure adapted and reprinted from Ref. [43] with permission from Wiley.

Equipment and methods: Crystal thickness and wrinkle topography were measured using optical profilometry (Zygo NewView 7300). A piezoelectric nanopositioner (EXFO Burleigh Inchworn) controlled the vertical displacement of the probe utilized in the contact point deformation wrinkling experiments. Wrinkle wavelengths from the contact point deformation technique were obtained from FFT spectra (Im-

ageJ) of optical micrographs (Zeiss Axiovert 200M, 5x or 10x objective, CCD camera). Wrinkle angles were measured in relation to the b [010] axis of crystals, perpendicular to the wrinkles using ImageJ. In the mechanical compression method, the wrinkle wavelengths were determined by fitting a sinusoidal function to wrinkle profiles obtained using optical profilometry. x-PDMS moduli were measured by uniaxial tensile test (Instron 4411), Dynamic Mechanical Analysis (TA instruments DMA Q800) using a frequency sweep (0.10 Hz 10 Hz) and JKR analysis using a 2 mm diameter flat punch.

Computational methods: Prof. Ashwin Ramasubramaniam (UMass, Mechanical and Industrial Engineering) performed theoretical calculations of the elastic constants of orthorhombic rubrene single crystals using the AIREBO interatomic potential [43, 44] and the optimized Becke88 van der Waals density functional (optB88-vdW) [45].

Crystals of polycyclic aromatic hydrocarbons are molecular crystals, which implies that the bonding is dominated by van der Waals forces. Atomistic calculations of the anisotropic elastic constants were performed in the LAMMPS simulation package. The empirical Adaptive Intermolecular Reactive Bond Order (AIREBO) potential [43, 44], which is parameterized for covalent C-H bonding as well as long-ranged van der Waals interactions, was used to model atomic interactions. From convergence calculations, the cutoff distance for long-range dispersion interactions between atoms was fixed at 10.2 Å. To estimate the nine independent elastic constants, the unit cell of the crystal was perturbed about its ground state by application of uniaxial strains along the three unit vectors as well as shear strains. The tensile and shear strains were restricted to within 0.5% to remain within the regime of linear elastic response. At each level of strain, atomic positions were relaxed with a tolerance of 0.001 eV/Åon the two-norm of the N-dimensional force vector; the corresponding stress components were obtained from the components of the pressure tensor for the

relaxed structure. The elastic constants were computed by fitting the stress-strain data to the constitutive law. Errors in the elastic constants were estimated from the standard errors in the linear fits.

For van der Waals density functional calculations, the tensile and shear strains were restricted to within $\pm 0.5\%$ to remain within the regime of linear elastic response. At each applied strain, atomic positions were relaxed with a tolerance of 0.01 eV/. The elastic constants, C_{ijkl}, were computed by quadratic fits to the strain energy, which is given by $E = E_0 + \frac{1}{2}\Omega_0 C_{ijkl}\epsilon_{ij}\epsilon_{kl}$, where E_0 is the ground state energy of the unit cell of volume Ω_0 and the ϵ_{ij}s are prescribed strains, summations over repeated indices being implied.

2.3 Results and Discussion

2.3.1 Determining the Elastic Constants of Rubrene Single Crystals

The rubrene single crystal (Figure 2.4) is a unique benchmark p-type material in the field of organic electronics. It displays the highest, reproducible field-effect mobilities ($15 - 20\ cm^2/Vs$) [46] and the longest triplet exciton diffusion lengths (2-10 μm) reported [47]. Also, the solid state packing of the molecules in rubrene crystals gives rise to a well-characterized anisotropy in the transport properties [11]. In addition, rubrene possesses an orthorhombic lattice [48], which combined with well-defined facets and the symmetries present in its crystal structure, make it easier to identify crystallographic axes through visual inspection. These characteristics made rubrene single crystals the ideal model system for an in-depth mechanical study to establish the effectiveness of the wrinkling instability to characterize the mechanical response of anisotropic molecular crystals.

A key finding in our investigation was the observation of different wrinkle wavelengths for wrinkles that were induced along different crystal directions. Figures 2.5a and 2.5b show optical micrographs portraying the same crystal as it wrinkles along

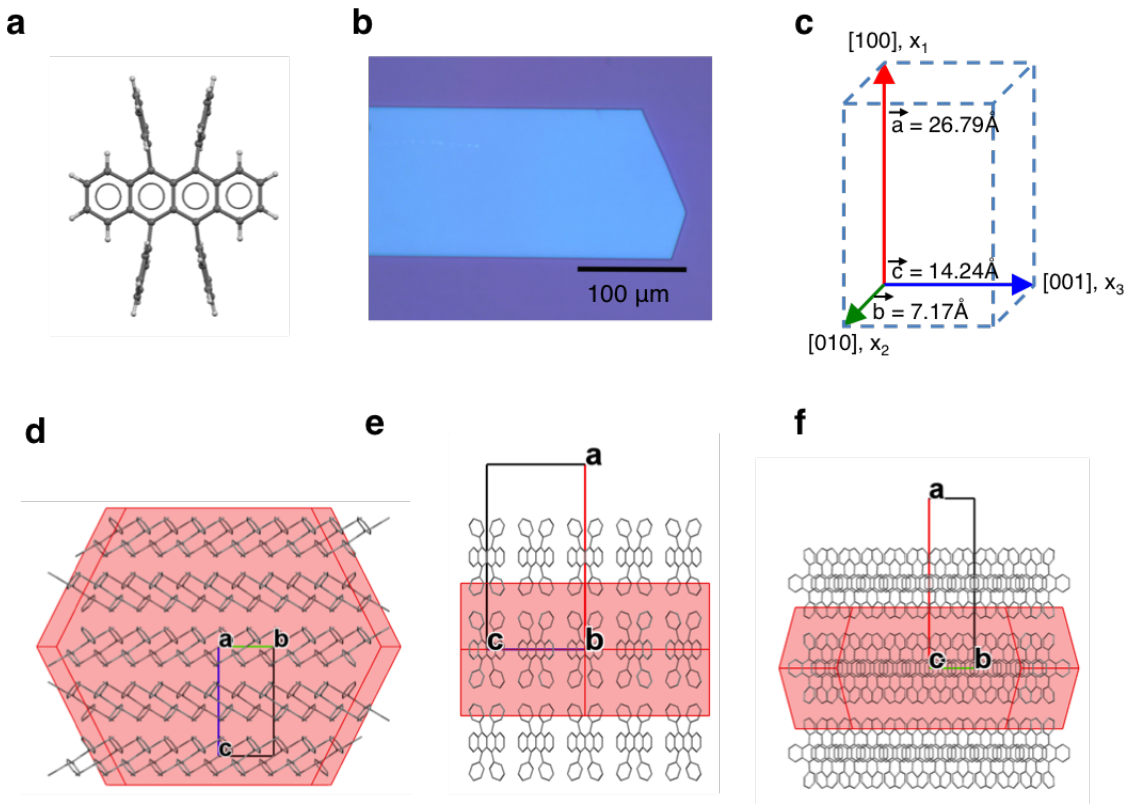

Figure 2.4: Crystal structure of rubrene. a) Molecular structure of rubrene. b) Optical micrograph of ultra-thin rubrene single-crystal plate. c) Unit cell length parameters of orthorhombic rubrene. d-f) Calculated Bravais-Friedel-Donnay-Harker (BFDH) crystal morphology for b-c (100), a-c (010) and a-b (001) faces of Rubrene, respectively. Figure adapted and reprinted from Ref. [43] with permission from Wiley.

the [010] and [001] directions, respectively. Careful analysis of the wrinkle profiles revealed differences in wrinkling wavelengths that are not necessarily evident in the optical micrographs. According to wrinkling mechanics, the observed differences in wrinkle wavelengths suggest differences in the elastic constants along distinct directions of the crystal plane [49].

To understand the underlying mechanics that would give rise to different wrinkle wavelengths, atomistic calculations of the elastic constants of rubrene were performed. From atomistic calculations, the tensor of elastic constants for rubrene was determined to be:

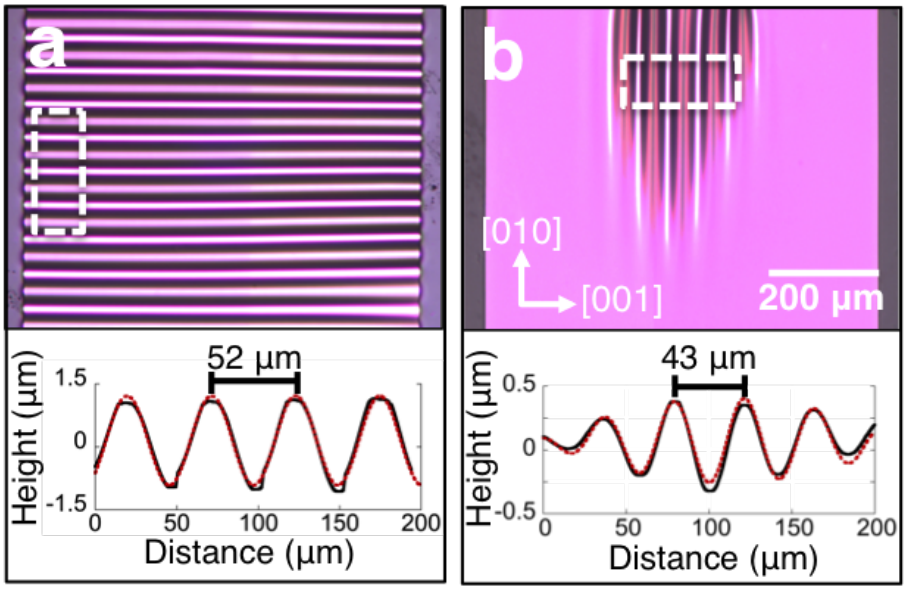

Figure 2.5: Anisotropic wrinkling in rubrene single crystals. a) Optical micrographs and height profile of wrinkles propagating along the [010] direction (b-axis). b) Optical micrograph and height profile of wrinkles propagating along the [001] direction (c-axis) direction of the same crystal in (a). Figure adapted and reprinted from Ref. [43] with permission from Wiley.

$$C = \begin{pmatrix} 15.54 \pm 2.63 & 1.08 \pm 1.48 & 2.08 \pm 1.50 & 0 & 0 & 0 \\ 1.08 \pm 1.48 & 17.85 \pm 1.84 & 10.82 \pm 1.40 & 0 & 0 & 0 \\ 2.08 \pm 1.50 & 10.82 \pm 1.40 & 13.29 \pm 2.41 & 0 & 0 & 0 \\ 0 & 0 & 0 & 2.03 \pm 0.86 & 0 & 0 \\ 0 & 0 & 0 & 0 & 1.97 \pm 0.76 & 0 \\ 0 & 0 & 0 & 0 & 0 & 3.36 \pm 1.42 \end{pmatrix} GPa$$

in a basis with unit vectors e1, e2, e3 aligned along the [100], [010], and [001] axes in Figure 2.4c. Since our wrinkling experiments involve in-plane stresses, the reduced elastic constants that govern the in-plane stress-strain response of the crystals are given by [50, 51]:

$$\overline{C}_{\alpha\alpha} = C_{\alpha\beta} - \frac{C_{\alpha 1} C_{1\beta}}{C_{11}}, \alpha, \beta = 2, 3 \tag{2.1}$$

which are computed to be $\overline{C}_{22(AIREBO)} = 17.77 \pm 1.85$ GPa, $\overline{C}_{33(AIREBO)} = 13.01 \pm 2.44$ GPa, $\overline{C}_{23(AIREBO)} = 10.66 \pm 1.43$ GPa.

The rubrene crystals are modeled as anisotropic thin plates with the [100] axis normal to the plane of the plate. The anisotropic bending moduli $D_{\alpha\beta}$ are then given by

$$D_{\alpha\beta} = \frac{\overline{C}_{\alpha\beta} h^3}{12} \tag{2.2}$$

where h is the thickness of the plate [50]. The bending moduli determined from atomistic simulations can now be employed in the governing Föppl-von Kármán equations for the deformation of a thin anisotropic plate to enable a classical linear stability analysis for buckling. Specifically, for the case of a one-dimensional buckled profile, $w = w_0 \cos k_\alpha x$, the wavenumber k_α can be related to the elastic modulus $\overline{C}_{\alpha\alpha}$ as

$$k_\alpha = \frac{1}{h} \left(\frac{3\overline{E}_s}{\overline{C}_{\alpha\alpha}} \right)^{\frac{1}{3}} \tag{2.3}$$

where $\overline{E}_s = E/(1 - v^2)$ is the plane-strain modulus of the elastomeric substrate with Young's modulus E, and Poisson's ratio v. Using the definition of wavenumber, $k_\alpha = 2\pi/\lambda_\alpha$, Eq. 2.3 may be rewritten as $\overline{C}_{\alpha\alpha} = 3\overline{E}_s (\lambda_\alpha / 2\pi h)^3$. Thus, by measuring the wrinkle wavelengths of crystals of different thicknesses and with the knowledge of the plane-strain modulus of the substrate, the elastic constants of the crystal along different directions on the (100) plane can be determined.

Figure 2.6 shows wrinkle wavelength data obtained from both experimental wrinkling techniques along the [001] and [010] directions. In Figure 2.6, we define a scaled wrinkle wavelength as $\lambda^* = \frac{\lambda}{2\pi} \left(3\overline{E}_s\right)^{\frac{1}{3}}$, which allows us to integrate data obtained from crystals attached to substrates of different moduli. From these experimental results, the in-plane elastic constants for rubrene are found to be $\overline{C}_{22(exp)} = 14.89 \pm 0.73$ GPa, $\overline{C}_{33(exp)} = 9.89 \pm 0.60$ GPa, which are in reasonable agreement with the computed values from atomistic simulations. Moreover, these results are in the same

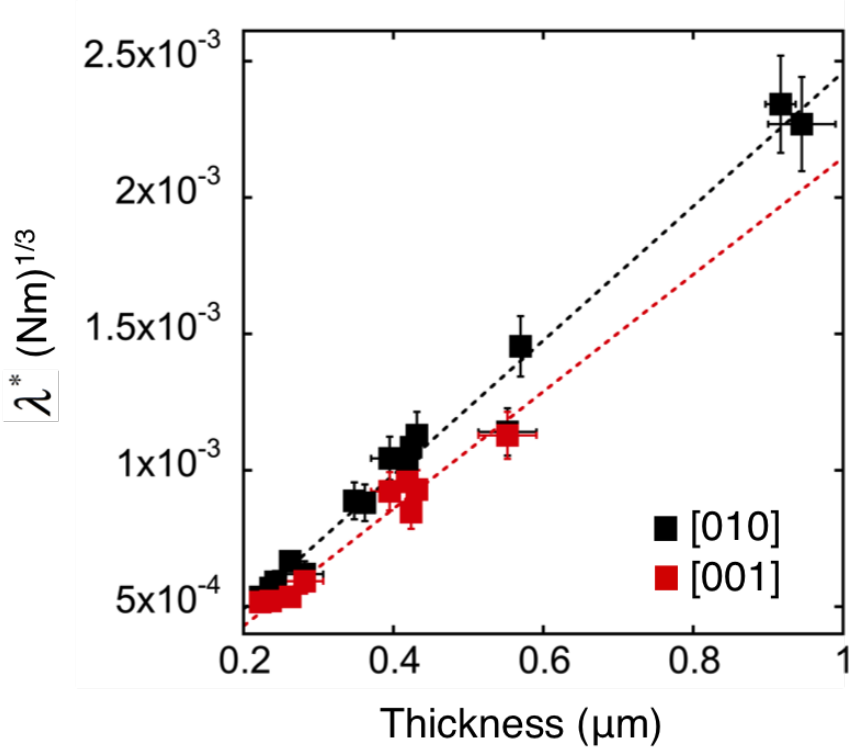

Figure 2.6: In-plane elastic constants determination using a scaled wrinkle wavelength (λ^*) as a function of thickness. The slopes of the fits are 2460.1 and 2146.2 for the [010] and [001] directions respectively. Figure adapted and reprinted from Ref. [43] with permission from Wiley.

order of magnitude as similar thin-film materials as showed in Table 1.1. A summary of results comparing experimental and AIREBO values is shown in Table 2.1 [43].

Table 2.1: Experimental and AIREBO in-plane elastic constants for rubrene single crystals

	$\overline{C}_{22}$ **[GPa]**	$\overline{C}_{33}$ **[GPa]**	**Anisotropy Ratio**
Experiment	14.89±0.73	9.69±0.60	1.51
AIREBO	17.77±1.85	13.01±2.44	1.37

Differences in wrinkling wavelengths along different crystallographic directions provide clear evidence of anisotropic mechanical properties in rubrene single crystals.

In general, the larger elastic constant along the b-axis can be explained by the shorter d-spacing between the aromatic molecules, which translates into stronger cofacial van der Waals interactions; such interactions are not as strong in the perpendicular direction ([001]).

2.3.2 Mapping the Stiffness Anisotropy in Organic Single Crystals

Our experiments with rubrene demonstrate the applicability of wrinkling to detect different effective in-plane elastic constants along the two major crystal axes, b [010] and c [001]. Due to the in-plane anisotropy, we expect the wrinkle wavelength to continuously change for all angles between the major in-plane crystal axes. We now explore the stiffness anisotropy along different angles with respect to the [010] axis for rubrene, tetracene, PDIF-CN_2 and perylene single crystals. This helps us build a visual in-plane stiffness map that facilitate the establishment of new structure-property correlation in PAHs.

2.3.2.1 Rubrene

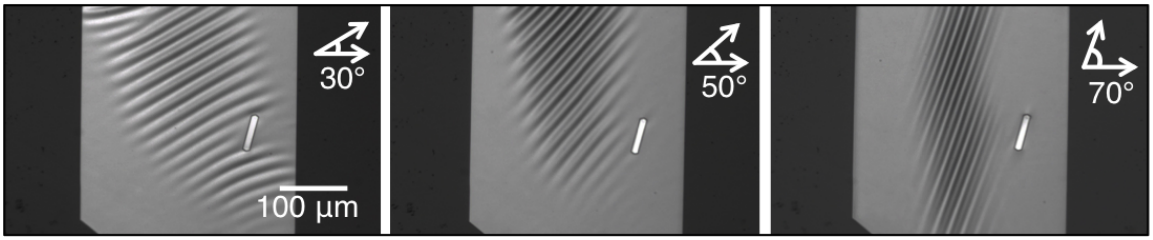

Figure 2.7: Optical micrographs of a wrinkled crystal at different load angles with respect to [010] direction. Figure adapted and reprinted from Ref. [43] with permission from Wiley.

To quantify the mechanical response of rubrene crystals, we systematically examined the buckling of rubrene crystals along different in-plane directions (Figure 2.7). If the sample is loaded along an axis at angle θ measured counterclockwise in-plane

from the [010] axis, the elastic constant in the direction of compression, $\overline{C'}_{22}$, can be defined as

$$\overline{C'}_{22}(\theta) = \overline{C}_{22}\cos^4\theta + \overline{C}_{33}\sin^4\theta + 2(\overline{C}_{23} + 2\overline{C}_{44})\cos^2\theta\sin^2\theta \tag{2.4}$$

such that the buckling wavelength correspondingly varies with orientation as

$$\frac{\lambda(\theta)}{t} = 2\pi\left[\frac{\overline{C'}_{22}(\theta)}{\overline{E}_s}\right]^{\frac{1}{3}}. \tag{2.5}$$

From symmetry considerations in the rubrene crystal structure, it is sufficient to vary the rotation angle θ from 0° $\left[\overline{C'}_{22}(\theta) = \overline{C}_{22}\right]$ to 90° $\left[\overline{C'}_{22}(\theta) = \overline{C}_{33}\right]$ to fully characterize the unidirectional buckling response. By inserting the values from AIREBO calculation for $\overline{C}_{22}$, $\overline{C}_{33}$, $\overline{C}_{23}$, $\overline{C}_{44}$ into Equation 2.4,the predicted plot of $\overline{C'}_{22}$ as a function of angle is obtained (Figure 2.8a). Figure 2.8a also displays experimental values of $\overline{C'}_{22}$ normalized as

$$\frac{\overline{C'}_{22}(\theta)}{\overline{C}_{22}} = \left[\frac{\lambda(\theta)}{\lambda_2}\right]^3 \tag{2.6}$$

The scatter observed at 90° ([001]) in Figure 2.8a can be attributed to the difficulty of obtaining large numbers of waves in the [001] direction for all measured samples. This might be due to edge effects as reported by Rogers and coworkers [52], produced by the limited width of the crystal plate in the [001] direction compared to the [010] direction.

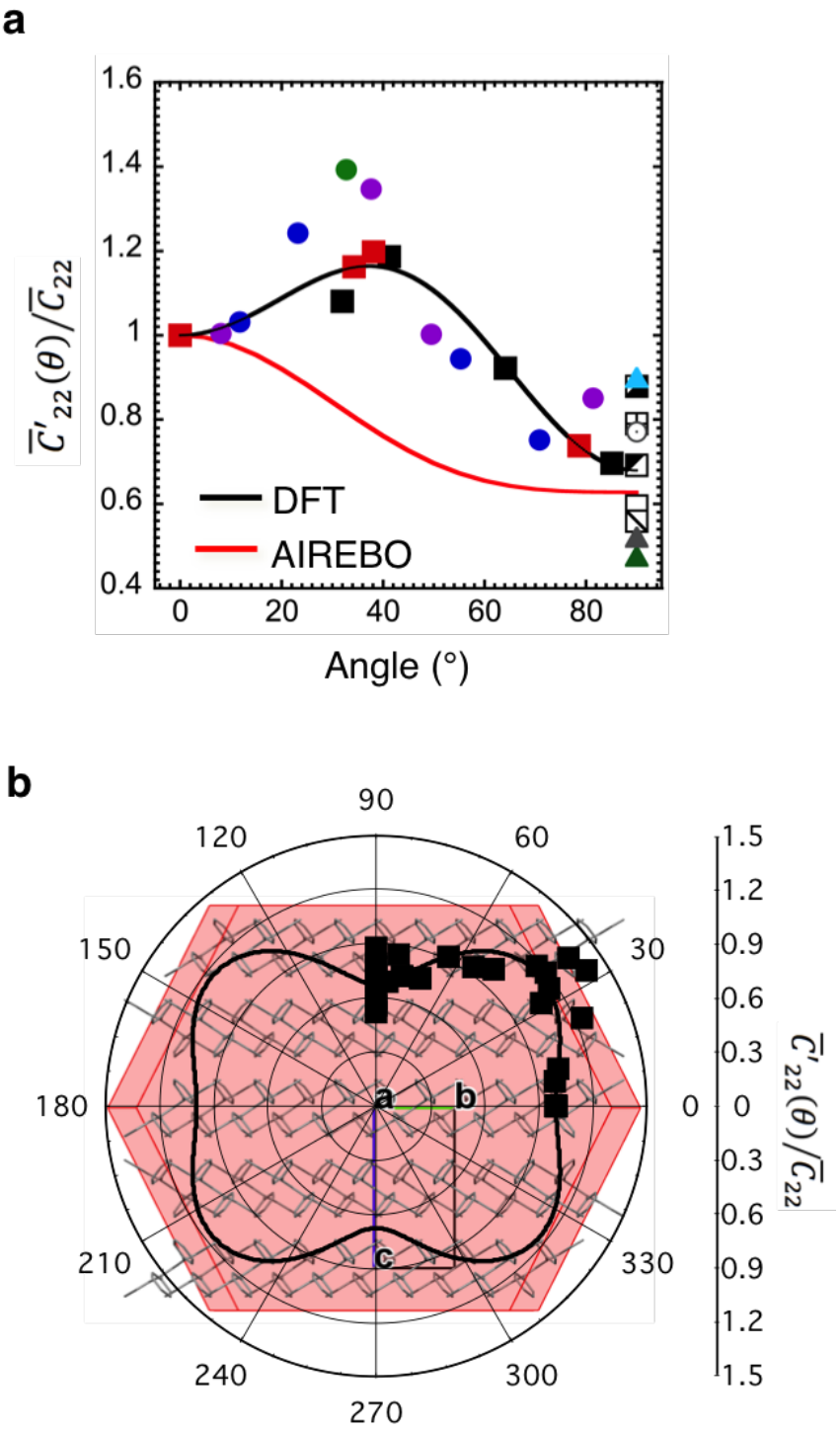

Figure 2.8: In-plane stiffness anisotropy in rubrene single crystals. a) Angular dependence of $\overline{C}'_{22}$ normalized by $\overline{C}_{22}$. Marker shape indicates different substrate modulus. Marker color indicates different crystal sample. b) Polar plot of experimental data in (a) overlaid on structure of (100) face of rubrene. Black line shows Equation 2.4 with elastic constant values from DFT.

We discovered a peak value in the experimental trend of stiffness between $30° - 40°$ with respect to the axis of preferred crystallization (b [010]). Interestingly, the plot of Equation 2.4 using AIREBO values did not agree with the experimental data. New calculations of the nine independent elastic constants of rubrene were carried out using Density Functional Theory (DFT) with state-of-the-art van der Waals exchange-correlation functionals. The revised stiffness matrix for rubrene obtained form these calculations is:

$$C_{DFT} = \begin{pmatrix} 25.65 & 7.71 & 7.98 & 0 & 0 & 0 \\ 7.71 & 15.46 & 7.65 & 0 & 0 & 0 \\ 7.98 & 7.65 & 11.2152 & 0 & 0 & 0 \\ 0 & 0 & 0 & 4.41 & 0 & 0 \\ 0 & 0 & 0 & 0 & 6.66 & 0 \\ 0 & 0 & 0 & 0 & 0 & 3.67 \end{pmatrix} GPa$$

The DFT values differ from those obtained from AIREBO, especially the C_{11} and shear components which are significantly larger in the DFT calculations. The revised effective in-plane constants are $\overline{C}_{22(DFT)} = 13.15$ GPa, $\overline{C}_{33(DFT)} = 8.93$ GPa, $\overline{C}_{23(DFT)} = 5.68$ GPa. These values are in better agreement with experiments. A comparison of the in-plane elastic constants of rubrene obtained from all the different approaches is shown in Table 2.2. The plot of Equation 2.4 using DFT values also shows a better agreement with experimental data (Figure 2.8), showing an intermediate stiffness maximum at $37.32°$.

Table 2.2: In-plane elastic constants for rubrene single crystals

	$\overline{C}_{22}$ [GPa]	$\overline{C}_{33}$ [GPa]	**Anisotropy Ratio**
Experiment	14.89±0.73	9.69±0.60	1.51
AIREBO	17.77±1.85	13.01±2.44	1.37
DFT	13.15	8.93	1.47

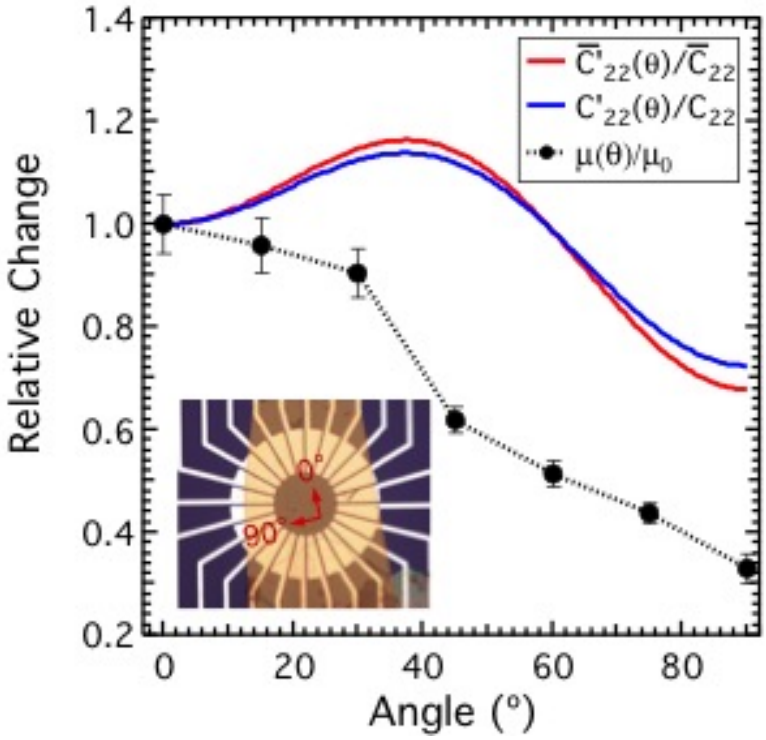

Figure 2.9: Comparison of anisotropic mobility trend and anisotropic elasticity in rubrene

Figure 2.8b shows the experimental data in Figure 2.8a in a polar plot overplayed over the structure of the (100) plane of rubrene together with the stiffness trend using values calculated from DFT. Surprisingly, the buckling wavelength peak observed at approximately 30° in relation to the b-axis corresponds to the angle that the tetracene backbone of rubrene makes with the [010] direction [48]. This angle is known as the pitch in the solid-state packing of rubrene [19, 53]. To date, we do not have an

explanation of the specific molecular interactions responsible for the maximum in-plane stiffness along the pitch angle of rubrene single crystals. We speculate that steric hinderance between the molecules along this direction might be playing a role.

It is well known that the unique packing of the rubrene molecules results in pronounced anisotropic charge-carrier mobilities [11]. Figure 2.9 shows a comparison between the mechanical and electrical anisotropy in rubrene crystals. A stiffness maxima is observed for both normalized $C'_{22}(\theta)$ and in-plane normalized $\overline{C}'_{22}(\theta)$ while the mobility trend shows an almost monotonic decrease in mobility as the angle increases away from the [010] direction. The observation of a peak value for in-plane stiffness not corresponding to the high charge-carrier mobility axis suggests that there is no analytical correlation between mechanical and electrical properties in rubrene crystals. This is expected due to the fact that the elasticity and conductivity tensors have different ranks, four and two, respectively. Nevertheless, explicit correlations between the two properties have been determined for two-pase composite materials by using approximation approaches [54, 55].

2.3.2.2 Tetracene

Tetracene is the backbone of the rubrene molecule. Tetracene crystals are triclinic, with different cell lengths and different cell angles unequal to 90° (Figure 2.10c-f). Compared to the nine independent elastic constants of rubrene, tetracene is expected to have twenty-one. The ultra-thin tetracene crystals tested did not exhibit good edge definition, therefore, polarized microscopy, combined with cleavage orientation was used to identify the b [010] axis. The experimental approach was the same as the one used for rubrene crystals. The wrinkle angles were measured in relation to [010] axis and all wrinkling was induced using the method of mechanical compression of cylindrical x-PDMS substrate (see Section 2.2). Figure 2.11 shows different wavelengths for wrinkles along different angles of the same crystal, indicating mechan-

ical anisotropy. Since the elastic constants of triclinic materials cannot be reduced to in-plane elastic constants by definition [56], we will hereafter refer to the moduli determined using wrinkling as effective in-plane elastic constants.

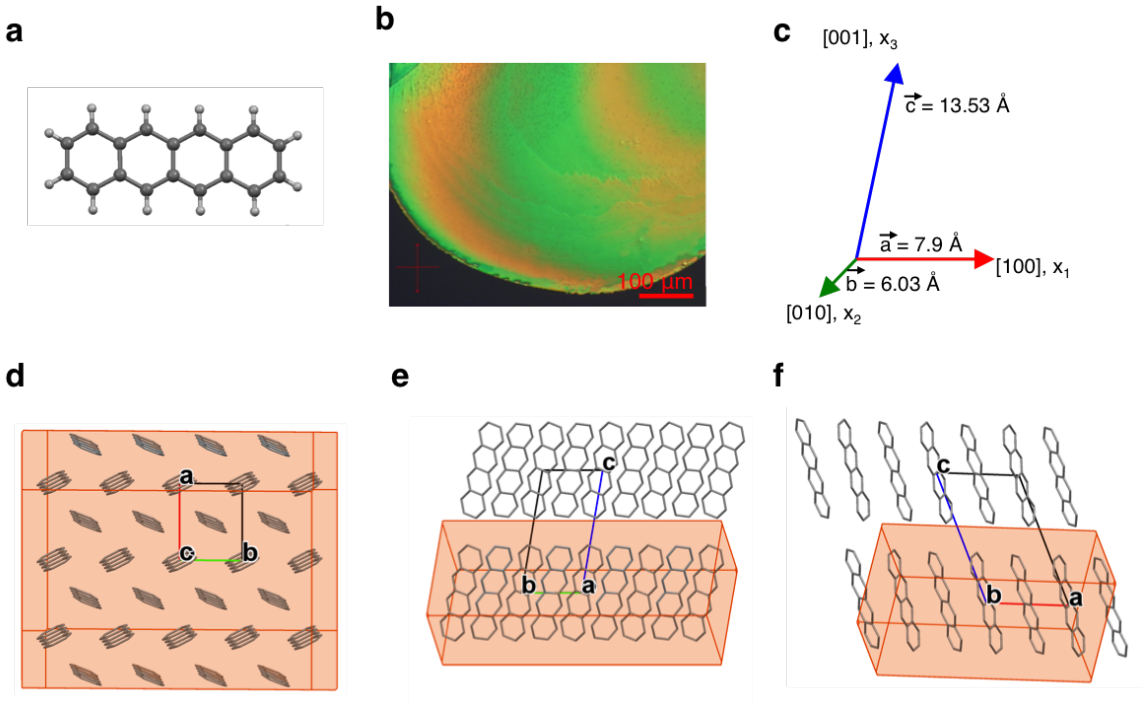

Figure 2.10: Crystal structure of tetracene. a) Molecular structure of rubrene. b) Polarized optical micrograph of tetracene single crystal on x-PDMS substrate. c) Unit cell length parameters of triclinic tetracene. d-f) Calculated Bravais-Friedel-Donnay-Harker (BFDH) crystal morphology for a-b (001), b-c (100) and a-c (010) faces of tetracene, respectively.

The effective in-plane stiffness values as a function of angle are displayed in Figure 2.12. Due to the absence of experimental data between 20° and 40°, we cannot conclusively locate the maximum stiffness. Nevertheless, overlaying the data of Figure 2.12a on the crystal structure on [001] on a polar plot suggests that the maximum might align with the tilt angle of the molecule with relation to the [010] axis (Figure 2.12b). This is similar to our observation in rubrene single crystals shown in Figure 2.8b. In contrast to rubrene, the direction of highest mobility in tetracene does not

correspond to the b-axis, instead it is approximately 45° from it as predicted from a first-principles-based simulation model developed by Goddard and coworkers [12].

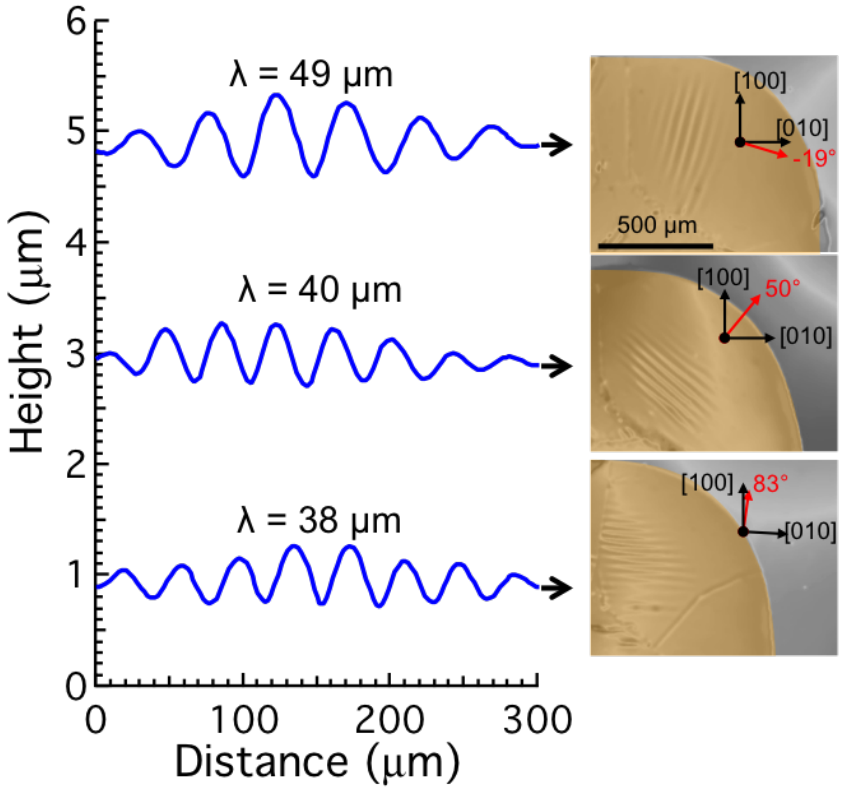

Figure 2.11: Wrinkle wavelength anisotropy in tetracene single crystals. Small differences in wrinkle wavelength are observed along different directions of the (001) crystal plane. Crystal has been colorized for easy identification.

The difference in mobility trend between tetracene and rubrene is due to the different packing and electronic coupling parameters in the two. According to Goddard and coworkers, in rubrene, the highest mobility direction corresponds to the direction with the largest electronic couplings (0°) [12]. Along the [010] axis, the molecules are closer together and the electronic couplings in this direction are much larger and dominate over the influence of other lower coupling values. Therefore, charge transport is higher in the [010] axis. This is not the case for tetracene where the highest mobility direction predicted does not correspond to the direction of largest electronic couplings (50.2°).

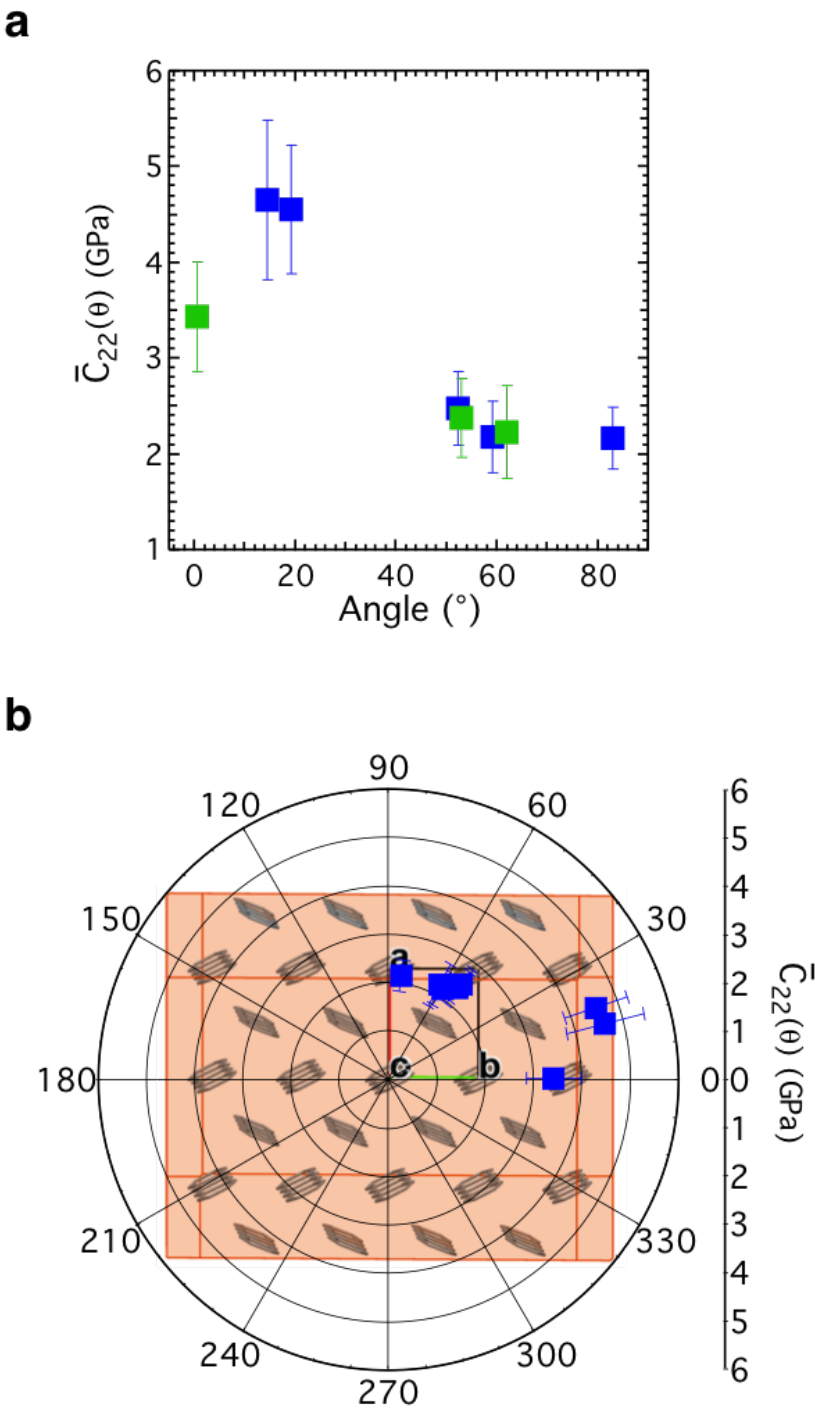

Figure 2.12: In-plane stiffness anisotropy in tetracene single crystals. a) Angular dependence of $\overline{C'}_{22}$. Marker color indicates different crystal sample. b) Polar plot of experimental data in (a) overlaid on structure of (100) face of tetracene.

This is because the electronic couplings of the probable charge hopping paths are closer and their combined effects play a roll in the overall charge transport [12].

We can conclude that an intermediate maximum for tetracene exists in the between the a- and b-axes. Further studies, including theoretical calculations, are necessary to obtain the complete stiffness matrix and accurately determine the angle of highest in-plane stiffness.

2.3.2.3 PDIF-CN_2

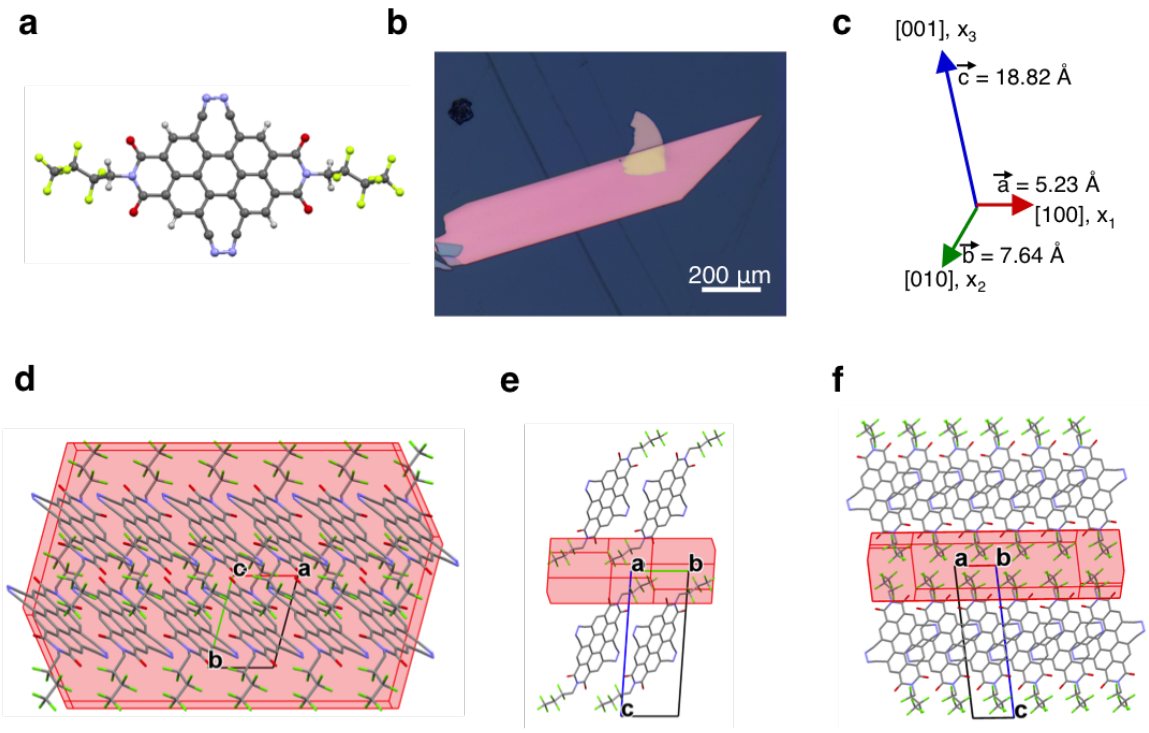

Figure 2.13: Crystal structure of PDIF-CN_2 . a) Molecular structure of PDIF-CN_2. b) Optical micrograph of PDIF-CN2 single crystal on x-PDMS substrate. c) Unit cell parameters of triclinic PDIF-CN_2. d-f) Calculated Bravais-Friedel-Donnay-Harker (BFDH) crystal morphology for a-b (001), b-c (100), and a-c (010) faces of PDIF-CN_2, respectively.

PDIF-CN_2 (Figure 2.13) is the only n-type material in this study. It exhibits exceptional air stability and high electron field-effect mobility (1-6 cm^2/Vs) [57].

Just as in the case of tetracene, PDIF-CN_2 crystals are in the triclinic system (Figure 2.13c). The thin PDIF-CN_2 crystals used in this study exhibited at least two facets from which the crystal orientation was determined.

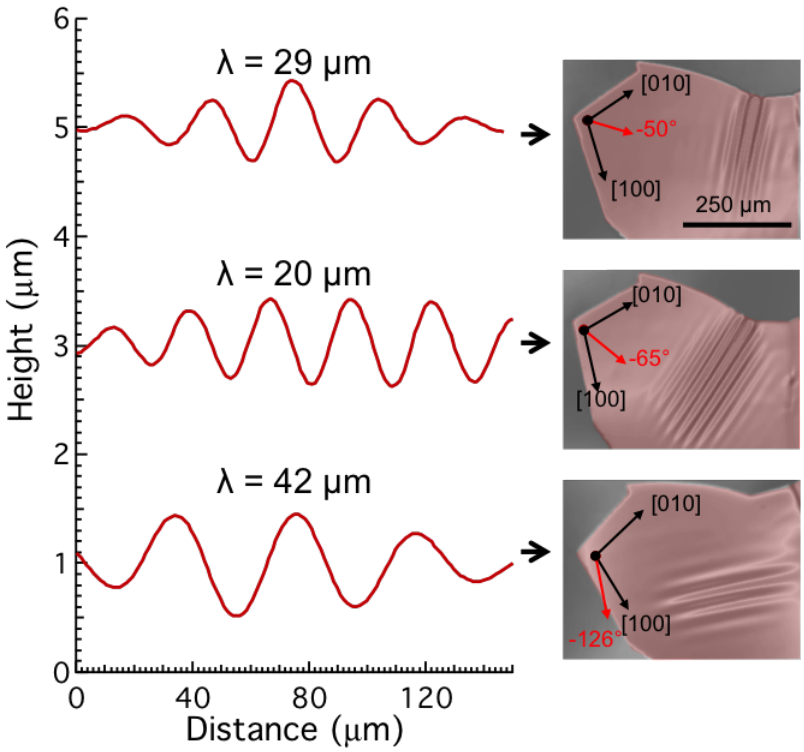

Figure 2.14: Wrinkle wavelength anisotropy in PDIF-CN_2 single crystals. Small differences in wrinkle wavelength are observed along different directions of the (001) crystal plane. Crystal has been colorized for easy identification.

Figure 2.14 shows a comparison of wrinkle wavelengths along different directions of a representative PDIF-CN_2 crystal. The relative differences in wrinkle wavelength are the largest in comparison to the other molecules tested. This is evidence of the large in-plane stiffness anisotropy present. The relative change in $\overline{C}'_{22}$ shown in Figure 2.15a. $\overline{C}'_{22}$ shows a steady increase with increasing angle. Note that, due to the lack of symmetry in the crystal structure of PDIF-CN_2, stiffness data has been plotted for values above 90°. Overlaying a polar plot of the data of Figure 2.15a on the crystal structure of the (001) plane shows that the maxima close to the the tilt angle of

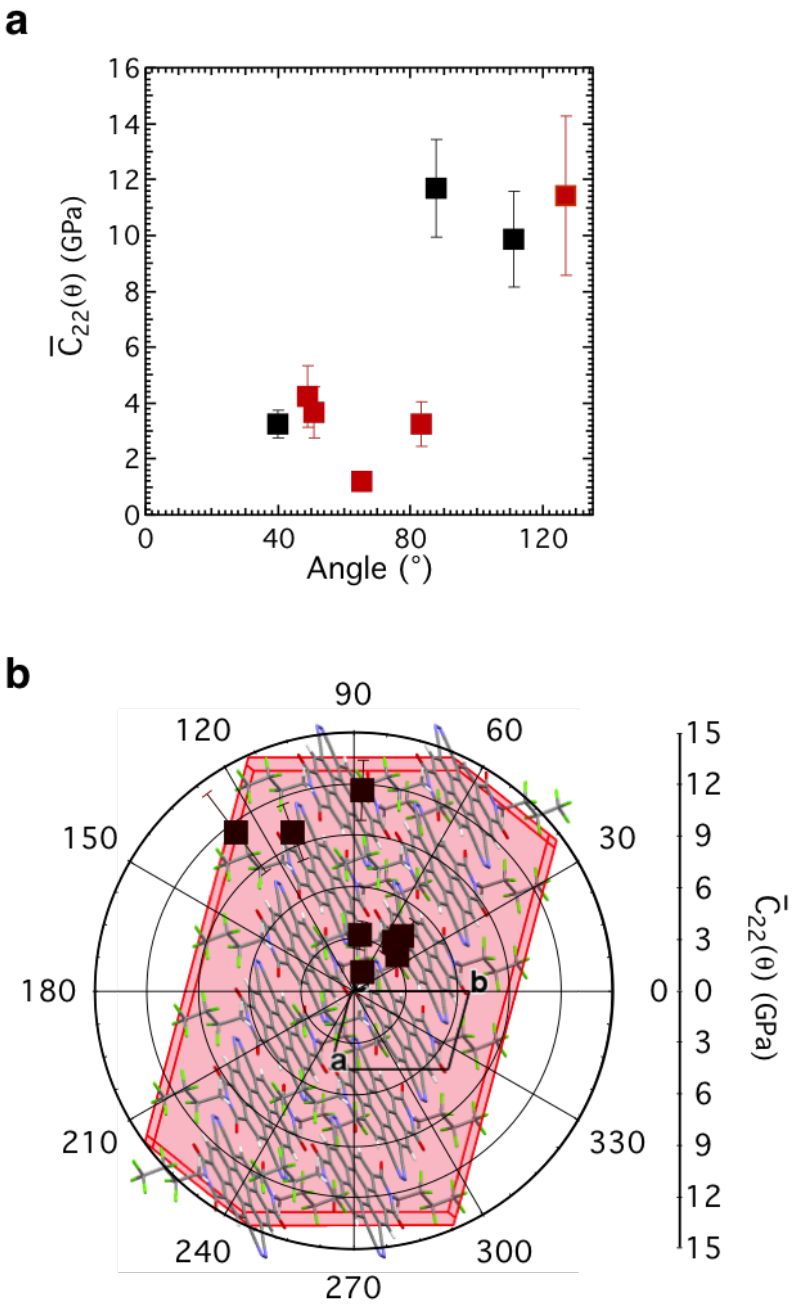

Figure 2.15: In-plane stiffness anisotropy in PDIF-CN_2 single crystals. a) Angular dependence of $\overline{C'}_{22}$. Marker color indicates different crystal sample. b) Polar plot of experimental data in (a) overlaid on structure of (100) face of PDIF-CN_2.

the molecule with relation to the [010] axis (Figure 2.15b). Due to the lack of experimental data between 20° and 40°, we cannot conclusively assign the position of the maximum stiffness.

Although our data does not cover the complete range of angles necessary for the full characterization of this highly asymmetric crystal, we can conclude that there exist significant in-plane mechanical anisotropy in PDIF-CN_2 single crystals. There is currently no field-effect mobility anisotropy data on PDIF-CN_2 crystals to use as a comparison with the mechanical anisotropy trend. Further studies, including theoretical calculations, are necessary to obtain the complete stiffness matrix and accurately determine the angle of highest effective in-plane stiffness.

2.3.2.4 Perylene

Perylene (Figure 2.16) is the core component of the backbone of the PDIF-CN_2 molecule. Perylene crystals are in the monoclinic system and as such have thirteen elastic constants (Figure fig: perycrystc). Figure 2.17 shows a comparison of wrinkle wavelengths along different directions of a representative perylene crystal. The measured wavelength differences are very small compared to the other single crystals studied, making the magnitude of the changes in $\overline{C}'_{22}(\theta)$ the smallest in this study.

Although perylene crystals show well-defined facets (Figure fig: perycrystb) the [010] direction was not easily identifiable. The b [010] axis can be identified by visual inspection in narrow crystal such as the one in Figure 2.16b. The wide and thin crystal needed to perform angle-dependent wrinkling experiments have a lower lateral aspect ratios, making it difficult to differentiate the a [100] from b [010] axis by visual inspection. Here, we take advantage of the fact that both the a [100] and b[010] axes make a 45° angle with the crystal edges (Figure 2.16d). All our measurements consider 0° to be 45° from any edge. Figure 2.18 shows the data of the four crystals tested. Positive angles correspond to directions measured counter-clockwise from the

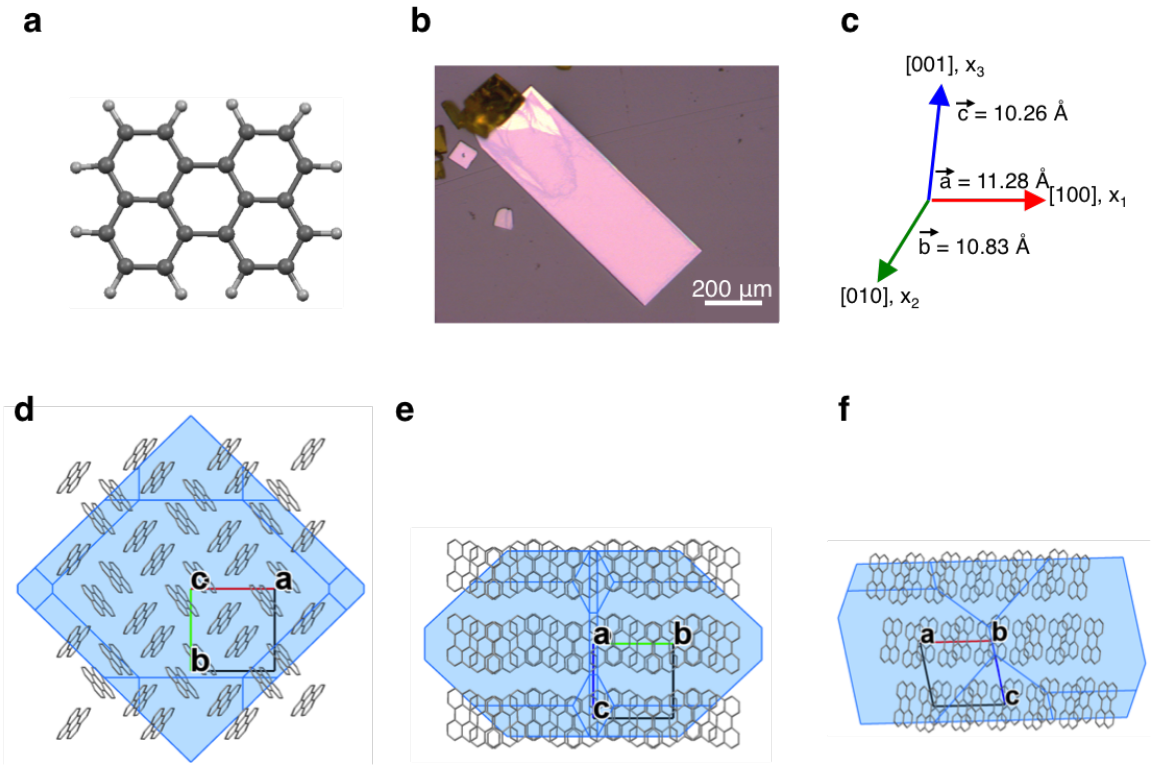

Figure 2.16: Crystal structure of perylene. a) Molecular structure of perylene. b) Optical micrograph of perylene single crystal on x-PDMS substrate. c) Unit cell parameters of monoclinic perylene. d) BFDH crystal morphology for (001) face of perylene. d-f) Calculated Bravais-Friedel-Donnay-Harker (BFDH) crystal morphology for a-b (001), b-c (100) and a-c (010) faces of perylene, respectively.

reference edge and negative values correspond to angles measured clockwise. With this method, the wrinkling data collected from different samples seems to follow a symmetric trend with a maximum wrinkling wavelength measured at $\pm 45°$. Using this symmetry, the data in Figure 2.18 can be replotted from 0° to 90° as shown in Figure 2.19. From these results, the in-plane elastic constants for perylene can be estimated as $\overline{C}_{22(exp)} = 8.0 \pm 1.16$ GPa and $\overline{C}_{11(exp)} = 8.98 \pm 1.31$ GPa. Since no wrinkles aligned perfectly with the b [010] axis($\theta = 0°$), the $\overline{C}_{22(exp)}$ value was determined from the wrinkles closest this axis, $\theta = 7.15°$.

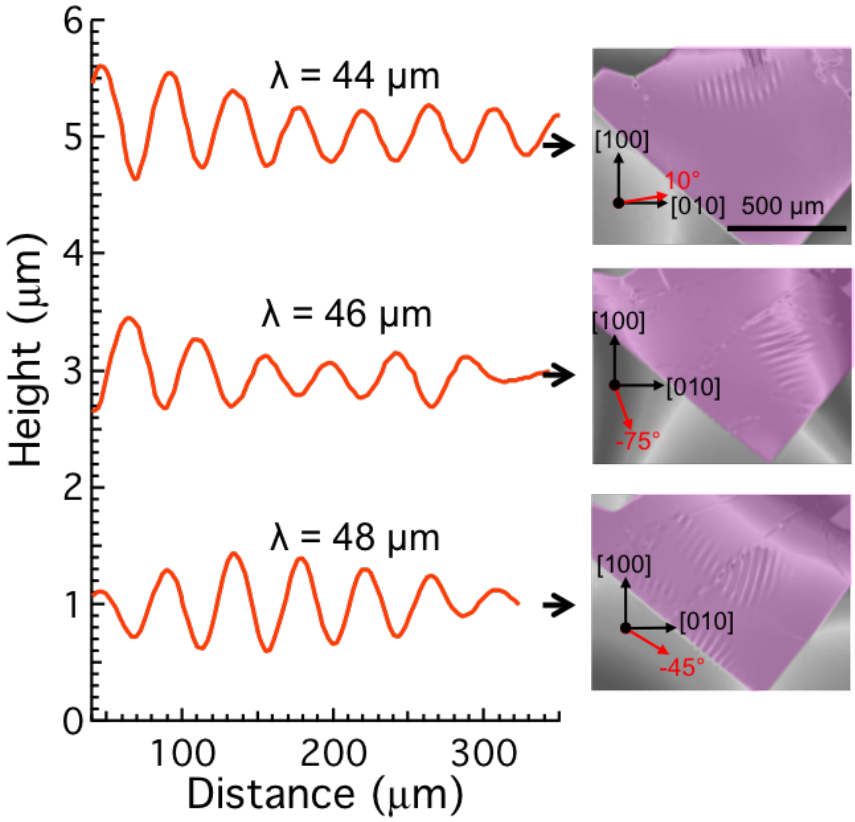

Figure 2.17: Wrinkle wavelength anisotropy in perylene single crystals. Small differences in wrinkle wavelength are observed along different directions of the (001) crystal plane. The crystal has been colorized to facilitate identification.

Overlaying the data of Figure 2.19a on the crystal structure of the (001) plane on a polar plot shows that the maxima aligns with the tilt angle of the backbone of molecule with relation to the [010] axis (Figure 2.19b) . The existence of a maximum stiffness measured close to the pitch angle of the perylene crystal is compatible with our results in rubrene single crystals (Figure 2.8).

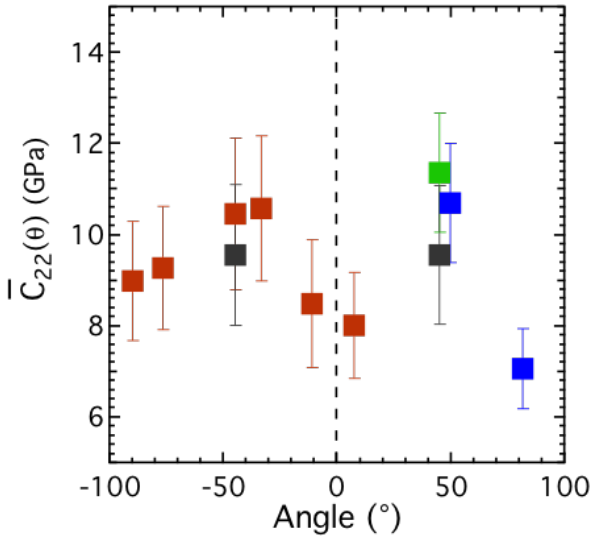

Figure 2.18: $\overline{C}'_{22}$ as a function of angle for different crystal samples.

Our results demonstrate small in-plane mechanical anisotropy in perylene single crystals, with a maximum stiffness measured close to 45° in relation to the b [010] direction. Although the existence of anisotropic mobility has been demonstrated in perylene single crystals [58], a systematic study of the angular dependence of mobility has not been published. We can note that the mobility measured by Lee et al. along the b [010] axis is $9.62 \pm 0.50x10^{-4}cm^2/Vs$, is higher than that along two different non-specified angles, $3.62 \pm 0.04x10^{-5}cm^2/Vs$ and $1.04 \pm 0.23x10^{-4}cm^2/Vs$. This suggests that the trend of mobility as a function of angle might be different from that of the stiffness, similar to the trends observed in rubrene single crystals.

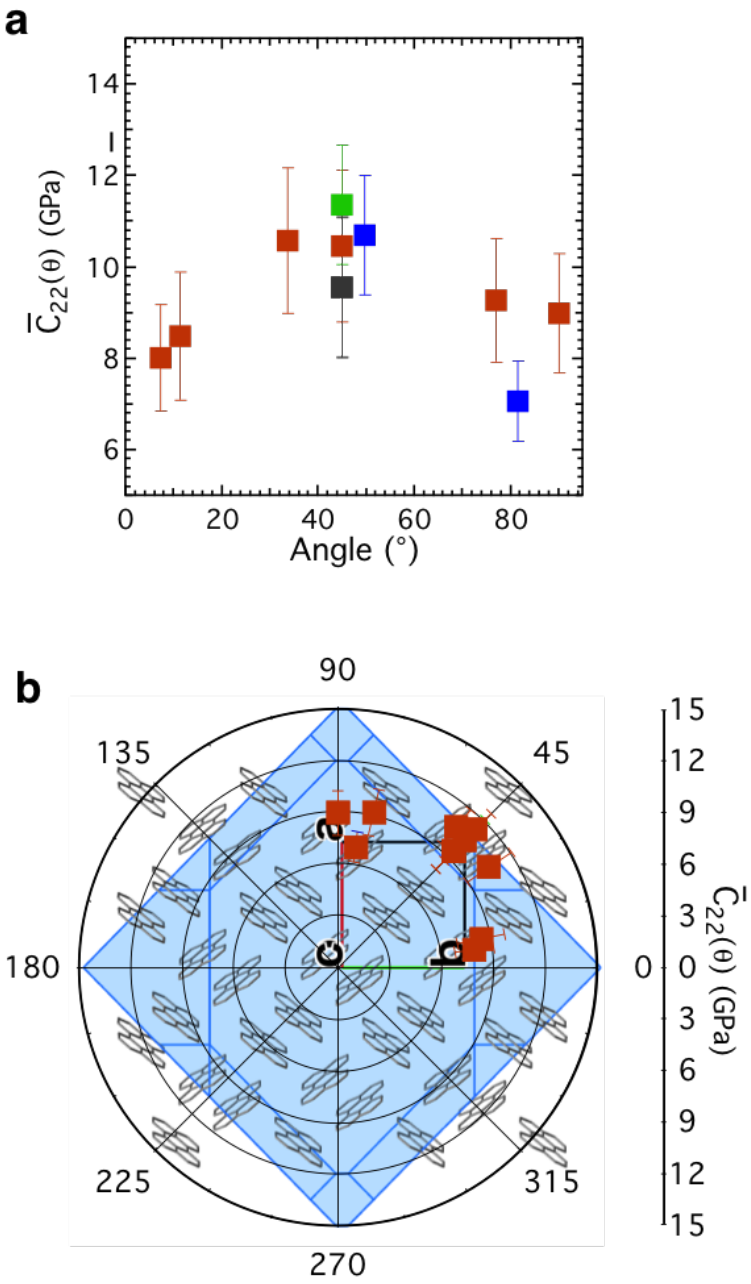

Figure 2.19: In-plane stiffness anisotropy in perylene single crystals. a) Angular dependence of $\overline{C'}_{22}$. Marker color indicates different crystal sample. b) Polar plot of experimental data in (a) overlaid on structure of (100) face of perylene.

2.4 Summary

In summary, the anisotropic mechanical properties of organic single crystals were characterized. By utilizing wrinkling as a metrology tool for mechanical properties we were able to extract the in-plane elastic constants and map the in-plane stiffness anisotropy of rubrene, tetracene, PDIF-CN_2 and perylene single crystals. A summary of the in-plane elastic constants for all single crystals studied is shown in Table 2.3. For rubrene and perylene, a peak value for the in-plane stiffness is found to be maximized at approximately 30°, aligning with the pitch angle that the backbone of molecule makes with the [010] direction. Surprisingly, there appears to be a similar trend in tetracene and PDI-CN_2, correlating the maximum stiffness and the orientation of the molecular backbone in relation to the b [010]. This discovery might suggest a previously non-realized link between mechanical properties and crystal structure in organic semiconductors.

The experimental results for rubrene were complemented with theoretical calculation of the nine independent elastic constants of rubrene using the methods of empirical hydrocarbon potentials and density functional theory. The values obtained through these calculations agree well with the in-plane elastic constants determined experimentally. However, the trend of wrinkling wavelengths as a function of loading direction does not agree with AIREBO results. DFT results do capture the angular trend of in-plane stiffness in rubrene. This difference between the AIREBO and DFT results represent an important lesson that will be helpful in future calculations of the elastic constants of other molecular crystals.

Table 2.3: Summary of effective elastic constants for organic single crystals

Material	Approach	$\overline{C}_{22}$ [GPa]	$\overline{C}_{33}$, $\overline{C}_{11}$ [GPa]	Anisotropy Ratio[1]	Anisotropy Ratio Max.[2]
Rubrene	**Experiment**	14.89±0.73	9.69±0.60	1.51	2.92
	AIREBO	17.77±1.85	13.01±2.44	1.37	1.37
	DFT	13.15	8.93	1.47	1.71
Tetracene	**Experiment**	3.43±0.6	[3] 2.17±0.32	1.58	2.14
PDIF-CN$_2$	**Experiment**	-	-	-	9.5
Perylene	**Experiment**	[4] 8±1.16	8.98±1.31	0.89	1.61

[1]Ratio between in-plane elastic constants: $\overline{C}_{22}/\overline{C}_{33}$ or $\overline{C}_{22}/\overline{C}_{11}$ depending on the unit cell orientation. [2] $\overline{C}'_{22max}(\theta)/\overline{C}'_{22min}(\theta)$, [3] Obtained at $\theta = 82.8°$, [4] Obtained at $\theta = 7.15°$.

In view of the absent research on the mechanical properties of organic crystals, our work represents a significant step forward in structure-property relationships in organic semiconductor materials. Our results are of special significance in developing a comprehensive picture of the inter-molecular potential that governs mechanical and electrical properties in organic semiconductors. Our methods for determining anisotropic moduli will have broad applicability not only to organic crystals, but to polycrystalline and composite films as well.

2.5 Open Questions

Although this chapter answered several questions regarding the mechanical properties of organics single crystals, other questions remain unanswered. Mainly, which specific molecular interactions are the origin of mechanical anisotropy observed, par-

ticularly the apparent stiffness maxima along the direction the planar backbone? Is this a property inherent to all PAHs single crystals? Is this a general result for all organic crystals with planar backbone?

In addition, it will be necessary to perform theoretical calculations of the elastic constants of tetracene, perylene and PDIF-CN_2 to obtain a deeper understanding of the mechanics governing the deformation of the crystals and to confirm the stiffness trends presented in our experiments. The ease to perform these calculations on materials with low or no symmetry remains a question.

Finally, how can we take advantage of this knowledge in order to design high-performance organic semiconductor molecules with tailored mechanical and electrical anisotropy? We are certain that, in the near future, these questions will be part of important research efforts throughout the organic electronics community.

2.6 Acknowledgements

We thank Prof. Ashwin Ramasubramaniam (UMass, Mechanical and Industrial Engineering) for performing atomistic and quantum mechanical calculations of elastic constants. We also acknowledge, Niva Ran who during her time as a undergraduate researcher assisted in the initial wrinkling experiments with rubrene.

CHAPTER 3

MOLECULAR WEIGHT DEPENDENCE OF IN-PLANE ELASTIC MODULI AND FIELD-EFFECT MOBILITY IN OLIGO- AND POLY-THIOPHENE FILMS

3.1 Introduction

It is well known that both electrical and mechanical properties are defined by the molecular structure and the way molecules arrange in the solid state. In semicrystalline polymers, as molecular weight increases, crystals change packing conformation from extended chains to folded and entangled chains [59]. Using this principle, we aim to provide new insights into the connections between parameters controlling electrical and mechanical properties in polythiophene systems and explore the dependence of these properties as a function of molecular weight.

Here, we study the influence of molecular weight on the elastic modulus and field-effect mobility of poly(2,5-bis(3-alkylthiophen- 2-yl)thieno[3,2-b]thiophene) (pBTTT). PBTTT is of interest due to alkyl chain interdigitation between neighboring lamellae, which promotes the formation of closely-packed, well-ordered structures [32, 60]. The solid-state molecular order in pBTTT translates into high field-effect mobility in the range of 0.1-0.3 cm^2/Vs [32]. Our study focuses on oligomers of the BTTT repeat unit, from the monomer (BTTT-1) to the pentamer (BTTT-5) and a high molecular weight polymer. Just like in the previous chapter, wrinkling is chosen as the ideal method for the characterization of the mechanical properties of BTTT films.

3.2 Experimental Approach

Preparation of films: Bare Si wafers slides were cleaned in four 20 minute ultrasonication steps in the following order: 1) Mucasol®/DI water solution, 2) DI water, 3) acetone, 4) isopropanol, followed by a drying step with dry air gun.

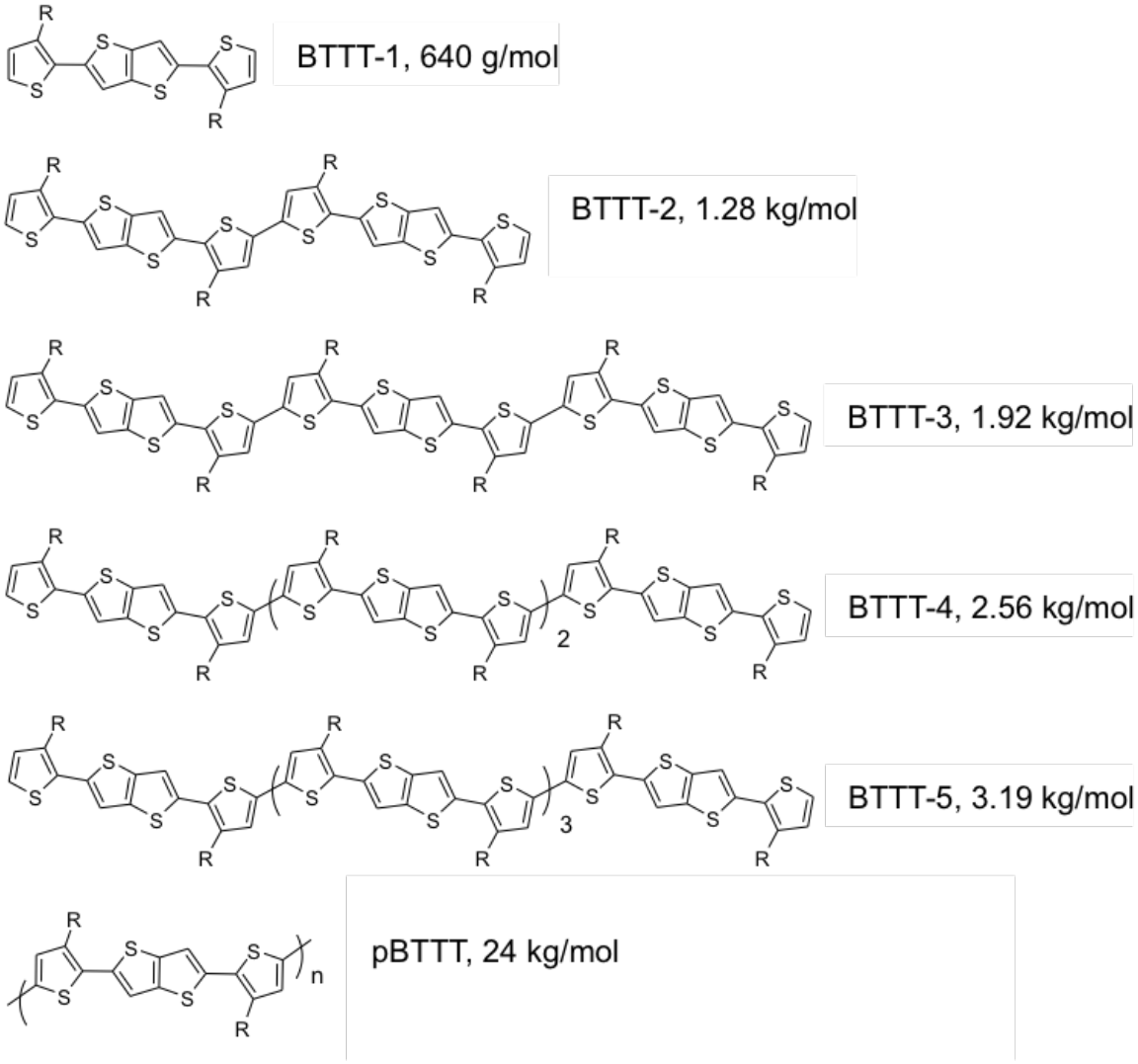

Figure 3.1: Chemical structures of BTTT series. R = $C_{12}H_{25}$.

2%poly(Acrylic acid) (PAA)/DI water solution was spin coated at 4,000 rpm for 60 seconds. PAA-coated Si was annealed at 100° C for 1 hour to eliminate excess water. BTTT-1,2,3,4,5 (Figure 3.1) were synthesized as reported by Zhang et al [60].

Oligomer solutions were prepared in chlorobenzene in concentrations from 10 - 20 mg/mL . Polymer solutions were prepared in dichlorobenzene/chloroform mixed at a 6:1 volume ratio, in concentrations of 10 and 20 mg/mL. The solutions were spin-coated at 750 to 2,000 rpm. BTTT-4, BTTT-5 and pBTTT solutions were warmed-up with a heat gun until the material was completely dissolved before spin-coating.

Transfer to elastomer substrate: x-PDMS substrates were prepared by mixing Dow Corning Sylgard 184 prepolymer and cross-linking agent in a 20:1 ($\overline{E}_s \approx 0.66$ MPa) and 40:1 ($\overline{E}_s \approx 50$ KPa) mass ratio using the same conditions introduced in Section 2.2. The BTTT/PAA/Si was stamped to the surface of x-PDMS and partially submerged in DI water to dissolve the PAA. After PAA is dissolved, BTTT film is transferred to x-PDMS (see Figure 3.2).

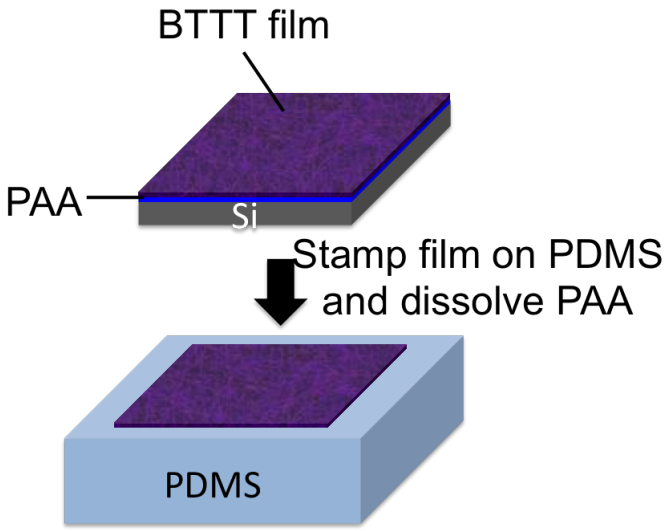

Figure 3.2: Transfer of BTTT film to x-PDMS.

Transistor Fabrication: Si/SiO_2 substrates were cleaned using the same procedure described above. 5 nm of Cr and 40 nm of Au were thermally evaporated through a shadow mask to form bottom contact source and drain electrodes with a length of 100 μm and width of 3 mm. The BTTT 2,3,5 and pBTTT solutions de-

scribed above were used to spin-coat films at 2000 rpm for 45 seconds on the bottom contact electrodes. Subsequently, the insulating layer was formed by spin-coating undiluted CYTOP®(Asahi Glass) directly on the BTTT using two spin steps: 1) 500 rpm for 20 seconds, 2) 2500 rpm for 60 seconds. $\sim 1\mu$m thick film of CYTOP was was obtained with this conditions. The CYTOP was annealed overnight at 40°-50° C in a vacuum chamber. Finally, a 40 nm Au film was thermally evaporated on the CYTOP to act as gate electrode.

BTTT-4 films, were spin-coated from a 10 mg/ml solution in chlorobenzene on PSSA at 2000 rpm for 30 seconds. The film was transferred onto the OTS-SiO_2 by dissolving the PSSA with DI water. Au source and drain electrodes were deposited using a shadow mask.

Equipment and methods: Film thickness was measured using optical profilometry (Zygo NewView 7300). Wrinkle wavelengths were obtained from FFT spectra (ImageJ) of optical micrographs (Zeiss Axioscope A1 with 5x, 10x, 20x objective, with Zeiss ICc1 camera). x-PDMS moduli were measured by uniaxial tensile test (Instron 4411) at a rate of 0.2 mm/sec. Transistor characteristics were measured at room temperature under atmospheric condition a Keithley 4200-SCS and Signatone Micromanipulator H-150 probe station.

Wrinkling experiments were conducted by applying mechanical compression using a strain stage as introduced in Section 2.2.

3.3 Results and Discussion

3.3.1 Determining the In-plane Elastic Moduli of BTTT Oligomers

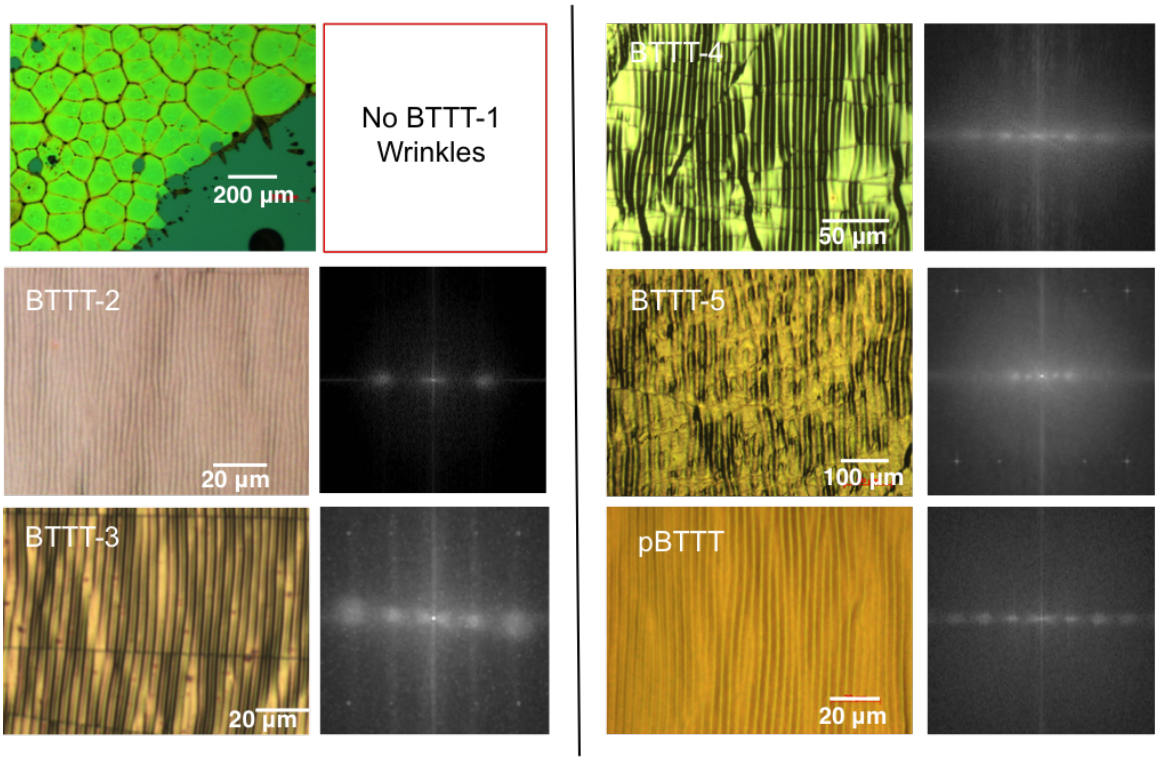

Figure 3.3: BTTT wrinkles and corresponding FFT spectra.

With the exception BTTT-1, all films displayed surface wrinkling when compressed above a critical strain (see Figure 3.3). BTTT-1 films showed large domains that developed fractures upon compressive strain application. BTTT-2, BTTT-3 and pBTTT films were smooth and produced highly periodic wrinkles. In contrast, BTTT-4 and BTTT-5 films were rough, likely due to inhomogeneous aggregations of small crystallites. As shown in Figure 3.3, the irregularity of these films produced crack/creases and strain localizations upon compression. Notwithstanding these non-uniformities, periodic wrinkles were obtained as demonstrated by the FFT spectra in Figure 3.3.

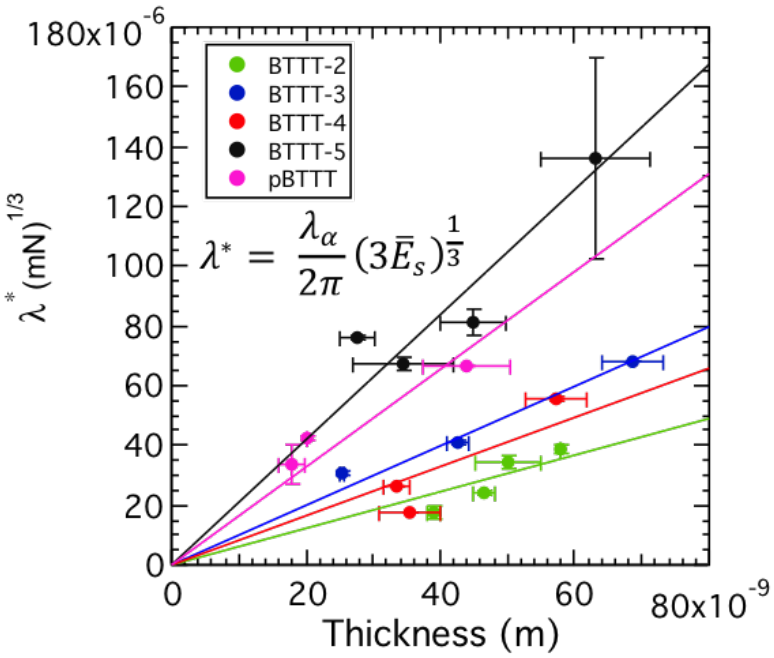

Figure 3.4: BTTT wrinkle wavelength as a function of film thickness.

Figure 3.4 demonstrates a linear dependence of wrinkling wavelength to film thickness. We utilize a scaled wrinkle wavelength $\lambda^* = \lambda_\alpha / 2\pi (3\overline{E}_s)^{1/3}$ as introduced in Section 2.3.1. Obtaining the linear fits for all materials, we can extract the plane-strain modulus of each film. A summary of our BTTT moduli results is shown in Table 3.1.

Table 3.1: BTTT in-plane elastic moduli

Material	**Molecular Weight [g/mol]**	$\overline{E}$ **[GPa]**
BTTT-2	1278	0.23±0.06
BTTT-3	1917	1.0±0.14
BTTT-4	2560	0.6±0.28
BTTT-5	3197	9.35±2.0
pBTTT	24000	4.55±1.30

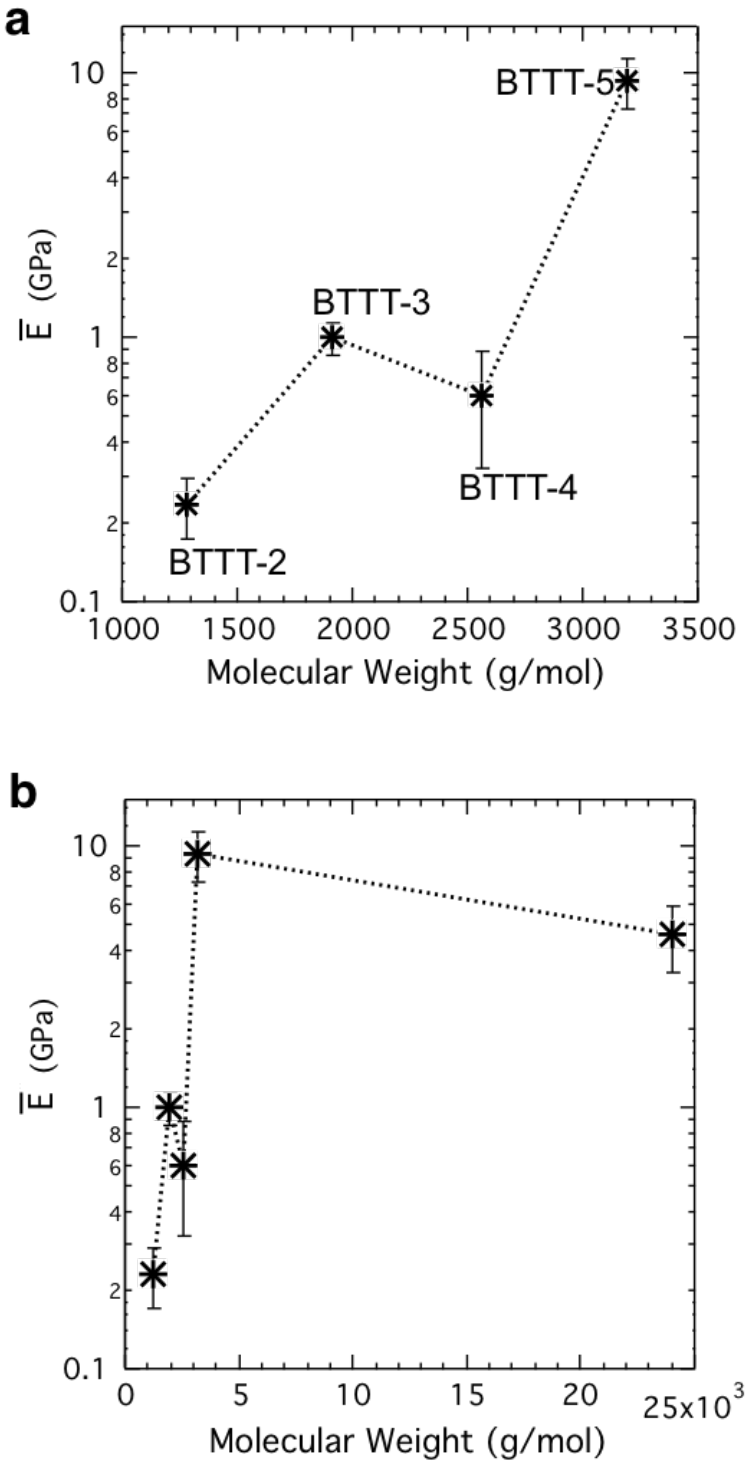

Figure 3.5: In-plane elastic moduli of a) BTTT oligomers and b) BTTT oligomers and polymer as a function of molecular weight.

Figure 3.5a and b show the elastic moduli of the oligomers and polymer as a function of molecular weight. The elastic modulus increases initially with increasing molecular weight, where BTTT- 2 displays the lowest value and BTTT-5 and pBTTT show the highest. The in-plane elastic modulus of pBTTT appears a slightly lower value than BTTT-5. This might indicate that a transition in mechanical behavior from small molecule to polymer occurs above 3500 g/mol. The degree of crystallinity of films is also an important factor dominating the mechanical behavior of polymer thin films. Published DSC data for the BTTT series, demonstrates that the crystallinity of the purified powder increases as a function of molecular weight [60]. This observation might not completely capture the crystalline properties of the films used in our experiments, since processing conditions can affect the degree of crystallinity of films. In addition to the degree of crystallinity, there are important morphological differences in the films of different molecular weight BTTT that will also affect mechanical measurements.

An independent analysis of the thin-film morphology and crystallinity by GIXD was published in a recent study by Zhang et al. [60]. We can use the key morphological features of each oligotiophene film outlined by Zhang et al. to interpret our elastic moduli data. Zhang et al. examined how the molecular weight affected the out-of-plane alignment of the crystalline domains. They discovered that crystalline domains become more aligned with the substrate with increasing molecular weight (Figure A.3). This can affect film modulus due to the anisotropic modulus of the oligomer crystallites, having the highest modulus along the molecular backbone (E_1) and the $\pi-$stacking direction (E_2) as explained by O'Connor et al. [32] (Figure 3.7). From this, we can expect to measure a higher in-plane modulus in materials with better alignment with respect to the substrate (E_1-E_2 plane coincides with the plane of compression in our experiments). It can also be expected that the modulus of the

film along the thickness axis (E_3) displays a more pronounced anisotropy in relation to the in-plane moduli as the molecular weight increases.

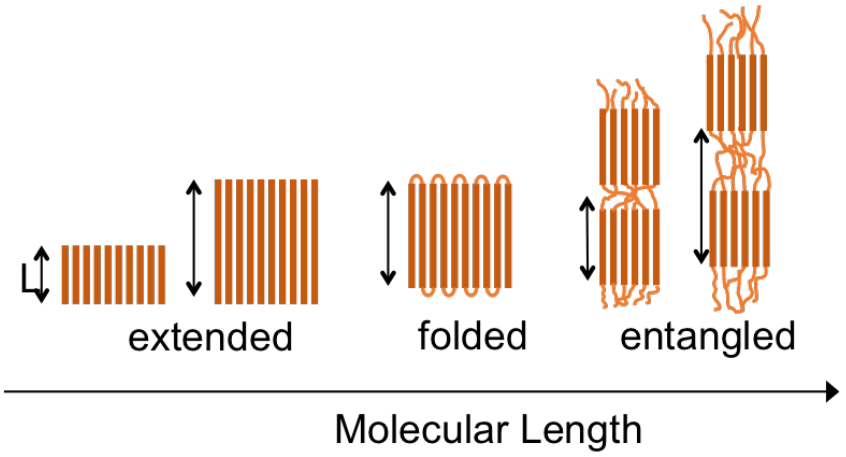

Figure 3.6: Crystal packing as a function of molecular weight.

In the GIXD data published by Zhang et al., BTTT-2 films show low ordering in comparison to BTTT-1 (Figure A.3). Crystalline grains show a wide distribution of angles with respect to the substrate. The d_{001} spacing was measured at 22 Å. The most important feature regarding the crystal packing of BTTT-2 comes from X-ray diffraction of single crystals grown from slow evaporation of hexane [60]. The crystal structure of BTTT-2 shows that in the a-b plane molecular sheets stack such that the backbones of the molecules is rotated approximately 48° relative the other neighboring sheets (see Figures A.1 and A.2). This, cross-stacking reduces the strong interactions from the $\pi-$stacking along the b-axis. We can speculate that the molecular sheet stacking pattern combined with relatively low degree of interdigitation of side alkyl chains and poor crystallite ordering with relation to the substrate might be responsible for low modulus measurement.

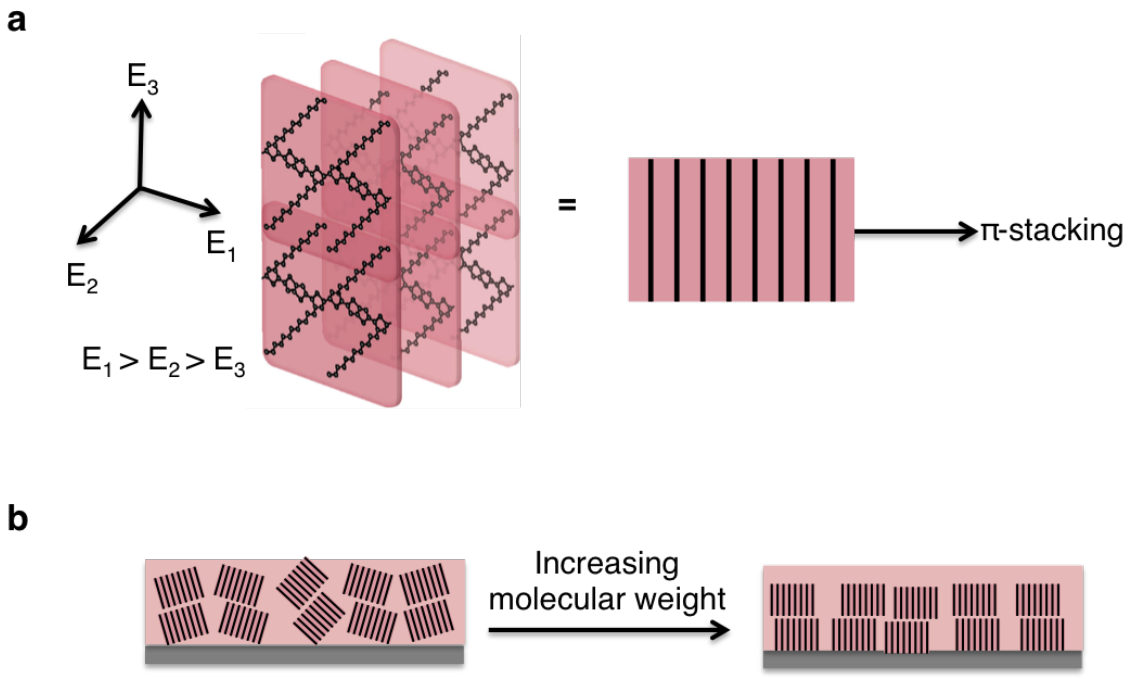

Figure 3.7: Effect of film microstructure on modulus measurements. a) Modulus anisotropy in BTTT crystal packing. Adapted and reprinted from Ref. [32]. Copyright (2010) American Chemical Society. b) Illustration of crystalline orientation as a function o molecular weight. Crystallites become more parallel to substrate with increasing molecular weight [60].

The modulus of BTTT-3 is 1 GPa, which is higher than that of BTTT-2. It was demonstrated the the d-spacing of BTTT-3 is approximately 18.6 Å, smaller than BTTT-2, which suggest a greater degree of alkyl chain interdigitation [60]. Compared to BTTT-3, BTTT-4 shows a larger lamellar stacking distance of 21 Å, indicating a lower degree of interdigitation. Zhang et al. attribute the larger d-spacing to the lower molecular symmetry of the alkyl side chains that BTTT-4 has in comparison to BTTT-3 [60]. BTTT-5 has a d[100] spacing of about 19.6 Å, indicating an enhancement in chain interdigitation [61]. Zhang et al. demonstrate that higher molecular weight oligomers order is nearly the same way on substrate as the polymer and share the same packing motif. Therefore, increasing the molecular weight beyond BTTT-5 does not significantly change the molecular packing. Nevertheless, we see a relative

decrease in the elastic modulus of pBTTT. This can be explained by the presence of chain entanglements.

3.3.2 Correlating BTTT Field-effect Mobility to Elastic Modulus

It has been previously observed that certain physical properties of polymers, such as degree of crystallinity, density and Young's modulus, increase initially as a function of molecular weight and eventually plateau [62]. Similar trends have been measured for electrical properties, such as the field-effect mobility of P3HT thin-film transistors [63, 64]. Therefore, we measure the mobility of BTTT oligomers and polymers to investigate whether any correlations exist between their mechanical and electrical properties as a function of molecular weight.

Top-gated, field effect transistors with CYTOP as dielectric layer (Figure 3.8b) were fabricated to characterize the field-effec mobility of BTTT series. Figure 3.8b shows the field-effect mobility BTTT oligomers and pBTTT. BTTT-2 displays the lowest mobility values, which can be explained by the cross-stacking pattern of the sheets in the crystal structure and the overall crystallite orientational disorder described by Zhang et al [60]. The mobility continues to increase with increasing molecular weight until BTTT-5. Both BTTT-4 and BTTT-5 exhibit very similar field-effect mobility values, almost two orders of magnitude higher than the one measured for BTTT-2. The rate of increase in mobility is significantly reduced between BTTT-5 and the polymer. This observation correlates to the difference in modulus between BTTT-5 and pBTTT. As in the case of modulus, we expect that there must exist a molecular weight value above which the field-effect mobility does not significantly change and the oligomer effectively behaves like a high molecular the polymer [63, 64].

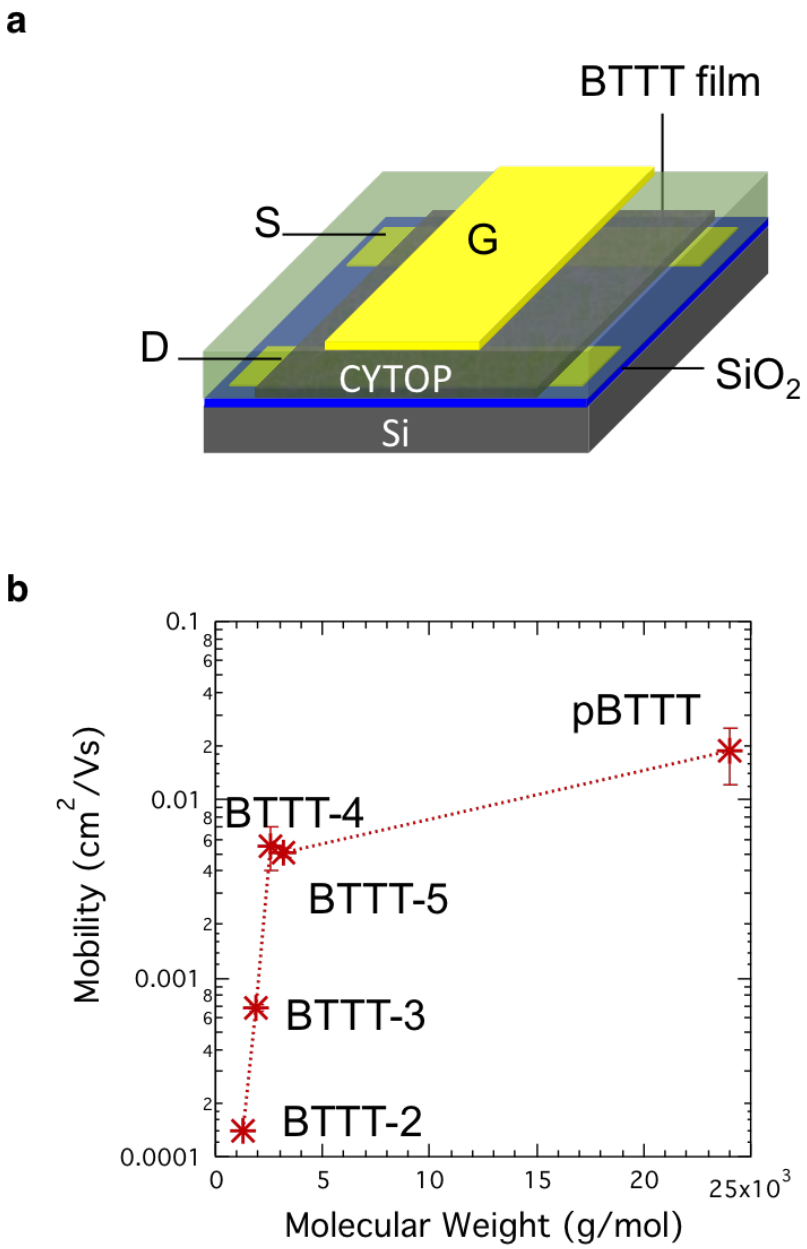

Figure 3.8: BTTT mobility measurements. a) BTTT field-effect transistor structure. b) BTTT field-effect mobilities as a function of molecular weight.

Figure 3.9 shows a comparison of the in-plane elastic modulus as a function of field-effect mobility. No clear trend is apparent, especially for the oligomers. This is an indication that there is no direct correlation between mechanical and electrical properties in the BTTT system. We note that the field-effect mobility is a measure-

ment based on surface conduction at the semiconductor/insulator interface. Mobility is highly dependent on film processing conditions, which can affect the degree of crystallinity and the density of defects. In contrast, in-plane modulus is a bulk property, where different molecular interactions beyond the surface are important.

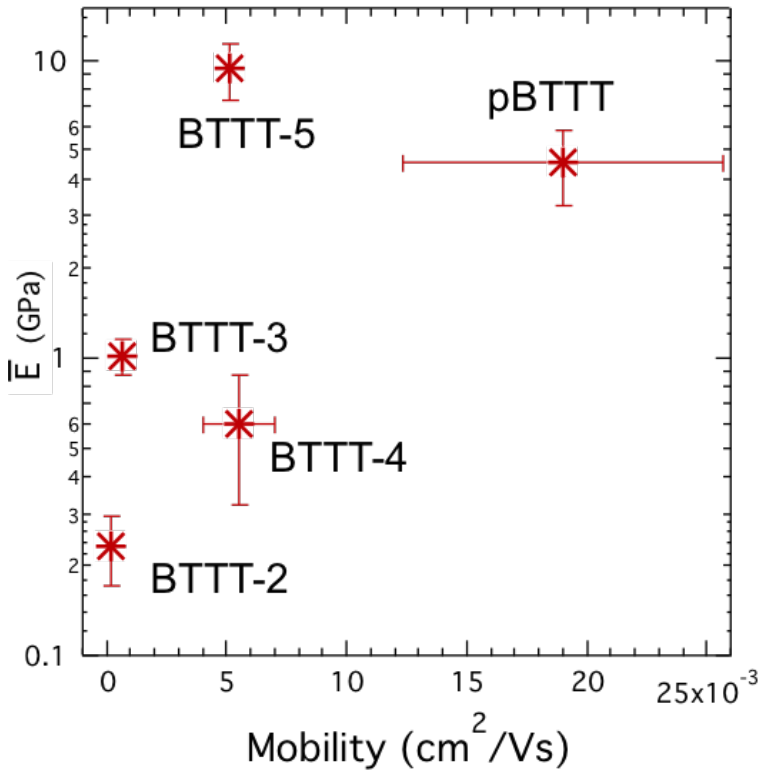

Figure 3.9: BTTT series in-plane elastic modulus as a function of field-effect mobilities.

3.4 Summary

Our experiments demonstrate that the mechanical and electrical properties of oligo- and poly-thiophene films are highly dependent on molecular weight. All BTTT oligomers, with the exception of the monomer (BTTT-1), were able to undergo the wrinkling instability. Our results show that, the plane-stress modulus of oligomers increases as a function of molecular weight. The increase is not monotonous, as a

small relative decrease in modulus is measured on BTTT-4 followed by an increase of an order of magnitude in BTTT-5. pBTTT does not significantly increase compared BTTT-5, which suggests that the modulus plateaus at some molecular weight values above 3500 g/mol. Although the degree of crystallinity of films is an important factor in defining the mechanical properties of thin films, we believe that the distribution and orientation of crystallites with respect to the substrate plays an important role.

3.5 Open Questions

DSC data is available for the purified powder form of BTTT oligomers, showing an almost monotonic increase in melting temperature as a function of molecular weight. Nevertheless, processing conditions (film casting method, solvent boiling point, annealing temperatures, etc.) can change the crystallinity of thin films. Therefore, it is important to understand how the degree of crystallinity of BTTT oligomers changes in films processed under similar conditions. This information will help decipher which parameter dominates the observed trend in mechanical properties, micro-structural differences or crystallinity.

3.6 Acknowledgements

We thank Dr. Lei Zhang, postdoctoral researcher in Briseno group, for synthesizing, characterizing and providing the BTTT oligomers. We also thank Dr. Jayanta Baral for fabricating and analyzing BTTT-4 transistor data.

CHAPTER 4

CHARGE TRANSPORT IN HOMOGENEOUSLY DEFORMED RUBRENE SINGLE CRYSTALS

4.1 Introduction

With the imminent proliferation of flexible and conformable organic electronic technologies, it has become essential to understand how mechanical deformation affects the electrical properties of organic thin-film devices. Due to their long-range order and purity, OSCs are the ideal system to study the effects of mechanical strain on charge transport properties without having to consider the independent effect of grain boundaries and other defects. Thus, by studying OSCs, we can correlate property changes to alterations in the crystal structure. The growth of thin, deformable, organic single crystals demonstrated in Chapter 2, introduces the possibility of utilizing OSCs in devices where the active layer undergoes mechanical strains during operation. Unfortunately, careful study of the effects of strain the electrical properties of OSCs has not been reported, likely due to experimental challenges such as crystal fragility and crystal delamination under compression.

Significant efforts into studying the effects of global bending on the field-effect mobility of organic polycrystalline films can be found in the literature. Sekitani el al. studied the effects of bending on the performance of pentacene field-effect transistors fabricated on flexible PEN substrates. [65, 66]. They showed that bending strains can affect field-effect mobility. Recently, Podzorov and coworkers demonstrated the mechanical robustness of thin, flexible OFETS of bis-(triisopropylsilylethynyl) pentacene (TIPS-pentacene) and bis-triethylsilylethynyl anthradithiophene (TES-ADT)

by bending them multiple times without degradation of performance. [67] Despite previous efforts utilizing polycrystalline films, the ideal platforms for a systematic study of strain effects on electrical properties are OSCs.

Due to the weak van der Waals bonds in molecular crystals, we expect global homogeneous deformation to affect crystal structure and therefore, affect molecular $\pi - \pi$ orbital overlap between molecules. This will be manifested in changes in the electrical properties of organic single crystals. Here, we investigate how mechanical deformation affects the electrical performance of ultra-thin (200 nm-1 μm) single crystals of the benchmark semiconductor rubrene when bent along the b [010] axis. We carefully control the strain field of the crystals by bending them around surfaces with known radii of curvature. Rubrene single crystals when subjected to bending tensile and compressive strains along the [010] crystallographic direction experience significant changes in sheet resistance. A piezoresistance coefficient of 11.26$\pm$0.47 is calculated from experimental values. We also addressed this issue from first-principles, by performing vdW-DFT calculations of mobility and resistivity as a function of applied strain. Computational results display a piezoresistive coefficient of 9.28, which is in very close agreement with experimental measurements.

Our experimental and computational results bring new understanding regarding what states of plane-strain might be detrimental or advantageous to OSCs device performance. This will impact future design of OSC devices for flexible electronic applications.

4.2 Experimental and Computational Approaches

Crystal growth: Thin rubrene single-crystals (200 nm - 1 μm) were grown using the process of horizontal physical vapor transport [15] from commercially available rubrene (99% Acros Organic™-Thermo Fisher Scientific,Inc). The as-received rubrene was purified three times through PVT before utilization as active material. The third

crystallization step followed the conditions outlined in Section 2.2 producing thin, flat crystal platelets.

Device fabrication: 120 μm thick PET slides with lateral dimensions of 2 cm x 4 cm, were used as substrates for bending experiments. Dow Corning Sylgard 184™prepolymer and cross-linking agent were mixed in a 5:1 mass ratio followed by dilution in hexanes in a 1:5 PDMS/hexanes mass ratio. The PDMS/hexanes solution was spin-coated at 3000 rpm for 45 seconds. The PET was secured to glass slides with polyimide tape prior to spin-coating. After spin-coating, PDMS was cross-linked at 70° C for two hours. The cross-linked PDMS (x-PDMS) thickness was approximately 1 μm. The x-PDMS serves as an adhesion enhancer between the PET and the crystal. 50 nm thick, parallel, Au contacts where thermally evaporated on x-PDMS through a shadow mask. Subsequently, the rubrene crystals were manually laminated with the long axis ([010]) direction perpendicular to the Au contacts (Figure 4.1a-b).

Bending experiments: Samples were bent along the high mobility axis of rubrene, b [010], using 3-D printed curved surfaces with known radii of curvature. Figure 4.1c, shows two schematics of the bending convention used through this study, positive radii correspond to tension and negative radii correspond to compression. PET samples were secure on the curved surfaces with adhesive tape (see Figure 4.1d). Strains were calculated using the expression: $\epsilon = t/2R$, where t is the thickness of the substrate and R is the radius of curvature. The radii of curvature used were: $\pm$ 40, 30, 20 and 10 mm; which correspond to the strains: $\pm$ 0.0015, 0.002, 0.003, 0.006, respectively.

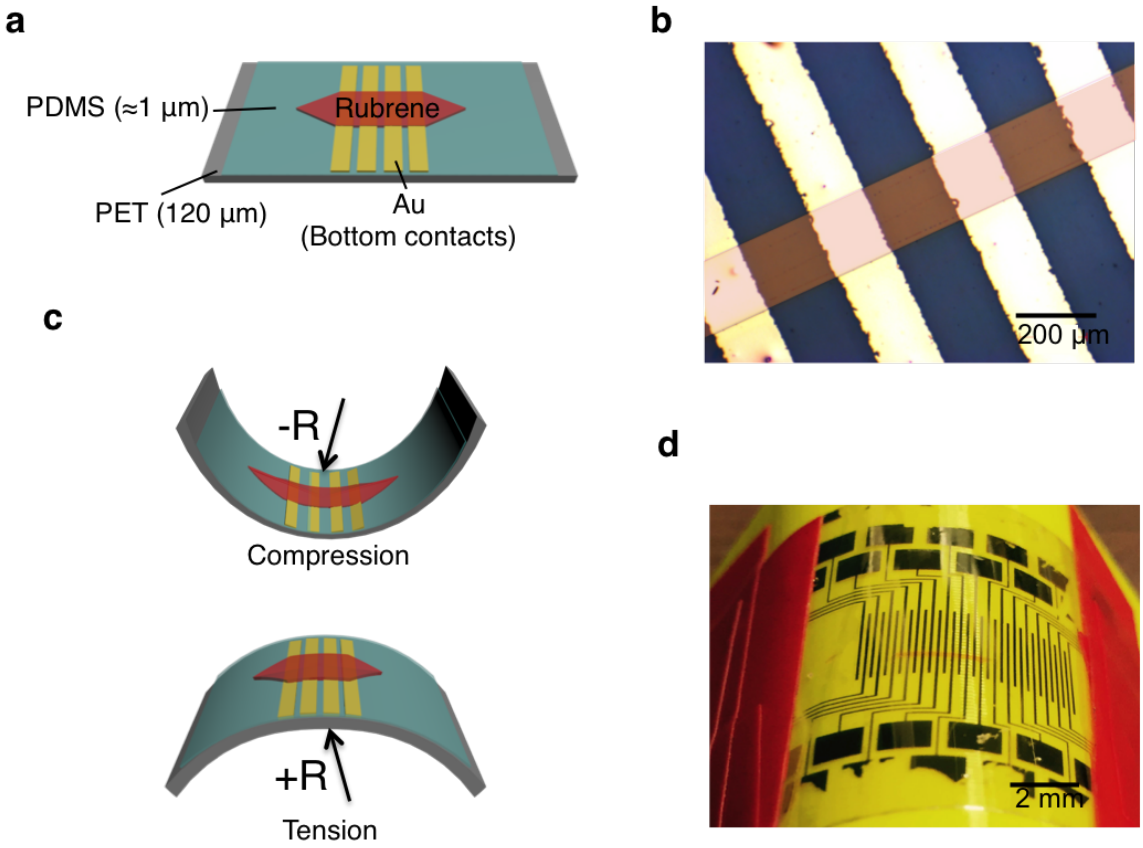

Figure 4.1: Single crystal bending platform. a) Schematic of rubrene device structure for bending experiments. b) Optical micrograph of rubrene single crystal laminated perpendicularly to the parallel Au contacts. c) Schematics of bending of rubrene single crystal device. d) Digital photograph of device structure attached to a surface with R = 10 mm.

Equipment and methods: Optical profilometry (Zygo NewView 7300) was used to confirm the local curvature of the crystals when attached to the curved surfaces, and to measure the thickness of x-PDMS film. Electrical surface resistance characterization was performed with a Keithley 4200-SCS connected to a Signatone H-150 micromanipulator probe station by sweeping voltages from -5 to 5 V and measuring the current. All I-V characteristics showed a linear dependence of the current on the voltage. Each resistance measurements was taken three times. For each specific applied strain, the strained resistances were measured in three independent strain

steps intercalated by unstrained resistance measurements. The average changes in resistance shown in Figure 4.4 were obtained from the average resistance measured at each strain step in relation to the average resistance of the unstrained sample.

Computational Methods: Prof. Ashwin Ramasubramaniam (UMass, Mechanical and Industrial Engineering) performed vdW-DFT calculations of the electronic structure of rubrene crystals that were strained along the high-mobility [010] axis. Assuming classical Drude-like transport of carriers within the relaxation-time approximation, the carrier mobility (μ) is given by

$$\mu_{e(h)} = \frac{e\tau}{m_{eff,e(h)}}, \tag{4.1}$$

where e is the elementary charge, τ is the carrier relaxation time, and $m_{eff,e(h)}$ is the effective mass of either the electron or the hole. The effective mass can be computed directly from the curvature of the electronic bands as $m_{eff,e(h)} = \hbar^2[\partial^2 E_{CB(VB)}(\mathbf{k})/\partial\mathbf{k}^2]^{-1}$ at either the valence band (VB) or conduction band (CB) edge; for our rubrene samples, which are hole-doped, the relevant effective masses are calculated at the VB edge. We assume that the dominant mode of carrier scattering is due to acoustic phonons and adopt a 2D deformation-potential model [68] whereby the relaxation time is given by

$$\tau = \frac{\hbar^3 Y L_{eff}}{\epsilon_{ac}^2 k_B T m_d}, \tag{4.2}$$

where Y is the elastic modulus along the carrier propagation direction, L_{eff} is the effective channel width for carrier transport, ϵ_{ac} is the acoustic deformation potential, T is the temperature, and $m_d = \sqrt{m_{eff,h1} m_{eff,h3}}$ is the so-called density-of-states mass, $m_{eff,h1}$ and $m_{eff,h3}$ being the hole masses along the [100] and [001] directions. Upon application of an external strain along the [010] direction, only the carrier

masses change via shifts in the electronic band structure. Thus, the relative mobility at uniaxial strain ϵ can be written rather simply as

$$\frac{\mu(\epsilon)}{\mu^0} = \frac{m^0_{eff,h} m^0_d}{m_{eff,h}(\epsilon) m_d(\epsilon)}, \tag{4.3}$$

and can be computed entirely from the carrier masses of the strained and unstrained (superscript "0") crystals. The resistivity is in turn related to the mobility as $\rho(\epsilon) = 1/ne\mu(\epsilon)$, n being the carrier density.

4.3 Results and Discussion

4.3.1 Piezoresistance Effect in Rubrene Single Crystals

Optical profilometry confirmed that the local curvature of crystal samples matched the macroscopic curvature of the surface almost perfectly. Small differences in radius arising from the substrate thickness were ignored and the nominal radii of curvature of the surfaces were used in the determination of strain. Figure 4.2 shows the local profiles of a representative crystal sample as it curves at different bending radii. Given that the device structure has a relatively soft interlayer between the PET and the rubrene single crystal, wrinkling might be possible when the sample is in compression. No wrinkles were observed for any of the bending conformations tested.

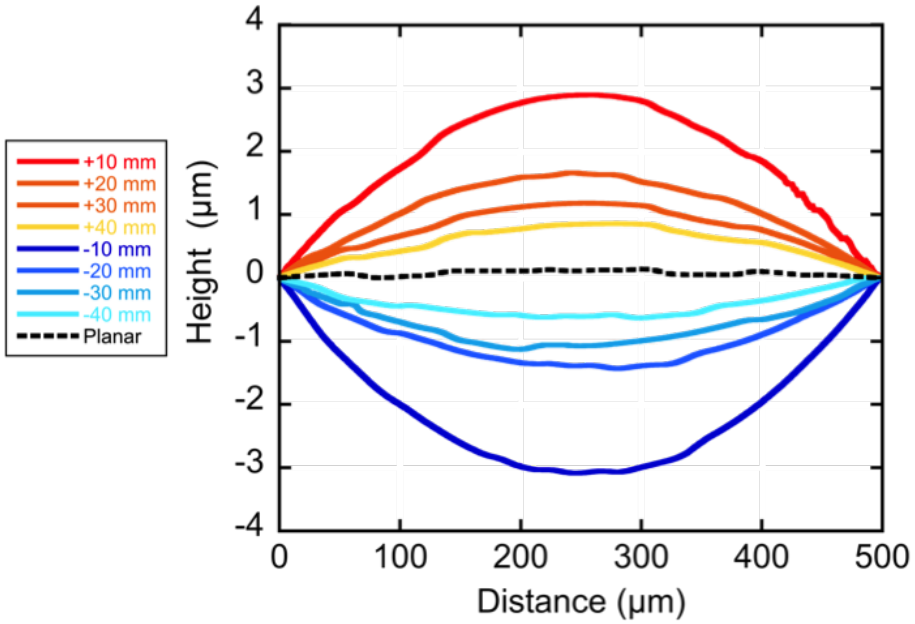

Figure 4.2: Representative profiles of local curvature corresponding to a rubrene single crystal device bent against surfaces with different radii of curvature.

Our results demonstrate that by deforming the crystals through bending, changes in resistance are observed in both tension and compression. Figure 4.3a shows that for positive strain, the resistivity increases with relation to the unstrained resistance, indicating a decrease in conductance. An increase in conductance, corresponding to a resistance decrease, is observed upon application of negative strains. The piezoresistance behavior was consistent over several cycles as shown in Figure 4.3. Despite the consistency, the magnitude of the change in resistivity exhibits small changes from cycle to cycle. Both the unstrained and strained resistances can show slightly different values over the range of two cycles.

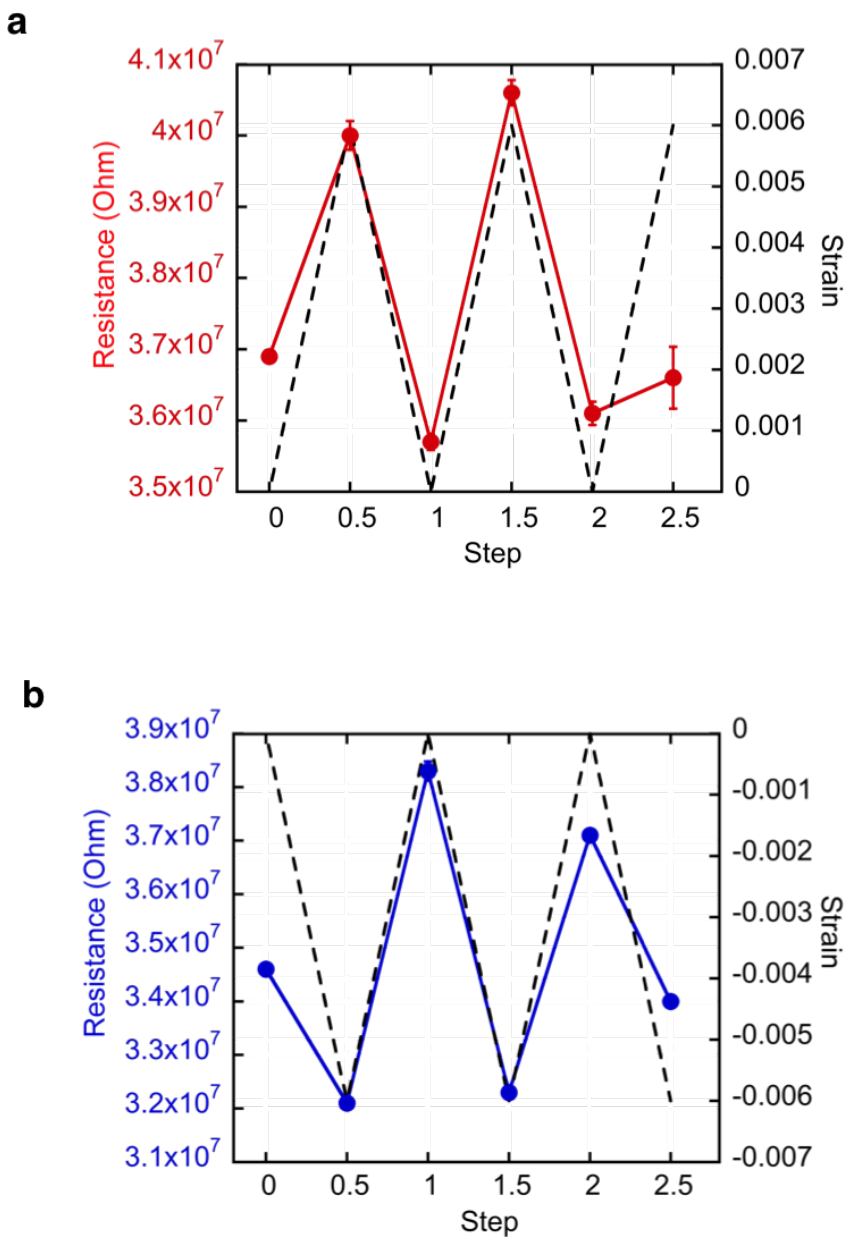

Figure 4.3: Cycling of piezoresistance performance for a) tensile and b) compressive strains.

The change in resistance with the application of strain is evidence of piezoresistance in rubrene single crystals. This can be explained by a change intermolecular distances under strain, which affects the π-orbital overlap between molecules. This is similar to observations by Rang et al. who studied the dependence of photoconduc-

tivity in tetracene, pentacene, and rubrene single crystals as a function of hydrostatic pressure. An increase in photoconductivity is observed and ascribed to the reduction of intermolecular distances due to pressure. [69, 70]. More recently, Takeya and coworkers have further studied the deformation of OSCs unit cells under hydrostatic pressure and the effects on the electronic properties of crystals [71, 72].

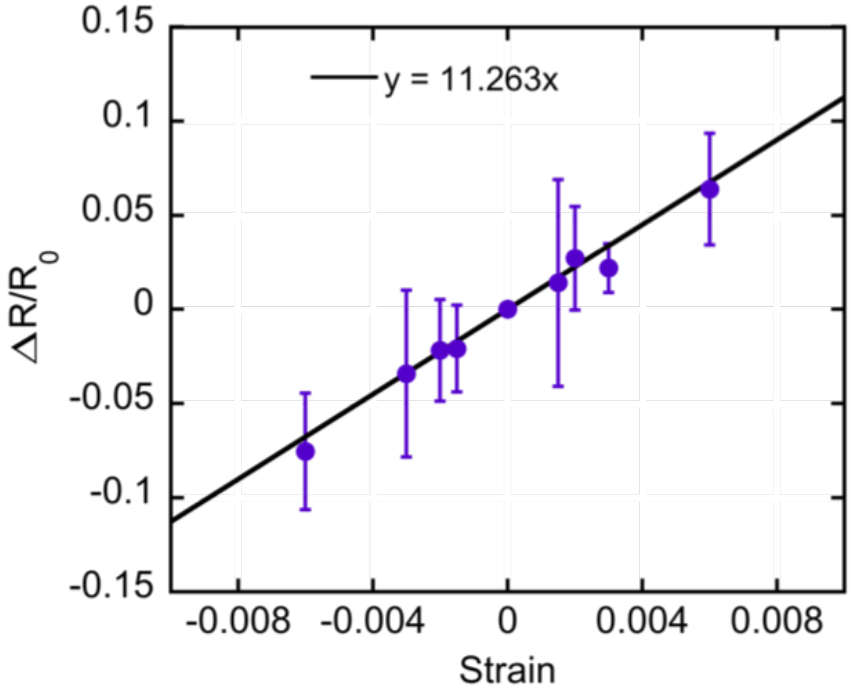

Figure 4.4: Average change in resistance as a function of bending strain.

Figure 4.4 shows an average change in resistance over all the measurements taken. The slope of the plot ($\Delta R/(\epsilon R_0)$) correspond to the piezoresistance coefficient or gauge factor as has a value of 11.26±0.47. The error bars are calculated from the variance in unstrained resistance and strained resistance over at least three bending cycles for each curvature.

4.3.2 Piezoresistance Effect Calculation in Rubrene Single Crystals

Prof. Ashwin Ramasubramaniam (UMass, Mechanical and Industrial Engineering) performed vdW-DFT calculations of the change of mobility and resistivity of rubrene based on charge-carrier masses. Assuming that the carrier density is not affected significantly by strain, the relative change in resistivity is given by $\Delta\rho/\rho \equiv [\rho(\epsilon) - \rho^0]/\rho^0 = [\mu^0/\mu(\epsilon)] - 1$. Figure 4.5 displays the relative change in resistivity for applied uniaxial strains along the b [010] axis ranging between $\pm 2\%$. As seen from this figure, the hole mobility can be enhanced by nearly 10% due to compressive strains of 1-2%, which may be attributed to increased $\pi - \pi$ overlap between rubrene molecules as they are brought closer to each other by the applied strain. The piezoresistive coefficient is 9.28, which is in close agreement with the experimental measurements based on resistance change.

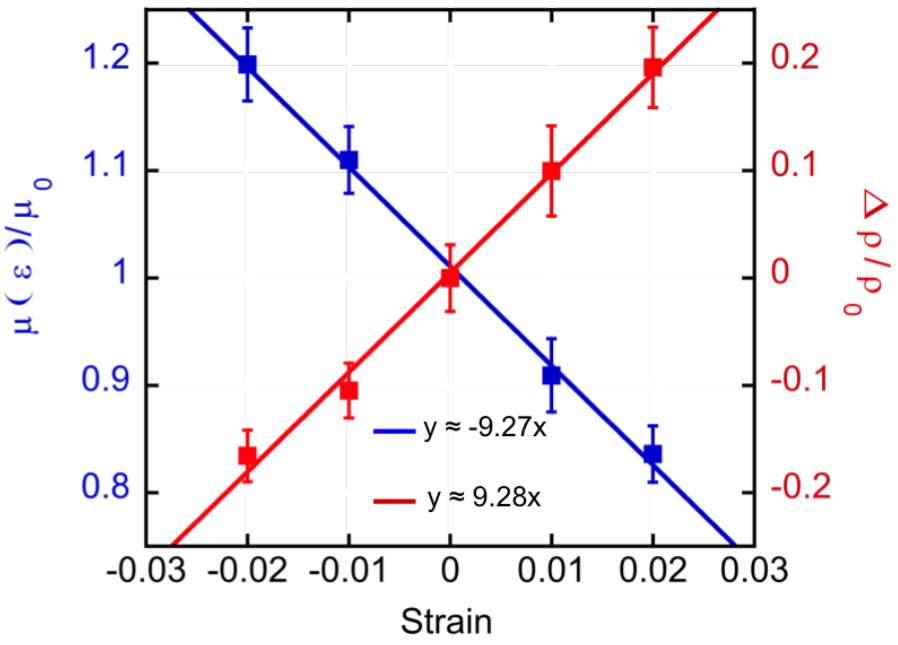

Figure 4.5: DFT results of change in resistivity and mobility as a function of applied strain.

4.4 Summary

The change in resistance with the application of strain is evidence of piezoresistance in rubrene single crystals. We demonstrate that the piezoresistance effect is reproducible. An increase in conductance is observed for compressive strains and a decrease is observed for tensile strains. This can be explained by a change intermolecular distances under strain, which affects the π-orbital overlap between molecules. Reducing the spacing between the rubrene molecules increases the π-orbital overlap while increasing the spacing, decreases the π-orbital overlap.

To our knowledge, this is the first study to measure the effects of uniform bending, both in tension and in compression, on the electrical properties of organic single crystal samples. The strain sensitivity demonstrated in this work will have an important impact in the application of organic semiconductors for strain sensors and electronic skin applications.

4.5 Open Questions

Going forward, this investigation will benefit from the addition a quantitive experimental investigation of the unit cell deformation in strained rubrene crystals.

Since the resistance of rubrene crystals is high, it would be interesting to investigate how the piezoresistance is affected in surface-doped crystals. A potential route for surface modification would be to use FTS-doping, as reported by Podzorov and coworkers [73].

Finally, due to the demonstrated mechanical and electrical anisotropy present in rubrene single crystals, we expect piezoresistance behavior to be different along different crystallographic directions. Therefore, orientation dependent piezoresistance experiments should be performed.

4.6 Acknowledgements

We thank Prof. Ashwin Ramasubramaniam (UMass, Mechanical and Industrial Engineering) for performing DFT calculations of mobility and resistivity and helpful conversations.

CHAPTER 5

CHARGE TRANSPORT IN INHOMOGENEOUSLY DEFORMED RUBRENE SINGLE CRYSTALS

5.1 Introduction

For the effective development of organic flexible electronic technologies, it has become essential to understand the how mechanical deformations affect electrical properties of organic semiconductors. In Chapter 4 we studied the effects of homogeneous bending in rubrene single crystals. We discovered the existence of a positive piezoresistive effect with a coefficient of approximately 11.26. To date, there has not been any research investigating the performance of single-crystal field-effect transistors (SCFETs) while undergoing inhomogeneous bending strains focused in the conducting channel region, located within the first few molecular layers above the dielectric/semiconductor interface [74]. This knowledge is crucial for the effective utilization of these materials in truly conformable electronics and other mechanically demanding applications such as pressure sensors and electronic skin [75, 76]. Therefore, it is important for the progress of the organic electronics field to understand how sensitive the performance of field-effect transistors is to the deformation of the conducting channel. We hypothesize that local inhomogeneous deformation collectively affect the performance of rubrene field-effect transistors.

In this chapter, we demonstrate that high field-effect mobility is maintained in rubrene single crystal transistors undergoing inhomogeneous strain conditions. We take advantage of the wrinkling instability of thin films on soft substrates as a unique way to strain the conducting channel of field-effect transistors in a non-destructive,

reversible, and predictable manner. Changes in field-effect mobility, both increases and decreases, are observed upon wrinkling. We discovered that this change in performance is dictated by the net strain at the dielectric/semiconductor interface. We propose an analytical model based on plate bending theory to quantify the net strain in wrinkled transistors and predict the change in mobility. The present study is, to our knowledge, the first report demonstrating the wrinkling of high-performance organic single crystal field effect transistors and the impact of local bending of the conducting channel in charge transport characteristics. These contributions represent a significant step forward in structure-function relationships in organic semiconductors, critical for the development of the next generation of flexible electronic technologies.

5.2 Experimental Approach

Crystal Growth: Thin rubrene single-crystals (200 nm - 1 μm) were grown using the process of horizontal physical vapor transport [15] from commercially available rubrene (99% Acros Organic™-Thermo Fisher Scientific,Inc). The as-received rubrene was purified three times through PVT before utilization as active material in transistors. The third crystallization step followed the conditions outlined in section 2.2 to obtain very thin, flat crystal platelets.

Transistor fabrication and characterization: First, rubrene single crystals were manually laminated on a poly(acrylic acid) (PAA)-coated silicon wafer. PAA is a water-soluble polymer that functions as a sacrificial layer for lift-off and transfer from silicon wafer to x-PDMS substrate. Next, parylene-N films (Specialty Coating Systems™) ranging from 400 nm - 1.3 μm in thickness were deposited on the crystals (Figure 5.1 (1)). Parylene serves as gate-dielectric material in the transistor structure. Parylene is used as the insulating layer due to the demonstrated low density of traps at the dielectric/crystal interface. [10, 39, 77, 78] Parylene films are transparent, pinhole free, and possess exceptional mechanical (Young‘s modulus = 2.4 GPa, yield strength

= 42 MPa), [79] and dielectric properties (ϵ = 2.65, breakdown electric field of 10 MV/cm for 100 nm thick films). [14] Subsequently, a 40 nm gold layer was thermally evaporated on the surface of the parylene film to act as the gate electrode (Figure 5.1 (1)). The Au/parylene/crystal configuration was then stamped on the surface of a cylindrical x-PDMS (Dow Corning Sylgard 184™) substrate with a small flake of highly oriented pyrolytic graphite (HOPG) between the x-PDMS/Au interface to create contact with a small section of the bottom gate, facilitating probe connection during electrical measurements (Figure 5.1 (2)).

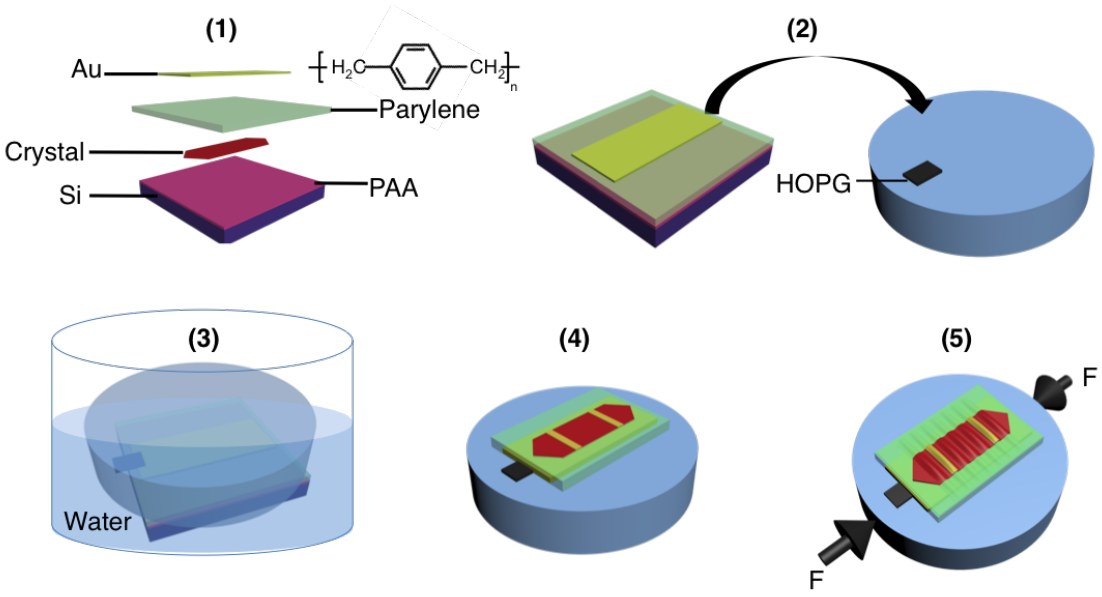

Figure 5.1: Single crystal transistor on elastomeric substrate fabrication steps. (1) Rubrene crystal is laminated on Poly(acrylic acid) (PAA) coated Si wafer. Parylene is vapor-deposited on crystal and then gold gate is thermally evaporated. (2) The complete SCFET assembly is laminated on elastomer substrate with gate electrode facing the bottom. An HOPG flake is used to facilitate contact with the gate electrode. (3) The elastomer/SCFET is partially submerged in water to dissolve PAA layer and expose the top facet of crystal. (4) Top source and drain Au contacts are evaporated using a shadow mask. (5) The completed SCFET on elastomeric substrate is able to wrinkle.

The PAA was easily dissolved by submerging the device assembly in water (Figure 5.1 (3)). After transfer of Au/parylene/crystal structure to x-PDMS surface, all samples were rinsed in DI-water to eliminate any PAA residue. Samples were dried in a chamber with constant flow of dry air overnight. Au source and drain electrodes are thermally deposited on the exposed (100) facet of the rubrene crystal (Figure 5.1 (4)). For this study, we utilized a top-contact geometry to ensure intimate metal/semiconductor interface while applying mechanical strains. Notice also that the fabrication process places all electrodes and dielectric directly on the surface of the crystal. This minimizes interfacial defects that come from lamination and coating of active layers on prefabricated substrates.

Wrinkling by mechanical compression: Two Thorlabs one-dimensional translation stages were utilized to build a strain stage. The x-PDMS cylinder with the crystal attached to its top is placed between the two translating blocks for compression (see Section 2.2)

Topographic analysis: A function of length and width is interpolated through all the surface points obtained through optical profilometry (Figure 5.2). The interpolated function represents the out-of-plane displacement from which local strains can be derived. Using an interpolated function facilitates the manipulation of topographic data during the local strain calculations.

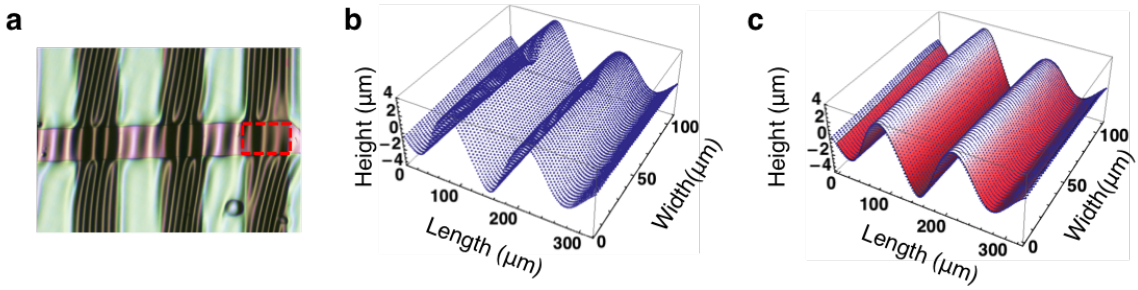

Figure 5.2: Topographic data analysis. a) Optical micrograph of wrinkled single crystal FET. Surface features of wrinkled transistors are measured using optical profilometry. b) 3D plot of x, y, z data obtained from optical profilometry. This data corresponds to dotted area in (a). c) A function of length and width is interpolated through all the surface points.

Equipment and settings: Crystal thickness and topographic data of wrinkled samples was obtained by optical profilometry (Zygo NewView 7300). Parylene thickness was measured by spectral reflectance (Filmetrics F20). Optical micrographs were obtained with a Zeiss Axioscope A1 equipped with Zeiss AxioCam ICc1 camera. Transistor characteristics were measured at room temperature in air on a Keithley 4200 SCS and Signatone Micromanipulator H-150 probe station.

5.3 Results and Discussion

5.3.1 Rubrene Crystal Field-Effect Mobility Modulation via Conducting Channel Wrinkling

The use of a cylindrical elastomeric substrate allows the precise alignment of the direction of applied strain by rotation. This study focused on the effects of wrinkling along the direction of high mobility in rubrene ([010]), also referred to as the b-axis [17, 48] (see Figure 5.3).

Applying in-plane, uniaxial, global compressive strains (ϵ_{xx}^{global}) above a critical value, generates one-dimensional wrinkling across the conducting channel of the

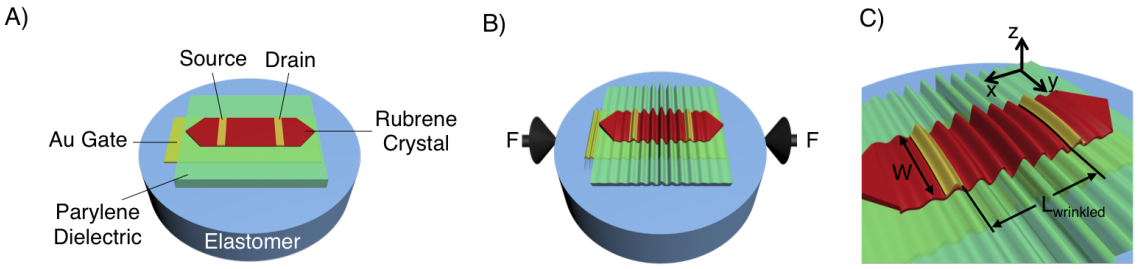

Figure 5.3: Rubrene single crystal transistor on elastomeric substrate. a) Structure of rubrene single crystal transistor. The crystal is embedded in parylene dielectric only exposing one crystal facet. b) The transistor wrinkles at a critical global compressive strain. The present study utilizes uniaxial compression along the high-mobility axis [010] of rubrene crystals. c) Coordinate system. The plane of the transistor corresponds to the x-y plane, which is perpendicular to to z-axis.

SCFET. ϵ_{xx}^{global} is defined by the change in diameter (D_{cyl}) of the x-PDMS substrate in the direction of compression as $\epsilon_{xx}^{global} = \triangle D_{cyl}/D_{cyl,0}$. Figure 5.5a, shows optical micrographs of a rubrene single crystal device in its planar and wrinkled configurations. For small ϵ_{xx}^{global}, ($\epsilon_{xx}^{global} \leq 0.01$ for devices in this study), wrinkling is reversible such that when the compression is removed, wrinkles disappear. At large ϵ_{xx}^{global} values, delamination of SCFET from x-PDMS substrate occurs (see Figure 5.4).

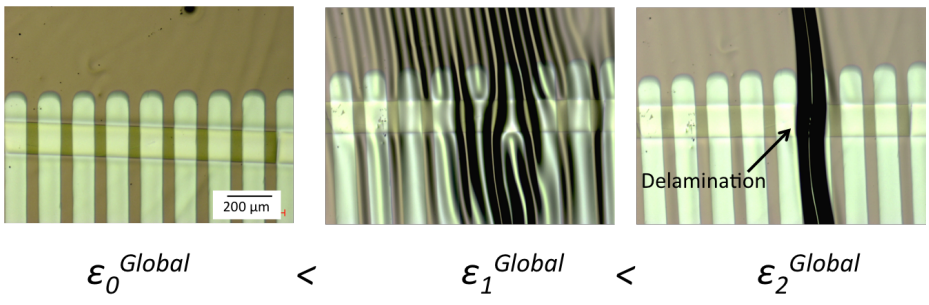

Figure 5.4: Delamination of wrinkled SCFET.

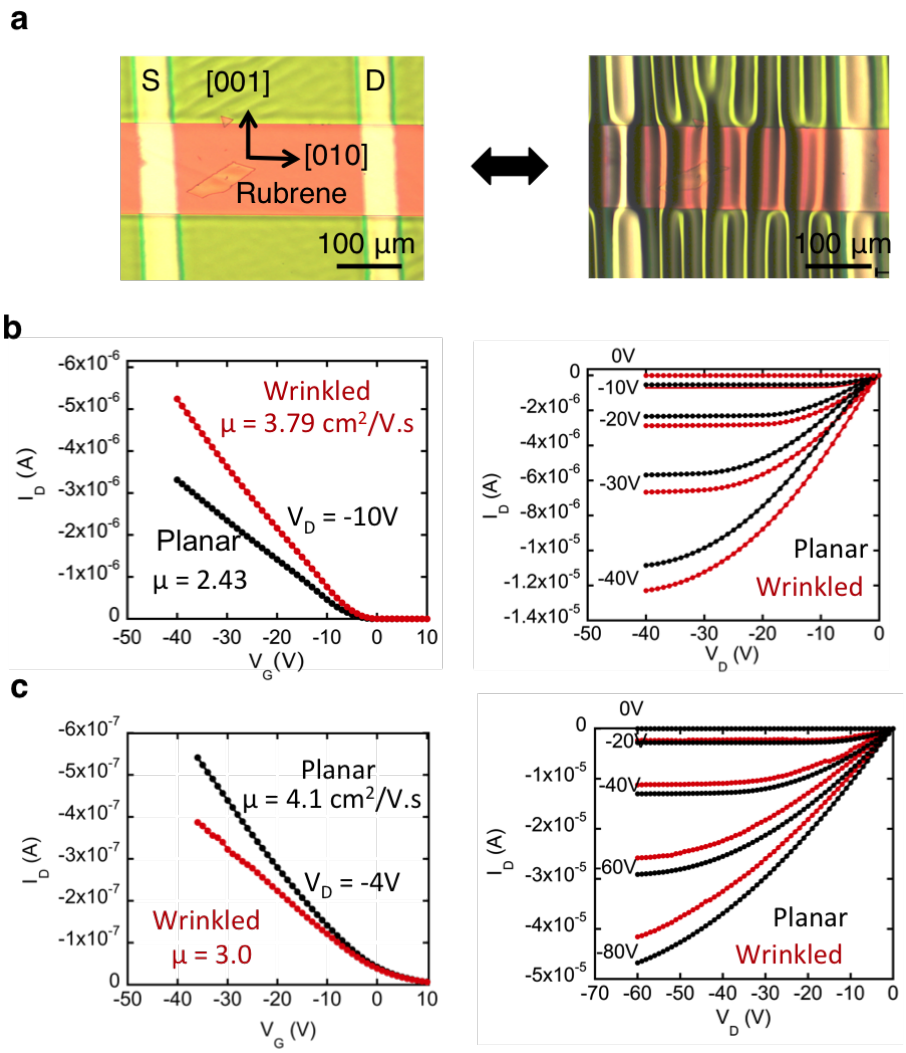

Figure 5.5: Electrical characteristics of single crystal transistor on elastomeric substrate in planar and wrinkled configuration. a) Optical micrograph of SCFET in planar and wrinkled configurations. b) Representative transfer and output characteristics for device showing an increase in field-effect mobility. c) Representative transfer and output characteristics for device showing a decrease in field-effect mobility.

To ensure a homogeneous charge-carrier density across the conducting channel all FETs were operated in the linear regime with drain voltages V_D ranging from -5 V to -15 V. All field-effect mobilities reported in this study were extracted using the expression [25]:

$$\mu = \frac{L}{WC_iV_D}\left(\frac{dI_D}{dV_G}\right) \tag{5.1}$$

where C_i is the capacitance per unit area of the insulating layer, V_G is the gate voltage, V_T is the threshold voltage and μ is the field-effect carrier mobility. All of the transistors fabricated for this study exhibit excellent characteristics, with mobilities as high as 8 cm^2/Vs, I_{on}/I_{off} of 10^6 and threshold voltages close to 0 V. Typical device output and transfer characteristics for planar and wrinkled devices are shown in Figure 5.5.

Considerations are taken to ensure that the charge carrier mobilities measured while straining SCFETs are not contact-resistance-limited. It is known that channel length affects the total device resistance in two-probe measurements [80, 81]. To determine how mobility is affected by channel length, multiple parallel gold contacts were deposited through a shadow mask on the single crystals, allowing for multiple field-effect mobility measurements on the same crystal sample as a function of channel length. Figure 5.6a shows a micrograph of a representative rubrene SCFET with multiple contacts. Devices were measured by using one contact as the common source electrode and the remaining contacts as drains, one at a time, systematically increasing the channel length. We observed that, for the same crystal, field-effect mobility increases with increasing channel length, with negligible change observed above length of approximately 500 μm, after which the changes are not as pronounced. This trend can be explained by considering the total resistance, $R_T = R_C + R_{Ch}$, as a function of the contact resistance R_C and the channel resistance R_{Ch}. R_{Ch} changes with channel dimensions according to $R_{Ch} = \rho\,(L/W.t)$, [82] and gate voltage V_G. Therefore, for the same V_G, mobility changes with channel dimensions because the relative magnitude of R_{Ch} increases and the influence of R_C is reduced as channel length increases. The intrinsic channel mobility dominates transport at large channel lengths while contact resistance limits it at short lengths. The 500 μm channel length is not a general rule for non-contact limited mobility, a more accurate indicator is the

channel aspect ratio (L/W). All the mobilities measured in our study plateau at an L/W value of approximately 2.5 (see Figure 5.6d).

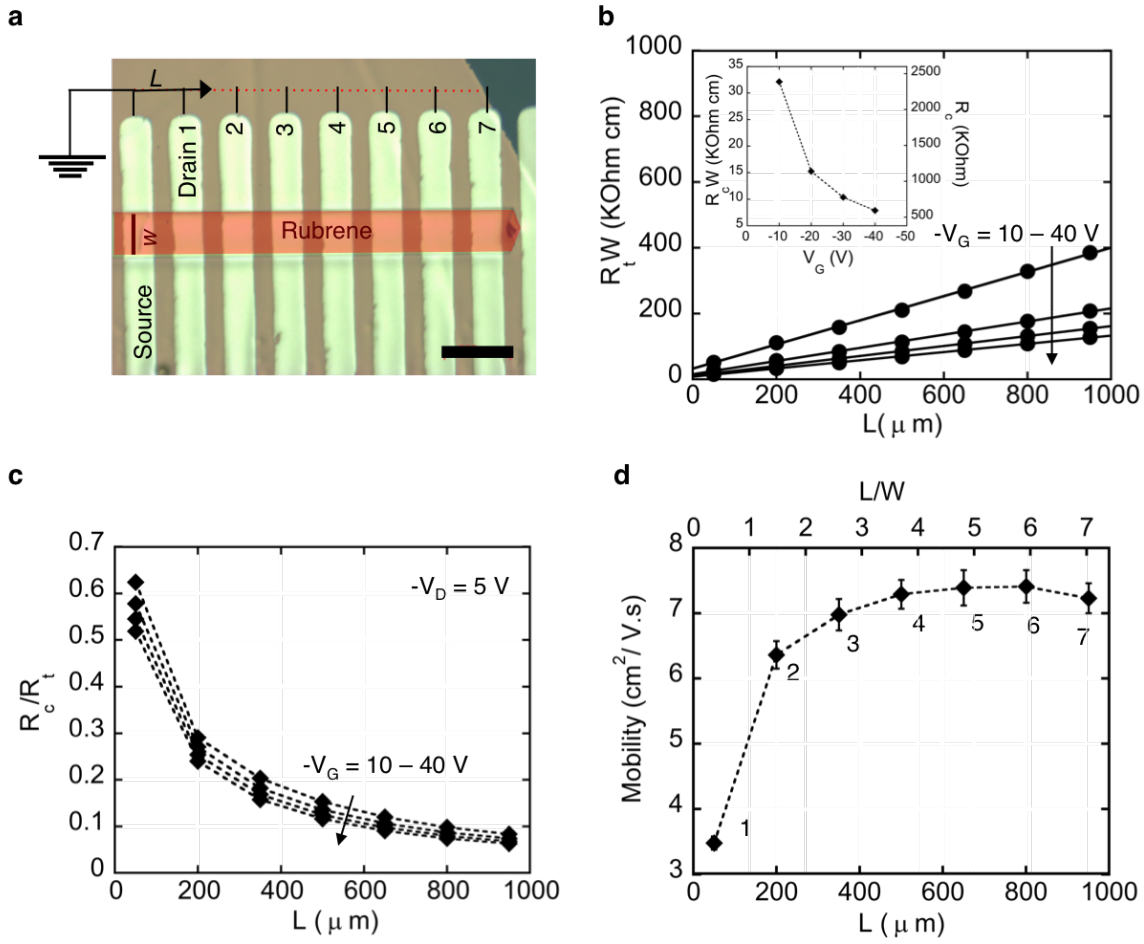

Figure 5.6: Contact resistance determination. a) Optical micrograph of representative single crystal FET with multiple top contact source and drain electrodes allowing for multiple channel length testing on same crystal sample. The crystal is colorized for clarity. For additional device details, see Appendix B. b) Width-normalize total device resistances as a function of channel length for different gate voltages. The contact resistance as a function of gate voltage is shown in the inset. c) Fraction of total device resistance due to contact as a function of channel length for different gate voltages. d) Field-effect mobility trend as a function of channel length and channel aspect ratio (L/W) for the device in (a). Mobility changes are negligible above a channel length of approximately 500 μm. Error bars in mobility correspond to the standard error of the mean from six independent measurements at different drain voltages in the linear regime, -5 V to -15 V at -2 V steps.

Contact resistances were determined using the gated transmission-line method (TLM) as reported elsewhere [81,83]. The width-normalized total resistances ($R_T W$) as a function of channel length is shown in Figure 5.6b. Figure 5.6c shows the fraction of the total device resistances due to contact resistances (R_c/R_T). We observe that at channel lengths larger than 500 μm the contact resistances correspond to less than 20% of the total resistance measured. In Figure 5.6d, the trend of mobility as a function of channel aspect ratio is shown for the same crystal sample shown in Figure 5.6a. Only devices with negligible dependence of mobility on channel length were utilized for wrinkling experiments.

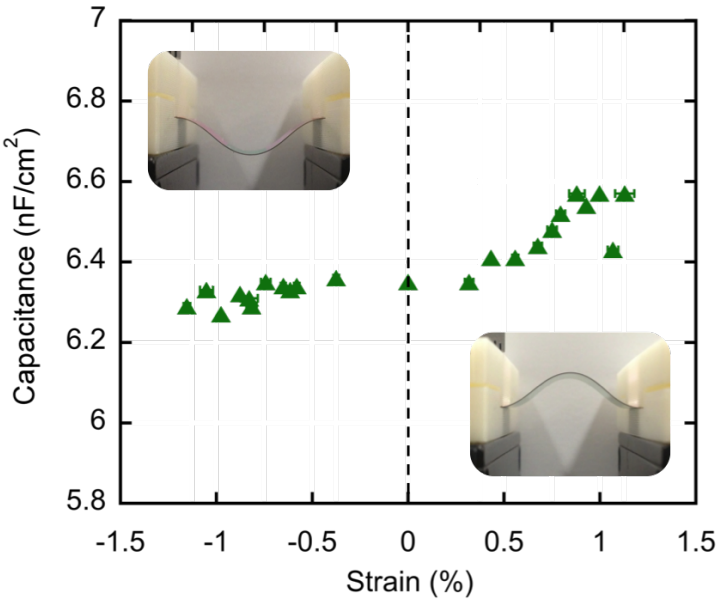

Figure 5.7: Global buckling of parylene capacitor. Parylene capacitance change measured as a function of global bending of parallel plate capacitor. Strain calculated from different bending radii.

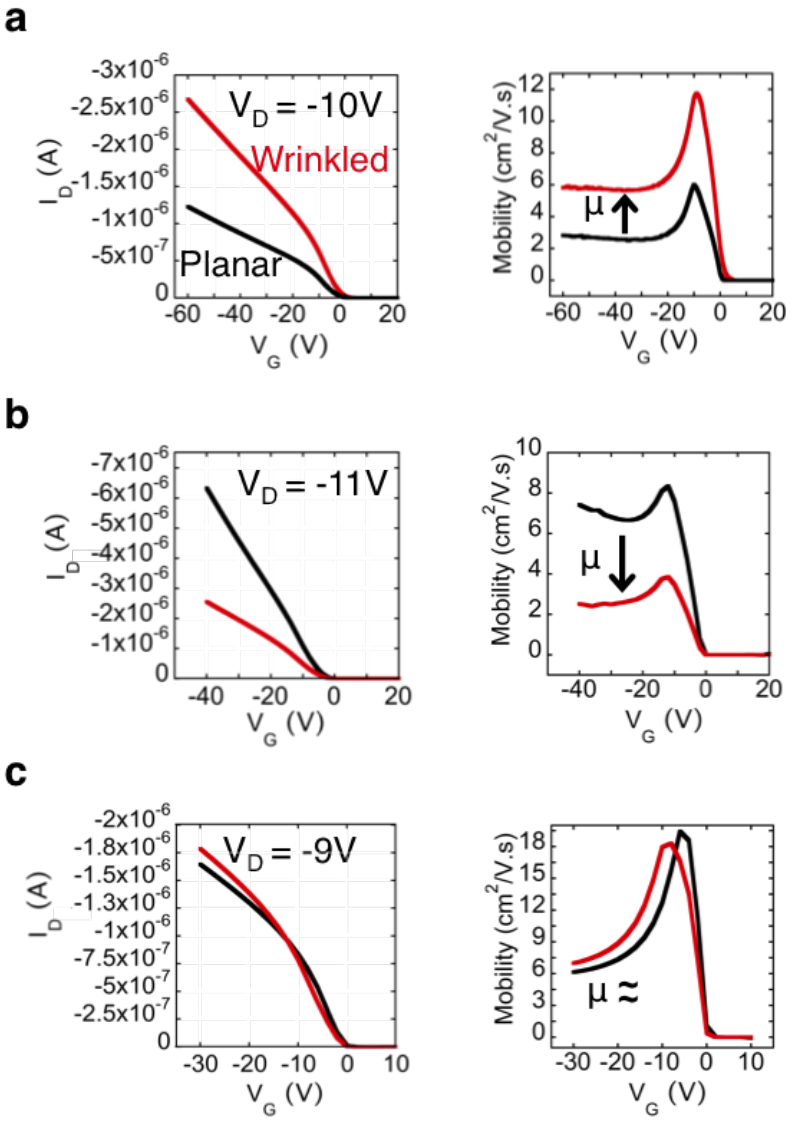

Figure 5.8: Effects of wrinkling single crystal field-effect transistors on mobility. a-c) Drain current I_D vs. gate voltage V_G corresponding to three different devices in their planar configuration and while undergoing wrinkling. Corresponding Mobility $\mu = [L/WC_iV_D]\,(dI_D/dV_G)$ vs. gate voltage V_G is shown.

Despite maintaining excellent transistor characteristics while undergoing wrinkling, impact in field-effect mobility is observed. Figure 5.8 shows comparative transfer characteristics between planar and wrinkled devices along with the corresponding plots of mobility, μ, as a function of gate voltage, V_G. Significant increase (Figure

5.8a), and decrease (Figure 5.8b) in mobility can be measured when SCFETs are wrinkled. Other devices show almost negligible change upon wrinkling (Figure 5.8c). As a control, we determined that the capacitance of parylene is effectively unchanged under applied strain (Figure 5.7); therefore, the same capacitance values are used to calculate the mobility of both planar and wrinkled devices.

It has been shown that that the coexistence of different d-spacings in an organic semiconductor can affect the mobility by inducing shallow trap states. Examples of this effect can be seen in pentacene OFETs [84] and in devices prepared using vibration-assisted crystallization introduced by Diemer et al. [85]. The strain in a wrinkled SCFET is inhomogeneous, therefore, an array of different crystal interplanar distances must be present in the conducting channel. To test the impact of this phenomenon, we estimated the trap density, N_{it}, for the devices shown in Figure 5.8 using the expression: $N_{it} = \frac{C_i}{q^2}\left(\frac{Sq}{k_B T ln(10)^{-1}}\right)$ [86]. Where C_i is the capacitance of the insulator, q is the elementary charge, $S = \frac{dV_G}{d(logI_D)}$ is the subthreshold slope, k_B is the Boltzmann constant and T is the temperature. Small differences in trap state densities are observed between the planar and wrinkled configurations of all devices (Figure 5.9), including a reduction in the trap density for the case of mobility decrease shown in Figure 5.8b. No correlation is apparent between the increase/decrease of the density of interfacial trap states and mobility, which indicates that this effect is not dominant in the change in mobility observed upon wrinkling.

To understand the effects of wrinkling on mobility, we hypothesize that the different behaviors observed depend on the net strain in the [010] direction (x-axis) experienced by the conducting channel while wrinkling. A model to quantify the net strain at the crystal/semiconductor interface is proposed next.

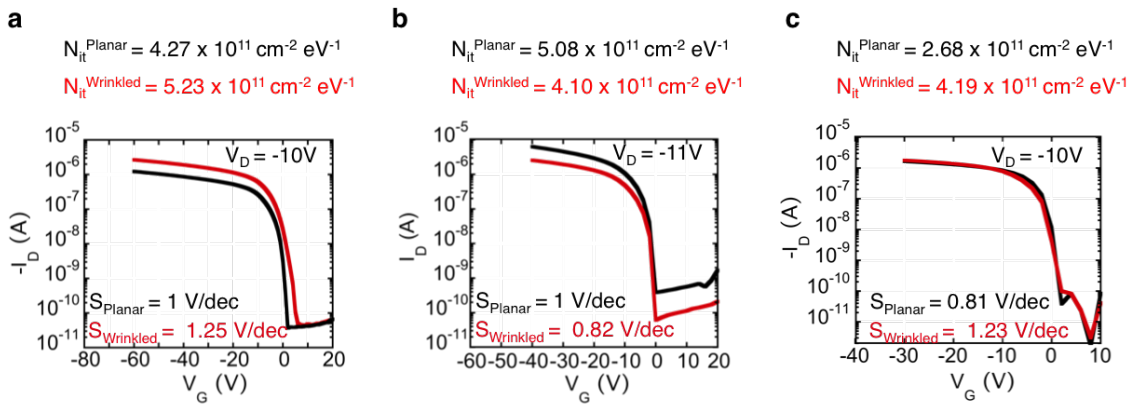

Figure 5.9: Interfacial traps calculation for devices shown in Figure 5.8.

5.3.2 Net strain Analysis in Wrinkled Rubrene Single-Crystal Transistors

SCFETs are multilayered structures composed of different materials spanning a large range of thicknesses and mechanical properties. Figure 5.10a shows a cross-sectional schematic of the device indicating the positions of each layer, the position of the conducting channel, z_{con}, and the representative position of the neutral plane, z_{np}, which is the plane that remains unchanged in length upon bending. Ignoring shear stresses at the x-PDMS/SCFET interface, we can consider the wrinkled SCFETs as composite plates that are undergoing bending with continuously changing curvature (Figures 5.10b, 5.10c). Continuous changes in concavity in the wrinkled channel, translate into continuous local change between mechanical tension and compression. The local strain of a wrinkled plate is written as a combination of the contributions of the von Kármán nonlinear plate model [87] and the local bending [88, 89]:

$$\epsilon_{xx}^{local}(x,y,z) = \epsilon_0 + \frac{\partial u(x,y)}{\partial x} + \frac{1}{2}\left[\frac{\partial w(x,y)}{\partial x}\right]^2 - \frac{\partial^2 w(x,y)}{\partial x^2} z; \tag{5.2}$$

where ϵ_0 is the critical strain for buckling, u is the in-plane displacement in the x direction, w is the out-of-plane deflection and z is the vertical coordinate through the thickness of the SCFET. In our experiments, the direction of wrinkling corresponds

to the x-axis (Figure 5.3c). For a wrinkled plate with small out-of-plane deflections, the in-plane displacement gradient is negligible. In our device structure, z represents the position of the conducting channel with respect to the neutral plane. Assuming that the charge carrier conduction is restricted to the dielectric/crystal interface in all devices, both in their planar and wrinkled configurations, makes z constant: $z = z_{con} - z_{NP}$. For the pure bending of a freestanding, multilayered film, the neutral plane location is determined by:

$$z_{np} = \frac{\sum_i z_i \overline{E}_i t_i}{\sum_i \overline{E}_i t_i}. \tag{5.3}$$

where z_i is the distance of centroid of the i-th layer, E_i and t_i are the Young's modulus and thickness of the corresponding layer, respectively.

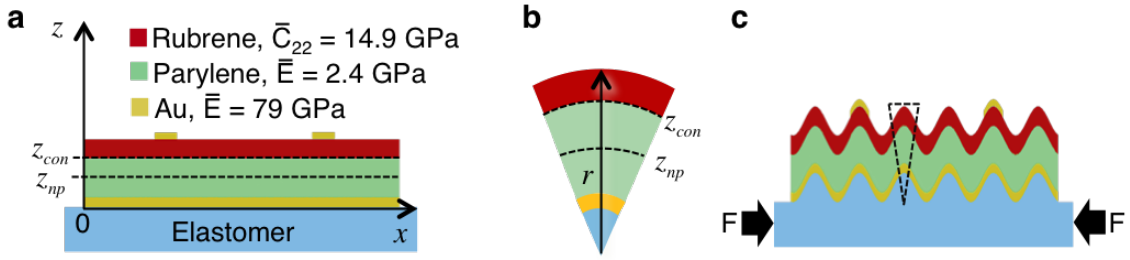

Figure 5.10: Net channel strain analysis. a) Cross-sectional schematic of single crystal transistor structure. Charge transport in field-effect transistors occurs at the dielectric/semiconductor interface (conducting channel, z_{con}). The position of neutral plane (z_{NP}) can be manipulated by changing the thicknesses of the different layers in the device. b) The local channel strain, ϵ_{xx}^{local}, depends on the position of z_{con} with respect to z_{NP} and local out-of-plane defection. c) Wrinkled transistors can be treated as a bending composite plate with continuously changing curvature.

Equation 5.2 is based on the curvature of the neutral plane, which is not known from the raw topographic data. Consequently, for an accurate determination of the strain in the conducting channel, a correction of the last term in Equation 5.2 is required.

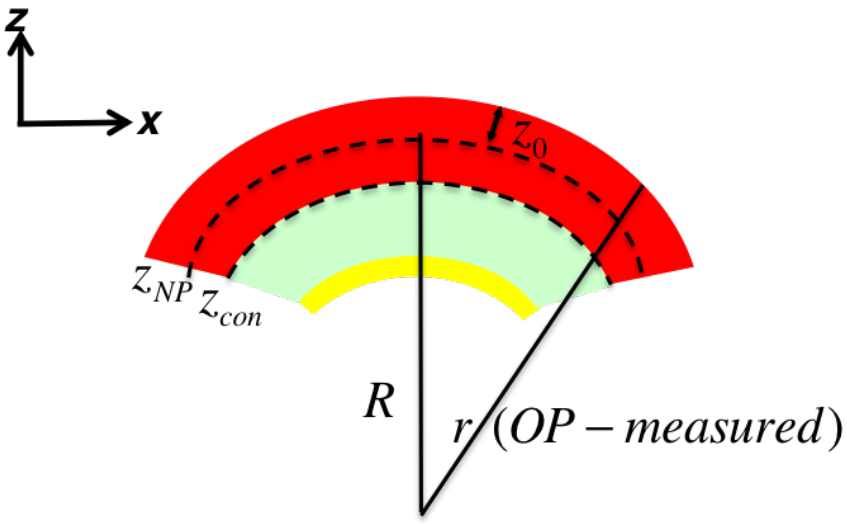

Figure 5.11: Bending of multilayered film.

Consider the bending of a multilayered composite plate such as the SCFET structure in Figure 5.11. The bending strain of said plate is proportional to the curvature of the neutral plane:

$$\epsilon_{xx}^{bending} \propto -zK_{NP} \propto -z\frac{1}{R} \tag{5.4}$$

where z is the vertical coordinate through the thickness of the plate, K_{NP} corresponds to the curvature of the neutral plane and R is the radius of curvature. In our experiments, the topography of the wrinkled transistors is measured using optical profilometry, hence, only the local out-of-plane deflection of the surface, and therefore, only the local curvature of the surface, is known. K_{NP} in Equation 5.4 can be written to accurately express the bending strain in the conducting channel in terms of the surface curvature as shown in Equation 5.6.

Let $z_0 = z_{FET} - z_{NP}$, $R = r - z_0$ and $z = z_c - z_{NP}$

$$\kappa = \frac{1}{r} = \frac{\partial^2 w(x,y)}{\partial x^2} \tag{5.5}$$

$$K_{NP} = \frac{1}{R} = \frac{1}{r - z_0} = \frac{\kappa}{1 - \kappa z_0} \tag{5.6}$$

Equation 5.6 can be written in terms of the the second derivative of the out-of-plane displacement:

$$K_{NP} = \left[\frac{\partial^2 w(x,y)}{\partial x^2}\right]\left[1 - \frac{\partial^2 w(x,y)}{\partial x^2} z_0\right]^{-1} \tag{5.7}$$

Writing the contribution of bending strain, together with the von Kármán nonlinear elastic plate model gives the full expression for local strain in a wrinkled plate:

$$\epsilon_{xx}^{local}(x,y,z) = \epsilon_0 + \frac{1}{2}\left[\frac{\partial w(x,y)}{\partial x}\right]^2 - z\left[\frac{\partial^2 w(x,y)}{\partial x^2}\right]\left[1 - \frac{\partial^2 w(x,y)}{\partial x^2} z_0\right]^{-1}; \tag{5.8}$$

Equation 5.8 allows us to evaluate the local strain everywhere in a wrinkled conducting channel, provided the local out-of-plane displacement values and the critical strain for buckling, ϵ_0 are known. The raw profilometry data corresponds to the out-of-plane deformation of the top surface and is analyzed as shown in Figure 5.2. ϵ_0 represents the critical strain for buckling, ϵ_c. ϵ_c was calculated from the device wrinkle wavelength at low strain using the classical wrinkling relation $\epsilon_c = {}^1\!/_4 \left({}^3\overline{E_s}/\overline{E_f}\right)^{2/3} = {}^1\!/_4 \left({}^{2\pi t}/_\lambda\right)^2$ [34].

Using Equation 5.8 we are able to visualize the strain everywhere in the conducting channel including the area under the electrodes. Figure 5.12b shows a density map of strain corresponding to the dotted area on the wrinkled transistor on Figure 5.12a. Beyond the ability to calculate and visualize the local strain in the conducting channel of wrinkled SCFET, our aim is to establish a connection between the strain imposed by wrinkling and the observed changes in field-effect mobility. Previous efforts by Sekitani et al. [65,66] studying the effects of global bending strains on OFET mobility and Rang et al. [70] studying the effect of hydrostatic pressure, attribute changes in electrical performance to the change of intermolecular spacing. We infer that different local strains in the wrinkled channel have different effects in the field-effect mobility.

The main difference between previous work and the present study is that distribution of strains in a wrinkled transistor is inhomogeneous; therefore, a way to quantify the collective contribution of all local strains to an effective net strain in a wrinkled channel is required.

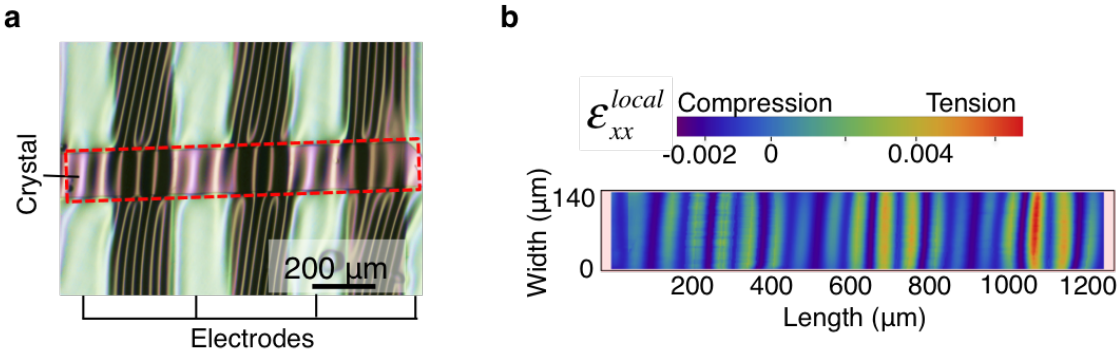

Figure 5.12: Visualization of local strain in a representative wrinkled SCFET.

To obtain a net strain value, ϵ_{xx}^{net} in a wrinkled transistor, we propose superposing each local strain contribution across the conducting channel, including the area under the source and drain electrodes, normalized by the projected area of the wrinkled channel, $WL_{wrinkled}$:

$$\epsilon_{xx}^{net} = \frac{1}{WL_{wrinkled}} \int_0^{L_{wrinkled}} \int_0^{W} \epsilon_{xx}^{local}(x,y)dxdy. \tag{5.9}$$

Figure 5.13 summarizes the mobility change as a function of ϵ_{xx}^{net} for different crystal samples. We discovered that, for negative $\epsilon_{xx_{net}}$ values, mobility increases because the wrinkled channel is in a state of net compression. Positive ϵ_{xx}^{net} values cause the mobility to decrease due to a state of net tension. Our analysis assumes that the effect of strain on mobility follows the same linear trend for both tension and compression. We noticed that ϵ_0 can play a dominating role in the calculation of local strain values

when the strain contribution from wrinkles is small in relation to ϵ_0. The ϵ_{xx}^{net} value can be used to understand the effect of complex mechanical deformations on field-effect mobility. The rubrene molecules are bonded by weak van der Waals forces in the solid state. Therefore, in comparison to its covalently bonded inorganic counterparts, rubrene single crystals can be considered "soft" semiconductors. We speculate that bending strains in wrinkled transistors alter the intermolecular distances in the crystal and consequently the electrical properties of the SCFETs. Mechanical compression reduces the intermolecular distances, increasing the mobility. Tension increases intermolecular distances, decreasing the mobility. It is important to mention that our model does not consider the effects of strain on charge injection. If by straining, we are indeed modifying the d-spacing along the conducting channel, charge injection might be affected. In order for this phenomenon to be integrated into our model, we would need to understand how changing crystal structure affects charge injection and the current density through the thickness of the crystal along the path from the electrode/organic semiconductor interface to the organic semiconductor/insulator interface. We include the area under top contact electrodes in the integration limits of ϵ_{xx}^{net} to account for possible changes in current density that may occur as a result of strain under source and drain areas at the semiconductor/insulator interface.

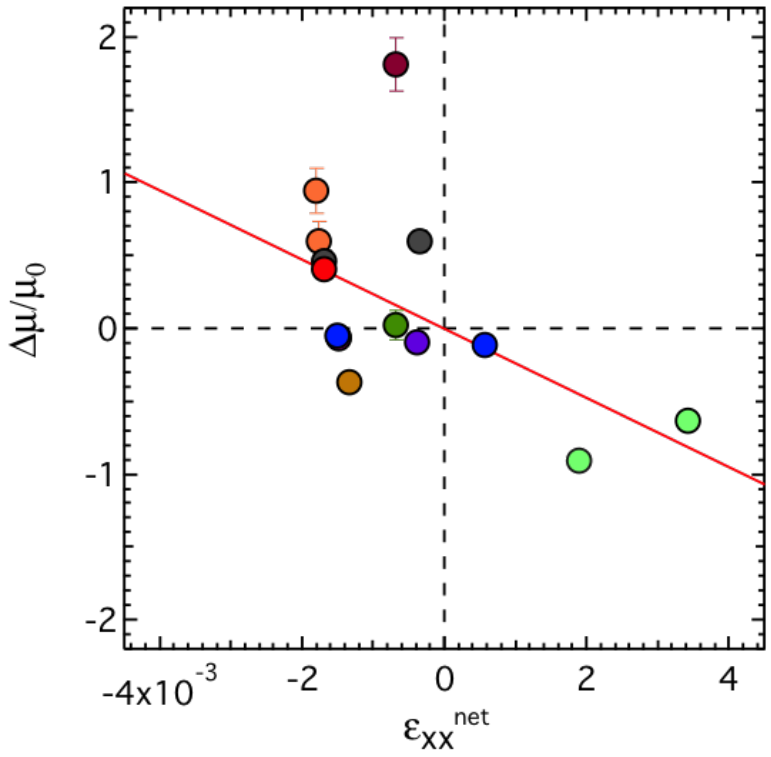

Figure 5.13: Effect of net channel strain in field-effect carrier mobility of rubrene transistors. Net compression (negative values) causes mobility increase and the opposite effect is observed for net channel tension (positive values). Different colors represent different devices. Individual device details are shown in Appendix B.

5.4 Summary

In the field electronics, the wavy surface features produced by wrinkling have been exploited as a suitable way to make flexible devices of both inorganic and organic semiconductors that are able to stretch, in a way analogous to an accordion, without damaging the active layer. We have fabricated wrinkled rubrene single-crystal field-effect transistors; demonstrating the ability of organic single crystals to maintain high-performance while withstanding inhomogeneous strains in the conducting channel. Changes in mobility upon wrinkling reveal that the performance of rubrene is very sensitive to small deformations of the conducting channel. We proposed a model

based on plate bending to quantify the net strain in the dielectric/crystal interface of wrinkled rubrene transistors. An important finding of this work is the ability to relate the increases in mobility to net compressive strains and mobility decreases to tensile net strains in the conducting channel. These results provide a strong foundation for the potential of using the wrinkling instability to modulate, even enhance, the performance of organic semiconductors which benefit from uniquely soft intermolecular bonds. This work will have broad applicability, bringing new understanding of strain induced changes in performance observed when deforming different device structures.

5.5 Open Questions

Wrinkled structures have an immense potential for their use in stretchable and conformable electronics able to withstand large deformations without degradation of performance. The present study focused on deforming SCFETs only within the wrinkling regime of strain. It is therefore of great importance to understand what are the limits of performance of organic semiconductors while undergoing higher inhomogeneous and localized strains, such as folds and creases.

Although a general dependence of mobility change on net strain is obtained with our current model, there is scatter present (Figure 5.13). What is the origin of the scatter? Do shear stresses play a roll? How is charge injection affected by strain at metal-semiconductor interface? If charge injection is affected, how can it be integrated into the net strain model.

From our model it is clear that the number of waves within the channel area is important in the net strain definition. Future efforts focusing on how to control the wavenumber between contacts will provide an extra handle to control the net strain in the conducting channel.

Finally, experiments like the ones presented in this chapter, but inducing wrinkles along directions different from the b [010] axis will expand our interpretation of how

strains affect charge transport properties in an anisotropic material such as rubrene. In addition, to obtain a comprehensive picture of the effects of strain to the crystal structure of rubrene single crystals, microstructure studies aided by diffraction techniques are necessary.

CHAPTER 6

CONCLUSIONS

This dissertation centered in elucidating the mechanical properties of organic semiconductors and understanding how the application of strains can modify their performance in electronic devices. Our motivation was that the solid state packing of different molecular structures gives rise to different mechanical and electrical properties which should be taken into account when designing flexible and conformable electronic technologies.

In Chapters 2 and 3 we studied how molecular structure affects the mechanical response of organic semiconductors. Our general approach was to study the mechanical properties of single crystals of small molecule hydrocarbons and a small set of highly crystalline polythiophene molecules. Our method to map mechanical anisotropy of crystals using wrinkles, proved to be a practical and accurate way to measure small differences in the effective in-plane moduli for any anisotropic thin-film material.

In Chapters 4 and 5 we explored how homogenous and inhomogeneous mechanical deformations affect the electrical properties of organic semiconductors, respectively. We demonstrated that mechanical strains affect crystal structure and therefore, charge transport phenomena, by measuring a piezoresistive coefficient of approximately 11.26 in rubrene single crystals. We also showed that rubrene single crystals can withstand inhomogeneous deformations without fracturing, proving that molecular crystals could be utilized in flexible electronic applications. In the future, the ability to modulate the field-effect mobility, demonstrated in Chapter 5, might have applications similar to strained Si channel transistors, used in modern commercial

electronics to tune the response of transistors in circuits. Our proposed model quantifying the net strain provides a novel way to control of charge transport properties by using inhomogeneous mechanical strains.

In the context of materials for flexible electronics, correlations between mechanical and electrical properties are of great interest. In general, correlations between different classes of physical properties (cross-property correlations) are key in the implementation of materials in engineering design. Establishing correlations between conductivity and elasticity remains a challenging problem given that the properties are represented by tensors of different ranks. Analysis of our results combined with literature values of modulus and field-effect mobilities, allowed us to reach some general conclusions regarding the correlation between mechanical and electrical properties of crystalline organic semiconductors. In Figure 6.1 we show a correlation map between elastic modulus and field-effect mobility for organic electronic materials. It can be seen that thiophene oligomers have a wide span of elastic moduli but their field-effect mobility remains relatively low. Thiophene polymers, on the other hand, show an almost monotonic increase in mobility as their modulus increases, showing the highest mobility and modulus value for the polymer with the highest degree of crystallinity (annealed pBTTT) [32]. The highest modulus and mobilities correspond to rubrene single crystals and polycrystalline pentacene. As expected, the mobility of pentacene is lower than that of rubrene, due to the presence of grain boundaries. Based on Figure 6.1 it is difficult to establish a comprehensive correlation between modulus and field-effect mobility.

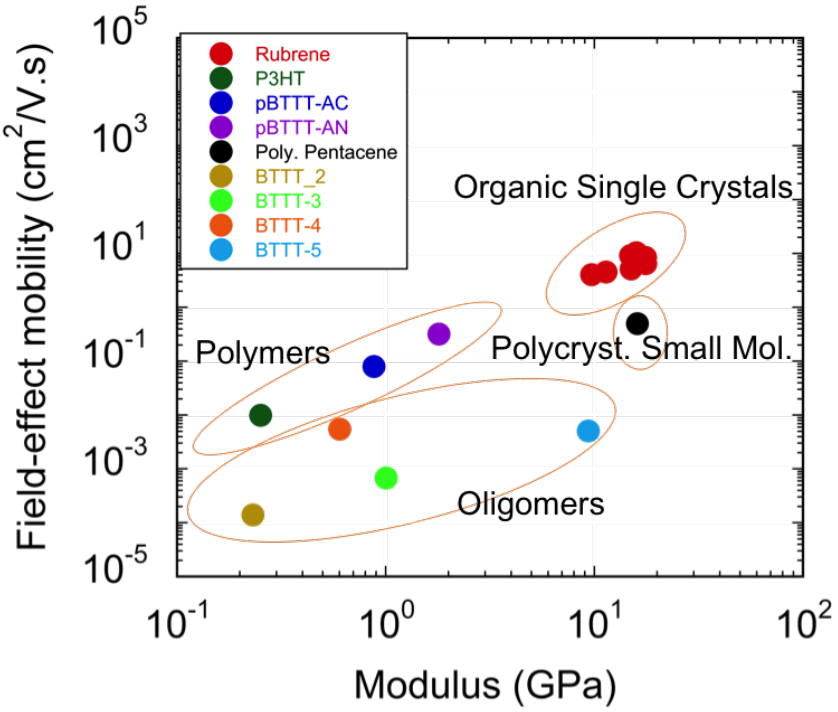

Figure 6.1: Average field effect mobility of organic semiconductor materials as a function of average modulus. Average mobility and modulus values for P3HT, pBTTT as-cast (AC) and annealed (AN) were obtained from O'Connor et al. [32]. Average mobility and modulus values for polycrystalline pentacene were obtained from Tahk et al. [31].

In conclusion, knowledge of mechanical properties of single crystals and polycrystalline films of organic semiconductors, together with an understanding of strain effects on electrical properties, are necessary for the effective development of organic flexible electronics. We are confident that the research presented here will impact electronic device architectures and future molecular design strategies of materials tailored for flexible electronic applications. We anticipate that organic single crystals will continue to play an important role in the development of the next generation of high-performance electronic technologies, including flexible transistors, stretchable solar cells, and pressure sensors.

APPENDIX A

MORPHOLOGICAL DATA FOR BTTT SERIES

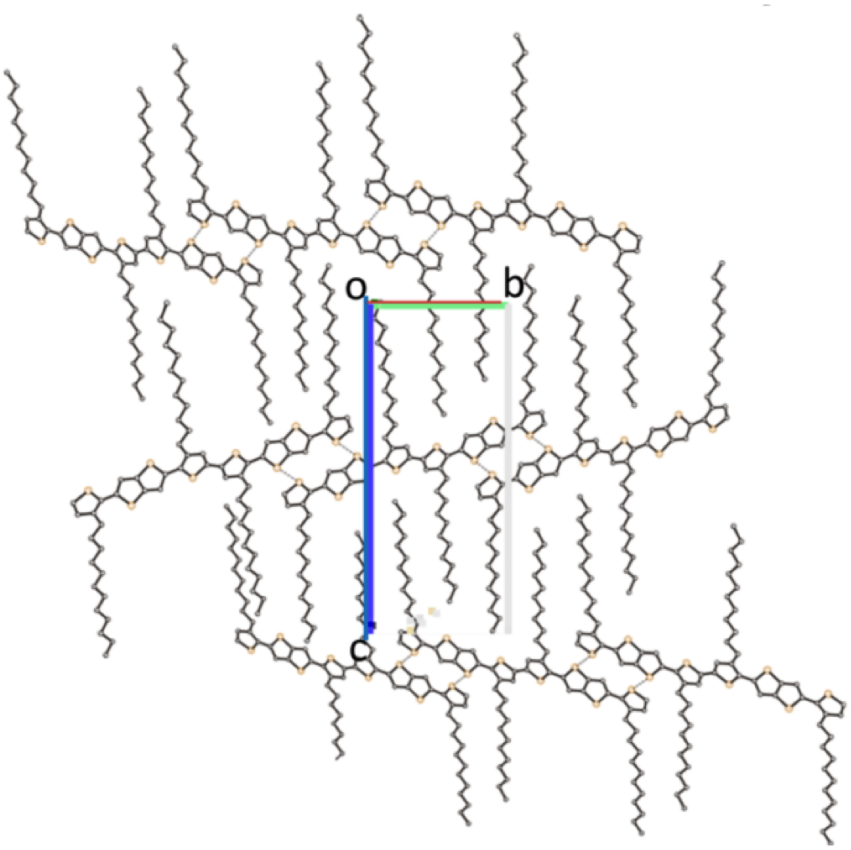

Figure A.1: BTTT-2 crystal packing along the a-axis obtained from single crystal x-ray diffraction. Adapted and reprinted from Ref. [60]. Copyright (2014) American Chemical Society.

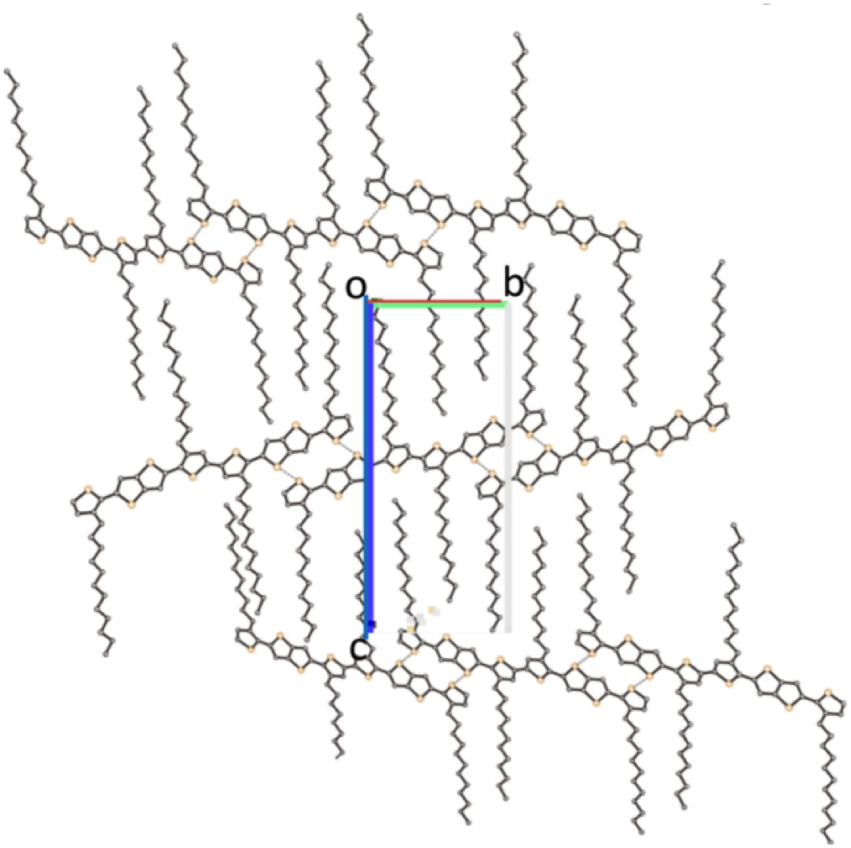

Figure A.2: BTTT-2 crystal structure showing 48° sheet rotation. Adapted and reprinted from Ref. [60]. Copyright (2014) American Chemical Society.

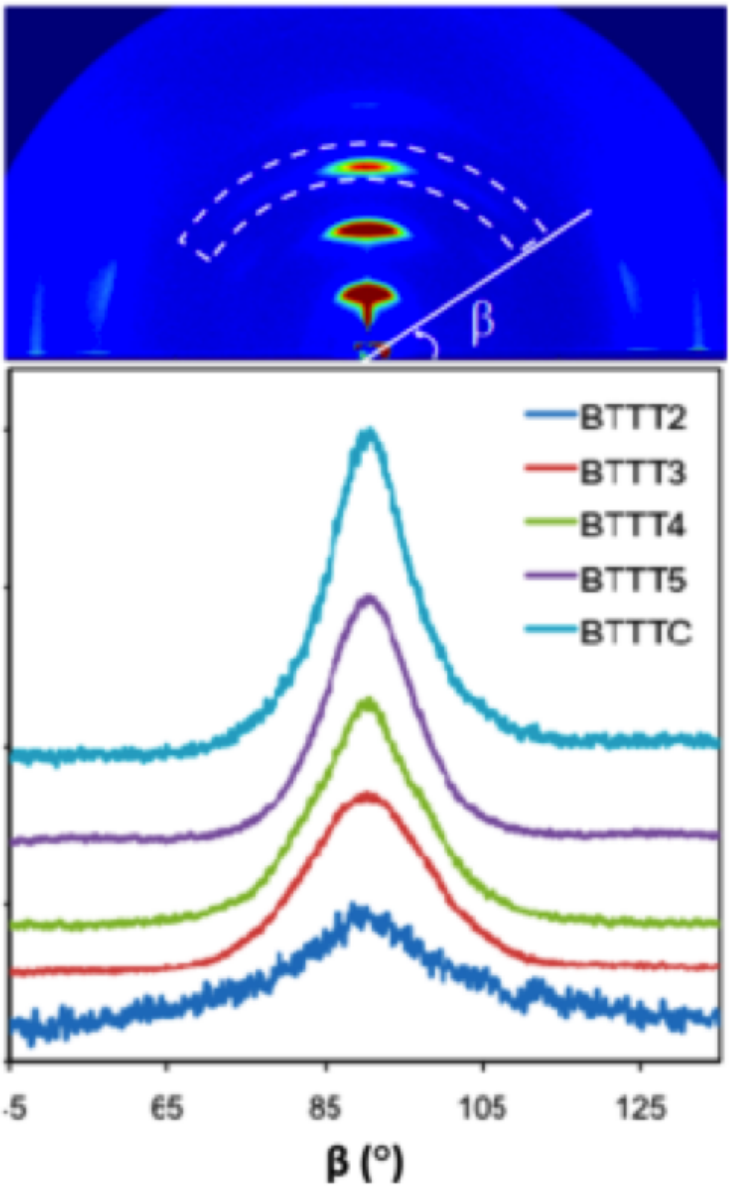

Figure A.3: Pole figures of (300) Bragg reflection show better crystallite-substrate alignment as a function of increasing molecular weight. Adapted and reprinted from Ref. [60]. Copyright (2014) American Chemical Society.

APPENDIX B

EXPERIMENTAL DETAILS FOR RUBRENE CRYSTAL FIELD-EFFECT TRANSISTORS TESTED

$\Delta\mu/\mu_0$	Micrograph	L (μm)	W (μm)	L/W	t_{Au_gate} (nm)	$t_{Parylene}$ (nm)	$t_{Rubrene}$ (nm)	Z_{np}* (nm)
-0.02	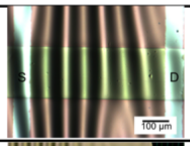	497	190	2.61	40	1074	646	1001
-0.05	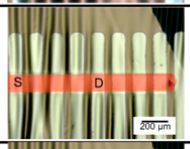	500	135	3.70	40	1125	235	660
-0.05		950	135	7.03	40	1125	235	660
-0.06	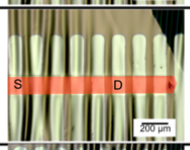	650	135	4.81	40	1125	235	660
-0.09	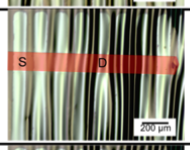	500	135	3.70	40	1125	235	660
-0.11	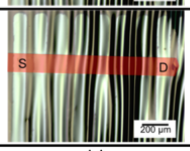	950	135	7.03	40	1125	235	660
-0.37	** 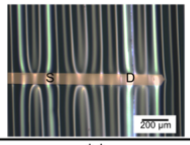	472	69	6.86	40	1055	839	1036
-0.9	** 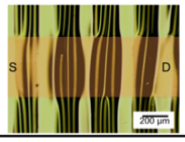	1063	460	2.31	40	520	250	260

$\Delta\mu/\mu_0$	Micrograph	L (µm)	W (µm)	L/W	t_{Au_gate} (nm)	$t_{Parylene}$ (nm)	$t_{Rubrene}$ (nm)	Z_{np}* (nm)
0.025	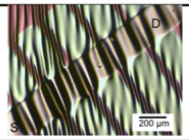	1350	237	5.68	40	703	680	780.8
0.41	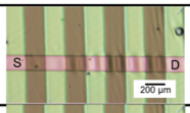	1400	150	9.33	40	685	890	900
0.47	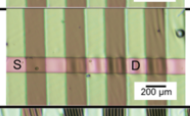	1000	150	6.67	40	685	890	900
0.6	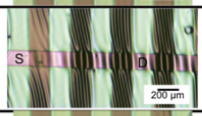	1000	150	6.67	40	685	890	900
0.60	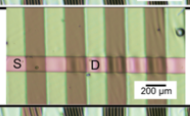	600	150	4	40	685	890	900
0.95	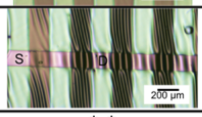	600	150	4	40	685	890	900
1.8	** 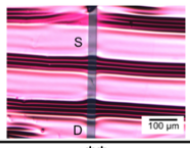	225	38	5.96	35	536.66	173	322
N/A	** 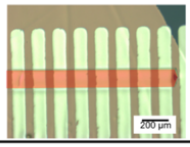	50-950	135	7.03	40	1125	235	660

*Neutral plane position. Vertical distance from elastomer/transistor interface
**Crystal position has been colorized for clarity.

BIBLIOGRAPHY

[1] K. Faber, K. Malloy, *The mechanical properties of semiconductors* (Academic Press, 1992).

[2] H. Klauk, *Organic Electronics* (Wiley-VCH Verlag GmbH & Co., 2006).

[3] C. W. Tang, S. A. Vanslyke, *Applied Physics Letters* **51**, 913 (1987).

[4] B. Geffroy, P. le Roy, C. Prat, Organic light-emitting diode (OLED) technology: Materials, devices and display technologies (2006).

[5] C. J. Brabec, *et al.*, *Advanced materials (Deerfield Beach, Fla.)* **22**, 3839 (2010).

[6] M. Kaltenbrunner, *et al.*, *Nature Communications* **3**, 770 (2012).

[7] G. Horowitz, D. Fichou, X. Peng, Z. Xu, F. Garnier, A field-effect transistor based on conjugated alpha-sexithienyl (1989).

[8] Z. Bao, J. Locklin, *Organic Field-Effect Transistors* (CRC Press, 2007).

[9] F. Garnier, *Chemical physics* **227**, 253 (1998).

[10] M. E. Gershenson, V. Podzorov, *Rev. Mod. Phys.* **78**, 973 (2006).

[11] V. C. Sundar, *et al.*, *Science* **303**, 1644 (2004).

[12] S.-h. Wen, A. Li, J. Song, W. Deng, *The Journal of Physical Chemistry B* **113**, 8813 (2009).

[13] S. F. Nelson, Y.-Y. Lin, D. J. Gundlach, T. N. Jackson, *Applied Physics Letters* **72**, 1854 (1998).

[14] R. De Boer, M. E. Gershenson, A. Morpurgo, V. Podzorov, *physica status solidi* **201**, 1302 (2004).

[15] R. A. Laudise, C. Kloc, P. G. Simpkins, T. Siegrist, *Journal of Crystal Growth* **187**, 449 (1998).

[16] A. L. Briseno, *et al.*, *Advanced Materials* **18**, 2320 (2006).

[17] C. Reese, Z. Bao, *Materials Today* **10**, 20 (2007).

[18] B. Moulton, M. Zaworotko, *Chemical reviews* **101**, 1629 (2001).

[19] T. Matsukawa, *et al.*, *Japanese Journal of Applied Physics* **49**, 085502 (2010).

[20] J. E. Anthony, *Angewandte Chemie (International ed. in English)* **47**, 452 (2008).

[21] A. L. Briseno, *et al.*, *Journal of the American Chemical Society* **128**, 15576 (2006).

[22] A. L. Briseno, *et al.*, *Nano letters* **7**, 668 (2007).

[23] L. F. Drummy, P. K. Miska, D. Alberts, N. Lee, D. C. Martin, *The journal of physical chemistry. B* **110**, 6066 (2006).

[24] S. M. Sze, K. K. Ng, *Physics of Semiconductor Devices, 3rd Edition.; John Wiley & Sons, Inc.; NJ* (John Wiley & Sons, Inc, 2007), pp. 164, 682, second edn.

[25] D. Braga, G. Horowitz, *Advanced Materials* **21**, 1473 (2009).

[26] a. Dodabalapur, L. Torsi, H. E. Katz, *Science (New York, N.Y.)* **268**, 270 (1995).

[27] C. R. Newman, R. J. Chesterfield, J. A. Merlo, C. D. Frisbie, *Applied Physics Letters* **85**, 422 (2004).

[28] a. F. Stassen, R. W. I. De Boer, N. N. Losad, a. F. Morpurgo, *Applied Physics Letters* **85**, 3899 (2004).

[29] J. M. Gere, *Mechanics of Materials* (Brooks/Cole-Thomson Learning, 2004).

[30] J. Groenewold, *Physica A* **298**, 32 (2001).

[31] D. Tahk, H. H. Lee, D.-Y. Khang, *Macromolecules* **42**, 7079 (2009).

[32] B. O'Connor, E. P. Chan, C. Chan, B. Conrad, *ACS nano* **4**, 7538 (2010).

[33] C. M. Stafford, *et al.*, *Nature Materials* **3**, 545 (2004).

[34] J. Chung, A. Nolte, *Advanced Materials* **23**, 349 (2010).

[35] Y. Sun, J. A. Rogers, *Journal of Materials Chemistry* **17**, 832 (2007).

[36] A. J. Baca, J. Ahn, Y. Sun, *Angewandte Chemie ...* pp. 5524 – 5542 (2008).

[37] J. Song, H. Jiang, Y. Huang, J. A. Rogers, *Journal of Vacuum Science & Technology A: Vacuum, Surfaces, and Films* **27**, 1107 (2009).

[38] D. da Silva Filho, E. Kim, J. Brédas, *Advanced Materials* **17**, 1072 (2005).

[39] V. Podzorov, S. E. Sysoev, E. Loginova, V. M. Pudalov, M. E. Gershenson, *Applied Physics Letters* **83**, 3504 (2003).

[40] A. L. Briseno, *et al.*, *Nature* **444**, 913 (2006).

[41] H. Minemawari, *et al.*, *Nature* **475**, 364 (2011).

[42] M. F. Ashby, *Proc. R. Soc. Lond. A* **454**, 1301 (1998).

[43] M. A. Reyes-Martinez, A. Ramasubramaniam, A. L. Briseno, A. J. Crosby, *Advanced Materials* **24**, 5548 (2012).

[44] S. Stuart, A. Tutein, J. Harrison, *Journal of Chemical Physics* **112**, 6472 (2000).

[45] J. Klime, D. R. Bowler, A. Michaelides, *Physical Review B - Condensed Matter and Materials Physics* **83**, 1 (2011).

[46] C. Reese, W.-J. Chung, M.-m. Ling, M. Roberts, Z. Bao, *Applied Physics Letters* **89**, 202108 (2006).

[47] H. Najafov, B. Lee, Q. Zhou, L. C. Feldman, V. Podzorov, *Nature Materials* **9**, 938 (2010).

[48] O. D. Jurchescu, A. Meetsma, T. T. M. Palstra, *Acta crystallographica. Section B, Structural science* **62**, 330 (2006).

[49] E. Cerda, L. Mahadevan, *Physical review letters* **90**, 1 (2003).

[50] S. P. Timoshenko, S. Woinowsky-Krieger, *Theory of plates and shells* (McGraw-Hill, 1959).

[51] S. Im, R. Huang, *Journal of the Mechanics and Physics of Solids* **56**, 3315 (2008).

[52] C. T. Koh, *et al.*, *Applied Physics Letters* **91**, 133113 (2007).

[53] A. Li, S.-H. Wen, J.-L. Song, W.-Q. Deng, *Organic Electronics* **10**, 1054 (2009).

[54] M. Kachanov, *Journal of the Mechanics and Physics of Solids* **49**, 1 (2001).

[55] I. Sevostianov, *Journal of the Mechanics and Physics of Solids* **50**, 253 (2002).

[56] T. C. T. Ting, C. O. Horgan, *Journal of Applied Mechanics* **63**, 1056 (1996).

[57] A. S. Molinari, H. Alves, Z. Chen, A. Facchetti, A. F. Morpurgo, *Journal of the American Chemical Society* **131**, 2462 (2009).

[58] J. W. Lee, *et al.*, *Journal of Applied Physics* **102** (2007).

[59] D. Y. Yoon, P. J. Flory, *Faraday Discussions of the Chemical Society* **68**, 288 (1979).

[60] L. Zhang, *et al.*, *Journal of the American Chemical Society* **136**, 18120 (2014).

[61] J. E. Northrup, *Physical Review B - Condensed Matter and Materials Physics* **76**, 1 (2007).

[62] A. a. Virkar, S. C. B. Mannsfeld, Z. Bao, N. Stingelin, *Advanced Materials* **22**, 3857 (2010).

[63] R. Kline, M. McGehee, E. Kadnikova, J. Liu, J. Fréchet, *Advanced Materials* **15**, 1519 (2003).

[64] R. Noriega, *et al.*, *Nature Materials* **12**, 1038 (2013).

[65] T. Sekitani, *et al.*, *Applied Physics Letters* **86**, 073511 (2005).

[66] T. Sekitani, S. Iba, Y. Kato, T. Someya, *Japanese Journal of Applied Physics* **44**, 2841 (2005).

[67] H. T. Yi, M. M. Payne, J. E. Anthony, V. Podzorov, *Nature communications* **3**, 1259 (2012).

[68] J. E. Northrup, *Applied Physics Letters* **99**, 062111 (2011).

[69] Z. Rang, *et al.*, *Applied Physics Letters* **79**, 2731 (2001).

[70] Z. Rang, *et al.*, *Applied Physics Letters* **86**, 123501 (2005).

[71] Y. Okada, K. Sakai, T. Uemura, Y. Nakazawa, J. Takeya, *Physical Review B* **84**, 245308 (2011).

[72] K. Sakai, *et al.*, *Physical Review Letters* **110**, 096603 (2013).

[73] M. F. Calhoun, J. Sanchez, D. Olaya, M. E. Gershenson, V. Podzorov, *Nature Materials* **7**, 84 (2008).

[74] G. Horowitz, *Advanced Materials* **10**, 365 (1998).

[75] T. Someya, *et al.*, *Proceedings of the National Academy of Sciences of the United States of America* **102**, 12321 (2005).

[76] S. C. B. Mannsfeld, *et al.*, *Nature Materials* **9**, 859 (2010).

[77] I. N. Hulea, *et al.*, *Nature Materials* **5**, 982 (2006).

[78] G. Horowitz, *Organic Electronics* **223**, 113 (2010).

[79] Specialty Coating Systems, Inc. Parylene Properties.

[80] H. Klauk, G. Schmid, W. Radlik, W. Weber, *Solid-State Electronics* **47**, 297 (2003).

[81] P. V. Necliudov, M. S. Shur, D. J. Gundlach, T. N. Jackson, *Solid-State Electronics* **47**, 259 (2003).

[82] N. W. Ashcroft, N. D. Mermin, *Solid State Physics*, vol. 2 (Brooks/Cole-Thomson Learning, 1976).

[83] G. Horowitz, P. Lang, M. Mottaghi, H. Aubin, *Advanced Functional Materials* **14**, 1069 (2004).

[84] J. H. Kang, D. da Silva Filho, J.-L. Brédas, X.-Y. Zhu, *Applied Physics Letters* **86**, 152115 (2005).

[85] P. J. Diemer, *et al.*, *Advanced materials (Deerfield Beach, Fla.)* **25**, 6956 (2013).

[86] A. Rolland, J. Richard, *Journal of the electrochemical society* **140**, 3679 (1993).

[87] S. P. Timoshenko, J. M. Gere, *Theory of Elastic Stability* (Dover Publications, Mineloa, NY, 1961), second edn.

[88] D. Brush, B. O. Almroth, *Buckling of Bars, Plates and Shells* (McGraw-Hill, 1975).

[89] R. M. Jones, *Buckling of Bars, Plates, and Shells* (Bull Ridge, 2006).